Modelling the Evolution of Arctic Melt Ponds

Fern Scott

Centre for Polar Observation and Modelling

Department of Earth Science

University College London

A thesis submitted for the degree of

Doctor of Philosophy

Supervisor

Dr. D.L. Feltham

December 2008

Abstract

During winter the ocean surface at the poles freezes over to form sea ice. Sea ice floats on the ocean surface and has a matrix structure caused by the rejection of salts during freezing. In the summer sea ice melts at its surface creating melt ponds.

An accurate estimate of the fraction of the upper sea ice surface covered in melt ponds during the summer melt season is essential for a realistic estimate of the albedo for global climate models. I will present a melt-pond–sea-ice model that simulates the two-dimensional (areal) evolution of melt ponds on an Arctic sea-ice surface. This advancements of this model compared to previous models are the inclusion of snow topography, a realistic hydraulic balance and calculation of drainage rates and the incorporation of a detailed one-dimensional thermodynamic model. Water transport across and through the sea-ice surface is described by the major hydraulic processes believed to be present. Thermodynamic processes are modelled using the mushy-layer equations in sea ice, heat diffusion equations in snow and using assumptions of turbulent heat flux in melt ponds, along with a three-layer two-stream radiation model.

The model simulates a section of a sea ice floe considered to be in hydrostatic equilibrium, where edge effects such as the presence of leads are neglected and consists of a grid of cells, each of which can be in one of four possible configurations: snow covered ice; bare ice; melt pond covered ice or open water. Eventually, a cluster of adjacent cells each containing melt water may be considered to have formed a melt pond. Lateral and vertical melt water transport is described by Darcy's Law.

The model is initialised with ice topographies that represent either first-year or multi-year sea ice, which are reconstructed from SHEBA ice thickness data using standard statistical methods. The roughness and thickness of the ice and snow surfaces were altered and the sensitivity of the model to the initial data was tested. First-year ice and multi-year ice simulations confirmed observed differences in individual pond size and depth. Sensitivity studies showed that pond fraction is most sensitive to mean initial snow depth in first-year ice simulations and reduction of ice permeability in all cases.

Contents

1 Introduction **1**

1.1 A Brief Introduction to Melt Ponds and Their Importance to Climate and Sea Ice Albedo 2

1.2 Introduction to Sea Ice 6

1.3 The Importance of Sea Ice to Climate 10

1.4 Sea Ice in Climate Models 12

1.5 The Phenomena of Melt Ponds 15

1.5.1 The Lifecycle of a Pond 15

1.5.2 Stage One: Surface Flooding 16

1.5.3 Stage Two: Pond Development 17

1.5.4 Stage Three: Vertical Drainage 17

1.5.5 Stage Four: Freeze Up 18

1.5.6 Comparison of Ponds on First-Year Ice and Multi-Year Ice 18

1.6 Aims and Preview of the Model 19

1.7 Structure of Thesis 20

2 Critical Analysis of Previous Melt Pond Models **21**

2.1 Introduction 21

2.2 The Ebert & Curry (1993) and Ebert *et al.* (1995) Models 22

2.3 The Taylor & Feltham (2004) Model 27
2.4 The Lüthje *et al.* (2006) Model 29
2.5 The Flocco & Feltham (2007) Model 32
2.6 Conclusions 35

3 The Model **38**

3.1 Introduction 38
3.2 Cellular Automaton 40
3.2.1 The Cellular Domain 40
3.2.2 Sea Level and Hydrostatic Equilibrium 42
3.2.3 Hydrology 43
3.2.4 Permeability 45
3.3 Vertical Heat Transport 48
3.3.1 Introduction 48
3.3.2 The Radiation Model 48
3.3.3 Heat Transport Through Sea Ice 52
3.3.4 Heat Transport within Snow 55
3.3.5 Heat Transport in Melt Ponds and Internal Melt Regions 56
3.3.6 Boundary Conditions 57
3.4 Method of Solution for the Thermodynamic Model 62
3.5 Summary 63

4 Stochastic Ice and Snow Thickness Topography Generation and SHEBA Forcing Data **65**

4.1 The Random Field and the Semivariogram 67
4.2 Covariance Model and Semivariogram 67
4.3 The Sill, Range and Nugget Effect 69

4.4 The Theoretical Spherical Covariance Model 70
4.5 Snow and Ice Thickness Data 71
4.6 Forcing Data 76
4.7 Summary 79

5 Simulations of Sea-Ice Melt Ponds on Snow-Covered First-Year Ice 80

5.1 Standard Case 81
5.2 Sensitivity to Snow Topography 87
5.2.1 Rough Snow 87
5.2.2 Smooth Snow 92
5.2.3 Thick Snow 95
5.2.4 Thin Snow 97
5.2.5 Summary 99
5.3 Sensitivity to Ice Topography 100
5.3.1 Rough Ice 100
5.3.2 Smooth Ice 104
5.3.3 Summary 106
5.4 Sensitivity to Vertical Permeability 107
5.4.1 Low Permeability 107
5.4.2 High Permeability 110
5.4.3 Summary 112
5.5 Summary 112

6 Simulations of Sea-Ice Melt Ponds on Snow-Covered Multi-Year Ice 115

6.1 Standard Case 116
6.2 Sensitivity to Snow Topography 123
6.2.1 Rough Snow 125

6.2.2 Smooth Snow . . . 127
6.2.3 Thick Snow . . . 129
6.2.4 Thin Snow . . . 131
6.2.5 Summary . . . 134
6.3 Sensitivity to Ice Topography . . . 134
6.3.1 Rough Ice . . . 135
6.3.2 Smooth Ice . . . 139
6.3.3 Summary . . . 140
6.4 Sensitivity to Vertical Permeability . . . 141
6.4.1 Low Permeability . . . 141
6.4.2 High Permeability . . . 143
6.4.3 Summary . . . 146
6.5 Summary . . . 146

7 Comparison of Simulations with Other Models and Observations 149

7.1 Comparison with Lüthje *et al.* (2006) Model . . . 150
7.1.1 First-Year Ice . . . 152
7.1.2 Multi-Year Ice . . . 156
7.2 Comparison with Flocco & Feltham (2007) Model . . . 160
7.2.1 First-Year Ice . . . 161
7.2.2 Multi-Year Ice . . . 163
7.3 Summary . . . 165
7.4 Comparison of Model Results to Observations . . . 165
7.5 Summary . . . 169

8 Conclusions and Further Work 171

Bibliography **182**

List of Figures

1.1 An aerial photograph of melt ponds that shows their prevalence on the summer sea-ice surface, the darkest regions have the lowest albedo, this is the open ocean, the lighter blue regions are melt ponds. This photograph taken from Perovich *et al.* (1999) was taken on 25th July as pond cover was ubiquitous across the ice surface but before ponds had deepened or melted through to the ocean. The 322 foot long ship in the top centre of the photograph gives an indication of the scale of the ponds. 4

1.2 Arctic sea ice melt pond. Photograph taken on 21st July as part of the albedo study on the SHEBA field trip. Image taken from Perovich *et al.* (1999). 5

1.3 Record minimum sea ice extent in September 2007. The magenta line indicates the median minimum extent between 1979 and 2000. Image from the National Snow and Ice Data Center Sea Ice Index. 7

1.4 Phase diagram for brine, after Curry & Webster (1999). The liquidus curve denotes the temperature at which ice formed from brine of a particular salinity can coexist with melt in thermodynamic equilibrium. The vertical line that begins at A marks brine of salinity 35 psu, brine of this salinity first forms ice at -2 ^{o}C, this is marked by B on the diagram. The ratio CE:ED is the ratio of ice to liquid for brine of salinity 35 psu at a temperature of -10 ^{o}C. 8

1.5 Times series of sea ice extent in the Northern Hemisphere. Curves show interdecadal variation and symbols indicate yearly values. Blue and red curves show Northern Hemisphere sea ice extent for March and September from the Hadley Centre Sea Ice and Sea Surface Temperature data set; the black curve is the April Nordic sea ice extent; and the dotted green is the August ice extent anomaly in Russian Arctic seas. Image taken from Lemke *et al.* (2007). 13

1.6 Arctic September observations of sea ice extent ($\times 10^6$ km^2), the thick red line and 13 climate models used in the Intergovernmental Panel on Climate Change Fourth Assessment Report. The solid black line is the mean of the multi-model ensemble mean and standard deviation from the mean is shown by the dotted black line. Models with more than one ensemble member are indicated with an asterisk. The inset panel shows the nine year running mean. The graph is taken from Stroeve *et al.* (2007). The disparity between model performance and observations may be due to the simplistic modelling of sea ice physics. 14

1.7 Stage One: snow melts and drains laterally across the ice surface, water is lost from the surface through cracks and flaws in the ice. k_j is the vertical ice permeability. Image taken from Eicken *et al.* (2002) 16

1.8 Stage Two: snow cover has been removed, vertical ice permeability has increased which allow ponds to drain through the ice, reducing their hydraulic head. k_j is the vertical ice permeability. Image taken from Eicken *et al.* (2002) 17

1.9 Stage Three: ponds drain to sea level, surface water is lost through thaw holes. k_j is the vertical ice permeability. Image taken from Eicken *et al.* (2002) 18

1.10 Stage Four: pond surfaces freeze over and are covered with fresh snow fall. k_j is the vertical ice permeability. Image taken from Eicken *et al.* (2002) . . 18

3.1 A schematic diagram of the cellular automaton. Each cell has an individual ice thickness, H, and has a horizontal surface area of 25 m^2. Melting decreases the ice thickness in a cell and allows a pond to form on the surface. Water can drain through a cell or can be transported to adjacent cells. . . . 41

3.2 Ice depth below sea level is combined with ice surface height above sea level (which includes negative values), creating a floe with cells which have an initial negative surface height. 43

3.3 An ice core showing the deteriorated, porous layer where most horizontal water transport through ice takes place. In this core the layer is approximately 6 cm thick. Taken from Eicken *et al.* (2002). 47

3.4 Schematic illustrating the layers in the radiation model. The maximum number of layers is three: the frozen surface of a pond, and internal melt region and the sea ice layer, this is shown in the left hand diagram. If the surface of the ice is not frozen over there could be two layers: a pond and the sea ice layer beneath. 50

4.1 The spherical semivariogram. S marks the sill and a is the range. 70

4.2 Probability distribution functions of snow thicknesses on thin ice, first-year ice with melt ponds, hummocky ice and deformed ice. The dashed line shows the mean snow depth. Snow thickness data was collected as part of the SHEBA field study. Image from Sturm *et al.* (2002). 72

4.3 Semivariograms of snow depth on various ice types, from the SHEBA field study. R marks the semivariance range, which is approximately 20 m for snow on all ice types. The ice code on the right hand side indicates the ice type on which the snow was measured, ice code 1 is smooth ice the roughness of the ice surface increases on the scale so that ice code 4 is deformed ice. The key on the left hand side gives the location where the measurements were taken, mean snow depth, standard deviation and the number of data points. Image taken from Sturm *et al.* (2002). 73

4.4 Probability distribution functions for generated first-year ice and snow topographies. 75

4.5 Probability distribution functions for generated multi-year ice and snow topographies. 75

4.6 Observed (thin line) and predicted (thick line) evolution of shortwave radiation with time, using SHEBA Flux Group data. Day 0 is January 1 1997. 78

4.7 Observed (black line) and predicted (white line) evolution of longwave radiation with time, using SHEBA Flux Group data. Day 0 is January 1 1997 78

5.1 Contour plots of the initial mean ice thickness and snow depth in each cell, in the left hand column. The right hand column shows the height of the ice surface above sea level and the height of the snow surface above sea level. Surface heights above sea level can be negative. 83

5.2 Contour plots showing simulated pond depth during the melt season. The top left panel shows pond depth on the day that ponds initially form and the bottom right panel shows pond coverage before freeze up. Dark blue represents bare ice and pond depth scale is illustrated in the colour bar with red for the deepest ponds. White regions are areas where sea ice has melted through entirely. 84

5.3 Top: Variation in the fractional distribution of surface area with time for the standard first-year ice case, where mean ice thickness is 1.7 m, standard deviation in ice thickness of 0.20 m, mean snow thickness is 0.31 m and standard deviation in snow thickness is 0.15 m. Fraction of the surface with a snow cover (light blue), fraction of the surface covered with melt ponds (red), fraction of the ice surface area covered in ponds (dashed red), fraction of the surface with no ice cover (open ocean) is dark blue. Bottom: Change in mean snow depth (light blue), mean pond depth (red) and mean ice thickness (black) with time for the standard first-year ice case. 85

5.4 Top: Variation in the fractional distribution of surface area with time for the alternative standard first-year ice case, where mean ice thickness is 1.7 m, standard deviation in ice thickness of 0.2 m, mean snow thickness is 0.31 m and standard deviation in snow thickness is 0.15 m. Fraction of the surface with a snow cover (light blue), fraction of the surface covered with melt ponds (red), fraction of the surface with no ice cover (open ocean) is dark blue. The dashed lines represent the corresponding values for the standard first-year ice case shown in figure 5.3. Bottom: Change in mean snow depth (light blue), mean pond depth (red) and mean ice thickness (black) with time for the standard first-year ice case. The dashed lines represent the corresponding values for the standard first-year ice case shown in figure 5.3. 88

5.5 Contour plot of the initial mean ice thickness for an alternative first-year ice standard case. Mean ice thickness is 1.7 m and standard deviation is 0.20 m. Despite the spatial differences between this topography and the standard case topography shown in figure 5.1 evolution of pond depth and pond fraction is very similar to the standard case described above. The similarity in evolution in fractional area distribution and change in mean depth of ice, snow and pond is shown in figure 5.4. 89

5.6 Top: Variation in the fractional distribution of surface area with time for the rough case, where mean ice thickness is 1.7 m, standard deviation in ice thickness of 0.2 m, mean snow thickness is 0.31 m and standard deviation in snow thickness is 0.15 m. Fraction of the surface with a snow cover (light blue), fraction of the surface covered with melt ponds (red), fraction of the surface with no ice cover (open ocean) is dark blue. The dashed lines represent the corresponding values for the standard first-year ice case shown in figure 5.3. Bottom: Change in mean snow depth (light blue), mean pond depth (red) and mean ice thickness (black) with time for the rough snow case. The dashed lines represent the corresponding values for the standard first-year ice case shown in figure 5.3. 90

5.7 Mean individual pond area for the standard case (red) and snow sensitivity studies. Scale for the thick snow case (dotted black) in on the right hand side. 91

5.8 Change of aerially averaged surface albedo with time for the standard case and snow sensitivity studies. 92

5.9 Top: Variation in the fractional distribution of surface area with time for the smooth snow case, where mean ice thickness is 1.7 m, standard deviation in ice thickness of 0.2 m, mean snow thickness is 0.31 m and standard deviation in snow thickness is 0.15 m. Fraction of the surface with a snow cover (light blue), fraction of the surface covered with melt ponds (red), fraction of the surface with no ice cover (open ocean) is dark blue. The dashed lines represent the corresponding values for the standard first-year ice case shown in figure 5.3. Bottom: Change in mean snow depth (light blue), mean pond depth (red) and mean ice thickness (black) with time for the smooth snow case. The dashed lines represent the corresponding values for the standard first-year ice case shown in figure 5.3. 93

5.10 Top: Variation in the fractional distribution of surface area with time for the thick snow case, where mean ice thickness is 1.7 m, standard deviation in ice thickness of 0.2 m, mean snow thickness is 0.31 m and standard deviation in snow thickness is 0.15 m. Fraction of the surface with a snow cover (light blue), fraction of the surface covered with melt ponds (red), fraction of the surface with no ice cover (open ocean) is dark blue. The dashed lines represent the corresponding values for the standard first-year ice case shown in figure 5.3. Bottom: Change in mean snow depth (light blue), mean pond depth (red) and mean ice thickness (black) with time for the thick snow case. The dashed lines represent the corresponding values for the standard first-year ice case shown in figure 5.3. 96

5.11 Top: Variation in the fractional distribution of surface area with time for the thin snow case, where mean ice thickness is 1.7 m, standard deviation in ice thickness of 0.2 m, mean snow thickness is 0.20 m and standard deviation in snow thickness is 0.15 m. Fraction of the surface with a snow cover (light blue), fraction of the surface covered with melt ponds (red), fraction of the surface with no ice cover (open ocean) is dark blue. The dashed lines represent the corresponding values for the standard first-year ice case shown in figure 5.3. Bottom: Change in mean snow depth (light blue), mean pond depth (red) and mean ice thickness (black) with time for the thin snow case. The dashed lines represent the corresponding values for the standard first-year ice case shown in figure 5.3. 98

5.12 Top: Variation in the fractional distribution of surface area with time for the rough ice case, where mean ice thickness is 1.7 m, standard deviation in ice thickness of 0.2 m, mean snow thickness is 0.31 m and standard deviation in snow thickness is 0.15 m. Fraction of the surface with a snow cover (light blue), fraction of the surface covered with melt ponds (red), fraction of the surface with no ice cover (open ocean) is dark blue. The dashed lines represent the corresponding values for the standard first-year ice case shown in figure 5.3. Bottom: Change in mean snow depth (light blue), mean pond depth (red) and mean ice thickness (black) with time for the rough ice case. The dashed lines represent the corresponding values for the standard first-year ice case shown in figure 5.3. 101

5.13 Mean individual pond area for the standard case and snow sensitivity studies. 103

5.14 Change of aerially averaged surface albedo with time for the standard case (solid line) and ice sensitivity studies. 104

5.15 Top: Variation in the fractional distribution of surface area with time for the smooth ice case, where mean ice thickness is 1.7 m, standard deviation in ice thickness of 0.2 m, mean snow thickness is 0.31 m and standard deviation in snow thickness is 0.15 m. Fraction of the surface with a snow cover (light blue), fraction of the surface covered with melt ponds (red), fraction of the surface with no ice cover (open ocean) is dark blue. The dashed lines represent the corresponding values for the standard first-year ice case shown in figure 5.3. Bottom: Change in mean snow depth (light blue), mean pond depth (red) and mean ice thickness (black) with time for the smooth ice case. The dashed lines represent the corresponding values for the standard first-year ice case shown in figure 5.3. 105

5.16 Top: Variation in the fractional distribution of surface area with time for the alternative low permeability case, where mean ice thickness is 1.70 m, standard deviation in ice thickness of 0.20 m, mean snow thickness is 0.31 m and standard deviation in snow thickness is 0.15 m. Fraction of the surface with a snow cover (light blue), fraction of the surface covered with melt ponds (red), fraction of the surface with no ice cover (open ocean) is dark blue. The dashed lines represent the corresponding values for the standard first-year ice case shown in figure 5.3. Bottom: Change in mean snow depth (light blue), mean pond depth (red) and mean ice thickness (black) with time for the low permeability case. The dashed lines represent the corresponding values for the standard first-year ice case shown in figure 5.3. 108

5.17 Mean individual pond area for the standard case and snow sensitivity studies. Scale for the low permeability case (dashed line) is on the right-hand side. 109

5.18 Change of aerially averaged surface albedo with time for the standard case and permeability sensitivity studies. 110

5.19 Top: Variation in the fractional distribution of surface area with time for the high permeability case, where mean ice thickness is 1.7 m, standard deviation in ice thickness of 0.2 m, mean snow thickness is 0.31 m and standard deviation in snow thickness is 0.15 m. Fraction of the surface with a snow cover (light blue), fraction of the surface covered with melt ponds (red), fraction of the surface with no ice cover (open ocean) is dark blue. The dashed lines represent the corresponding values for the standard first-year ice case shown in figure 5.3. Bottom: Change in mean snow depth (light blue), mean pond depth (red) and mean ice thickness (black) with time for the high permeability case. The dashed lines represent the corresponding values for the standard first-year ice case shown in figure 5.3. 111

6.1 Top: Variation in the fractional distribution of surface area with time for the standard multi-year ice case, where mean ice thickness is 2.5 m, standard deviation in ice thickness of 1.1 m, mean snow thickness is 0.3 m and standard deviation in snow thickness is 0.25 m. Fraction of the surface with a snow cover (light blue), fraction of the surface covered with melt ponds (red), fraction of the surface with no ice cover (open ocean) is dark blue. Bottom: Change in mean snow depth (light blue), mean pond depth (red) and mean ice thickness (black) with time for the standard multi-year ice case. 117

6.2 Contour plots of the initial mean ice thickness and snow depth in each cell, in the left hand column. The right hand column shows the height of the ice surface above sea level and the height of the snow surface above sea level. Surface heights above sea level can be negative. 118

6.3 Contour plots showing simulated pond depth during the melt season. The top left panel shows pond depth on the day that ponds initially form and the bottom right panel shows pond coverage before freeze up. Dark blue represents bare ice and pond depth scale is illustrated in the colour bar with red for the deepest ponds. White regions are areas where sea ice has melted through entirely. 120

6.4 Mean individual pond area for the standard case and snow sensitivity studies. 121

6.5 Top: Variation in the fractional distribution of surface area with time for the alternative standard multi-year ice case, where mean ice thickness is 2.5 m, standard deviation in ice thickness if 1.1 m, mean snow thickness is 0.3 m and standard deviation in snow thickness is 0.25 m. Fraction of the surface with a snow cover (light blue), fraction of the surface covered with melt ponds (red), fraction of the surface with no ice cover (open ocean) is dark blue. The dashed lines represent the corresponding values for the standard first-year ice case shown in figure 6.1. Bottom: Change in mean snow depth (light blue), mean pond depth (red) and mean ice thickness (black) with time for the standard multi-year ice case. The dashed lines represent the corresponding values for the standard multi-year ice case shown in figure 6.1. 122

6.6 Contour plot of the initial mean ice thickness for an alternative multi-year ice standard case. Mean ice thickness is 2.5 m and standard deviation is 1.1 m. Despite the spatial differences between this topography and the standard case topography shown n figure 6.3 evolution of pond depth and pond fraction is very similar in both this and the standard case described above. The similarity in evolution in fractional area distribution and change in mean depth of ice, snow and pond is shown in figure 6.5. 123

6.7 Top: Variation in the fractional distribution of surface area with time for the rough snow case, where mean ice thickness is 2.5 m, standard deviation in ice thickness of 1.1 m, mean snow thickness is 0.30 m and standard deviation in snow thickness is 0.40 m. Fraction of the surface with a snow cover (light blue), fraction of the surface covered with melt ponds (red), fraction of the surface with no ice cover (open ocean) is dark blue. The dashed lines represent the corresponding values for the standard multi-year ice case shown in figure 6.1. Bottom: Change in mean snow depth (light blue), mean pond depth (red) and mean ice thickness (black) with time for the rough snow case. The dashed lines represent the corresponding values for the standard multi-year ice case shown in figure 6.1. 124

6.8 Change of aerially averaged surface albedo with time for the standard case and snow sensitivity studies. 126

6.9 Top: Variation in the fractional distribution of surface area with time for the smooth snow case, where mean ice thickness is 2.5 m, standard deviation in ice thickness of 1.1 m, mean snow thickness is 0.30 m and standard deviation in snow thickness is 0.10 m. Fraction of the surface with a snow cover (light blue), fraction of the surface covered with melt ponds (red), fraction of the surface with no ice cover (open ocean) is dark blue. The dashed lines represent the corresponding values for the standard multi-year ice case shown in figure 6.1. Bottom: Change in mean snow depth (light blue), mean pond depth (red) and mean ice thickness (black) with time for the smooth snow case. The dashed lines represent the corresponding values for the standard multi-year ice case shown in figure 6.1. 128

6.10 Top: Variation in the fractional distribution of surface area with time for the thick snow case, where mean ice thickness is 2.5 m, standard deviation in ice thickness of 1.1 m, mean snow thickness is 0.6 m and standard deviation in snow thickness is 0.25 m. Fraction of the surface with a snow cover (light blue), fraction of the surface covered with melt ponds (red), fraction of the surface with no ice cover (open ocean) is dark blue. The dashed lines represent the corresponding values for the standard multi-year ice case shown in figure 5.3. Bottom: Change in mean snow depth (light blue), mean pond depth (red) and mean ice thickness (black) with time for the thick snow case. The dashed lines represent the corresponding values for the standard multi-year ice case shown in figure 6.1. 130

6.11 Top: Variation in the fractional distribution of surface area with time for the thin snow case, where mean ice thickness is 1.7 m, standard deviation in ice thickness of 0.2 m, mean snow thickness is 0.20 m and standard deviation in snow thickness is 0.25 m. Fraction of the surface with a snow cover (light blue), fraction of the surface covered with melt ponds (red), fraction of the surface with no ice cover (open ocean) is dark blue. The dashed lines represent the corresponding values for the standard multi-year ice case shown in figure 6.1. Bottom: Change in mean snow depth (light blue), mean pond depth (red) and mean ice thickness (black) with time for the thin snow case. The dashed lines represent the corresponding values for the standard multi-year ice case shown in figure 6.1. 132

6.12 Top: Variation in the fractional distribution of surface area with time for the rough ice case, where mean ice thickness is 2.5 m, standard deviation in ice thickness of 1.50 m, mean snow thickness is 0.31 m and standard deviation in snow thickness is 0.25 m. Fraction of the surface with a snow cover (light blue), fraction of the surface covered with melt ponds (red), fraction of the surface with no ice cover (open ocean) is dark blue. The dashed lines represent the corresponding values for the standard multi-year ice case shown in figure 6.1. Bottom: Change in mean snow depth (light blue), mean pond depth (red) and mean ice thickness (black) with time for the rough ice case. The dashed lines represent the corresponding values for the standard multi-year ice case shown in figure 6.1. 136

6.13 Mean individual pond area for the standard case and ice sensitivity studies. 137

6.14 Top: Variation in the fractional distribution of surface area with time for the smooth ice case, where mean ice thickness is 2.5 m, standard deviation in ice thickness of 0.5 m, mean snow thickness is 0.30 m and standard deviation in snow thickness is 0.25 m. Fraction of the surface with a snow cover (light blue), fraction of the surface covered with melt ponds (red), fraction of the surface with no ice cover (open ocean) is dark blue. The dashed lines represent the corresponding values for the standard multi-year ice case shown in figure 6.1. Bottom: Change in mean snow depth (light blue), mean pond depth (red) and mean ice thickness (black) with time for the smooth ice case. The dashed lines represent the corresponding values for the standard multi-year ice case shown in figure 5.3. 138

6.15 Change of aerially averaged surface albedo with time for the standard case and ice sensitivity studies. 139

6.16 Top: Variation in the fractional distribution of surface area with time for the low permeability case, where mean ice thickness is 2.5 m, standard deviation in ice thickness of 1.1 m, mean snow thickness is 0.3 m and standard deviation in snow thickness is 0.25 m. Fraction of the surface with a snow cover (light blue), fraction of the surface covered with melt ponds (red), fraction of the surface with no ice cover (open ocean) is dark blue. The dashed lines represent the corresponding values for the standard multi-year ice case shown in figure 6.1. Bottom: Change in mean snow depth (light blue), mean pond depth (red) and mean ice thickness (black) with time for the low permeability case. The dashed lines represent the corresponding values for the standard multi-year ice case shown in figure 6.1. 142

6.17 Mean individual pond area for the standard case and vertical permeability sensitivity studies. 143

6.18 Change of aerially averaged surface albedo with time for the standard case and vertical permeability sensitivity studies. 144

6.19 Top: Variation in the fractional distribution of surface area with time for the high permeability case, where mean ice thickness is 2.5 m, standard deviation in ice thickness of 1.1 m, mean snow thickness is 0.31 m and standard deviation in snow thickness is 0.25 m. Fraction of the surface with a snow cover (light blue), fraction of the surface covered with melt ponds (red), fraction of the surface with no ice cover (open ocean) is dark blue. The dashed lines represent the corresponding values for the standard multi-year ice case shown in figure 5.3. Bottom: Change in mean snow depth (light blue), mean pond depth (red) and mean ice thickness (black) with time for the high permeability case. The dashed lines represent the corresponding values for the standard multi-year ice case shown in figure 6.1. 145

7.1 Contour plots of the evolution of pond area and depth on first-year ice after 5 days, 20 days, 35 days and 50 days, taken from Lüthje *et al.* (2006). Axis labels are in metres. The scale on the right represents pond depth, shallow ponds are blue and deep ponds are red. White represents bare ice and dark red represents regions where ice has melted through and bare ice is exposed. 154

7.2 Evolution of mean melt pond area from the Lüthje *et al.* (2006) model for first-year ice, dashed line (scale on the right-hand side) and multi-year ice, solid line (scale on the left-hand side). Taken from Lüthje *et al.* (2006) . . . 155

7.3 Area covered with melt ponds from the the multi-year ice standard case described in this thesis, Lüthje *et al.* (2006) multi-year ice model and field studies. 157

7.4 Contour plots of the evolution of pond area and depth on multi-year ice after 5 days, 20 days, 35 days and 50 days, taken from Lüthje *et al.* (2006). Axis labels are in metres. The scale on the right represents pond depth, shallow ponds are blue and deep ponds are red. White represents bare ice and dark red represents regions where ice has melted through and bare ice is exposed. 159

7.5 Results from the Flocco & Feltham (2007) first-year ice simulation. Area covered in melt ponds (top) and area-averaged albedo (bottom). Taken from Flocco & Feltham (2007). 162

7.6 Results from the Flocco & Feltham (2007) multi-year ice simulation. Area covered in melt ponds (top) and area-averaged albedo (bottom). Taken from Flocco & Feltham (2007). 164

List of Tables

4.1 Table of mean and variance of ice thickness and snow thickness(metres) for first-year and multi-year ice. These are the values used to create initial ice and snow surface topographies for the standard cases. 74

4.2 Table of mid-monthly forcing data used in the melt-pond–sea-ice model. . . 77

5.1 Summary of important results from the standard first-year ice case and sensitivity studies. 114

6.1 Summary of important results from the standard multi-year ice case and sensitivity studies. 148

List of Symbols

$(\rho c)_l$ Volumetric specific heat capacity of interstitial brine, equal to 4.185×10^6 J / (m^3 K)

$(\rho c)_{pond}$ Volumetric specific heat capacity of pond, equal to 4.185×10^6 J / (m^3 K)

$(\rho c)_{seaice}$ Volumetric specific heat capacity of sea ice, J / (m^3 K)

$(\rho c)_s$ Volumetric specific heat capacity of interstitial ice, equal to 1.883×10^6 J / (m^3 K)

α Surface albedo

$\alpha*$ Coefficient of thermal expansion of pond equal to 5×10^{-5} K^{-1}

$\alpha_{bareice}$ Albedo of bare ice

δt Timestep length, s

ϵ Emissivity of pond, equal to 0.97

Γ Gradient of linearised liquidus curve, equal to 0.0514 K / psu

γ Constant of proportionality for turbulent heat flux, 0.1

$\gamma(h)$ Experimental semivariogram

κ_i Extinction coefficient in layer i, m^{-1}

$\mathcal{L}$ Latent heat of vaporisation, equal to 2.501×10^6 J / kg

$\mathcal{L}_{snow}$ Latent heat of snow, equal to 332424 J / kg

μ Dynamic viscosity, equal to 10^{-3} kg m^{-1} s^{-1}

ν Kinematic viscosity of pond, equal to 10^{-6} m^2 s^{-1}

ϕ Solid volume fraction of sea ice

π_h Horizontal ice permeability, m^2

π_v Vertical ice permeability, m^2

$\prod$ Permeability tensor, m^2

ψ Fluid surface height, m

ρ Density, kg / m^3

ρ_m Density of melt water, kg / m^3

$\rho_s\mathcal{L}$ Latent heat of fusion of pure ice, equal to 3.0132×10^8 J / m^3

ρ_{air} Density of dry air, equal to 1.275 kg / m^3

ρ_{snow} Density of snow, kg / m^3

σ Stefan-Boltzmann constant, equal to 5.67×10^{-8} J / (K^4 m^2 s)

σ_{ij} Covariance

$\mathbf{h}$ Lag, m

A Floe area, m^2

a Range, m

A_i Coefficient dependent on optical properties and depth, W / m^2

A_{pond} Fractional area covered in ponds

B_i Coefficient dependent on optical properties and depth, W / m^2

$C(\mathbf{h})$ Covariance function

C_i Coefficient dependent on optical properties and depth, W / m^2

C_T Stability dependent bulk transfer coefficient

c_{air} Specific heat capacity of dry air, equal to 1005 J / (kg K)

c_{snow} Volumetric specific heat capacity of snow, equal to 2092 J / (kg K)

D Mean draft, m

D_i Coefficient dependent on optical properties and depth

E Factor by which melting is enhanced

E_{pond} Net energy flux at upper surface of pond, W / m^2

E_{seaice} Net energy flux at the upper boundary, W / m^2

E_{snow} Net energy flux at the snow upper surface, W / m^2

$F_C(T)$ Heat flux out of liquid layer at upper boundary, W / m^2

$F_C(T_o)$ Heat flux at upper surface of pond, W / m^2

$F_{\downarrow i}$ Downwelling irradiance for layer i, W / m^2

$F_{\uparrow i}$ Upwelling irradiance for layer i, W / m^2

F_{lat} Latent heat flux, W / m^2

F_{LW} Incoming longwave radiation, W /m^2

$F_{net}(h_{lower})$ Net irradiance at lower surface of pond, W / m^2

$F_{net}(h_{upper})$ Net irradiance at upper surface of pond, W / m^2

$F_{net}(z)$ Total radiant heat energy at depth z, W / m^2

F_{ocean} Heat flux from the ocean into sea ice, equal to 2 W / m^2

F_{sens} Sensible heat flux, W / m^2

F_{SW} Incident shortwave radiation, W / m^2

g Gravitational acceleration, equal to 9.8 m / s^2

H Ice thickness, m

$h(t)$ Snow thickness at time t, m

h_i Position within layer, m

h_{max} Depth beyond which melt rate is no longer enhanced, m

h_{pond} Depth of pond, m

i_o Fraction of incident radiation that penetrates the material

J Turbulent heat flux factor, equal to 1.907×10^{-5} m / (s $K^{1/3}$)

j_i Arithmetic mean of variable $z_i(\alpha)$

j_j Arithmetic mean of variable $z_j(\alpha)$

k_i Absorption coefficient in layer i, m^{-1}

k_l Thermal conductivity of brine, 0.5 W / (m K)

k_{seaice} Thermal conductivity of sea ice, W / (m K)

k_{snow} Thermal conductivity of snow, equal to 0.31 W / (m K)

k_s Thermal conductivity of pure ice, 2 W / (m K)

m Melt rate of ice beneath ponds, cm / day

m_i Melt rate of bare ice, cm / day

m_p Constant parameter

m_{+h} Lag mean

m_{-h} Lag mean

n Number of measurements

$N(h)$ Number of pairs of data measured at a lag h and in a given direction

p Pressure, Pa

q Darcy velocity, m / s

q_o Specific humidity at surface

q_{air} Specific humidity at reference level

r_i Scattering coefficient in layer i, m^{-1}

R_o Fresnel reflection coefficient

s_i Optical parameter dependent on absorption and extinction coefficients in layer i

T Temperature, K

t Time, s

$T_L(C_{pond})$ Equilibrium freezing temperature at concentration C_{pond}, K

T_o Surface temperature, K

T_{air} Surface temperature of air, K

T_{ice} Temperature of snow at snow–ice interface, K

T_{lower} Temperature at lower boundary, K

T_{upper} temperature at upper boundary of pond

U Interstitial Darcy velocity, equal to $u/(1-\phi)$, m / s

u Darcy velocity component in the horizontal direction, m / s

v Darcy velocity component in the vertical direction, m / s

v_{wind} Wind speed at reference height, equal to 4.9 m / s

x_i Mass of ice, kg

x_p Mass of water, kg

x_s Mass of snow, kg

z_h Vertical component of hydraulic head, m

z_i Position within layer i, m

Chapter 1

Introduction

The main motivation of this thesis is to improve our understanding of the physics that governs the formation and horizontal and vertical evolution of Arctic melt ponds in order to facilitate improvements in calculating sea ice albedo in the sea ice component of global climate models. This chapter will give a brief introduction to sea ice and melt ponds, summarise the importance of sea ice to climate, and place the research into its wider field to outline the motivations for this work. Global climate models are being used to inform us of the changes in climate we should expect in the future. Sea ice is modelled in a simplistic way and yet sea ice is known to be an important part of the climate system. Its importance is due to the amplification of warming that is expected at the poles, which can be used an indicator of global changes and also because sea ice links the ocean and atmosphere so changes affect and feedback between both systems. The reason for the polar amplification of warming is the ice–albedo feedback. This is the process whereby if there is an increase in temperature sea ice extent will reduce, thus more ocean with a low albedo will be exposed, more radiation will be absorbed and warming will increase thus causing a further reduction in ice extent. Polar amplification is expected to double global mean temperature rise at the poles. Sea ice needs to be modelled in a way that

realistically captures the processes affecting sea ice mass balance so that sea ice can be confidently used as an adequate indicator of changes in climate.

Melt ponds are a persistent feature of the summer sea ice surface and therefore they need to be modelled. The grid size of global climate models is such that melt ponds are sub grid scale and need to be included as a parameterisation of some sort. To ensure that the parameterisation is a realistic description we need to understand the physics that governs melt pond growth so that the parameterisation can be physically based. The model described in this thesis aims to investigate the sensitivity of melt ponds to variations in topography and sea ice permeability so that we can improve our understanding of what governs melt pond formation and growth.

The following sections of this chapter introduce sea ice and melt ponds and their relevance to the climate and to the scientific community. First is a general introduction to melt ponds and their importance to climate. This is followed by a description of the formation and structure of sea ice and a discussion of the reasons why sea ice is important to the climate, climate models and climate observations, and why melt ponds need to be modelled. Next the formation and evolution of melt ponds is described, based on observation. Finally I present an overview of the melt-pond–sea-ice model developed in this thesis and describe the structure of the thesis.

1.1 A Brief Introduction to Melt Ponds and Their Importance to Climate and Sea Ice Albedo

Arctic melt ponds are pools of water that collect in depressions on the surface of sea ice during the melt season; they are formed from melting snow and ice and spread across the sea-ice surface, driven by hydraulic gradients. Melt ponds affect the fraction of solar radiation reflected from the sea-ice surface and for this reason they are an important

feature of sea ice. The ratio of incident radiation to reflected radiation is known as the albedo, a totally absorbing body has an albedo of 0 and a totally reflecting body has an albedo of 1. Winter sea ice, which is highly reflective, has an almost constant albedo which lies between 0.8-0.9, in winter sea ice is often covered with snow which also has an albedo between 0.8-0.9. In the winter months, therefore, the aerially averaged albedo of sea ice is easy to establish. In the summer months the surface of sea ice can be covered with ponds. Pond covered ice has a much lower albedo than bare ice, and so the aerially averaged albedo of the sea-ice surface is more difficult to establish, unless the area covered in ponds is known. The ponded areas themselves may have varying albedo, changing from 0.2 to 0.4, because of the ice beneath them or particulates, such as sediments, biota and other organic matter, in the pond. Due to their low albedo melt ponds absorb more solar radiation than sea ice, the additional absorbed radiation warms the pond and causes further melting at the base and sides of the pond; thus ponded ice melts more quickly than bare ice. The total area covered in ponds therefore can affect the mean thickness of ice. Melt ponds need to be studied in detail because of the impact they have on the albedo. Figure 1.1 is an aerial photograph of melt ponds that shows their prevalence on the summer sea-ice surface, the darkest regions have the lowest albedo, this is the open ocean, the lighter blue regions are melt ponds. This photograph taken from Perovich *et al.* (1999) was taken on 25th July as pond cover was ubiquitous across the ice surface but before ponds had deepened or melted through to the ocean. The 322 foot long ship in the top centre of the photograph gives an indication of the scale of the ponds.

Figure 1.2 illustrates the size of melt ponds from the surface. Melt ponds form from melted snow and typically appear at the end of May and by mid-June cover a significant fraction of the sea-ice surface, Fetterer & Untersteiner (1998), ponds widen and deepen in June and July, sometimes melting through to the ocean, towards the end of August or

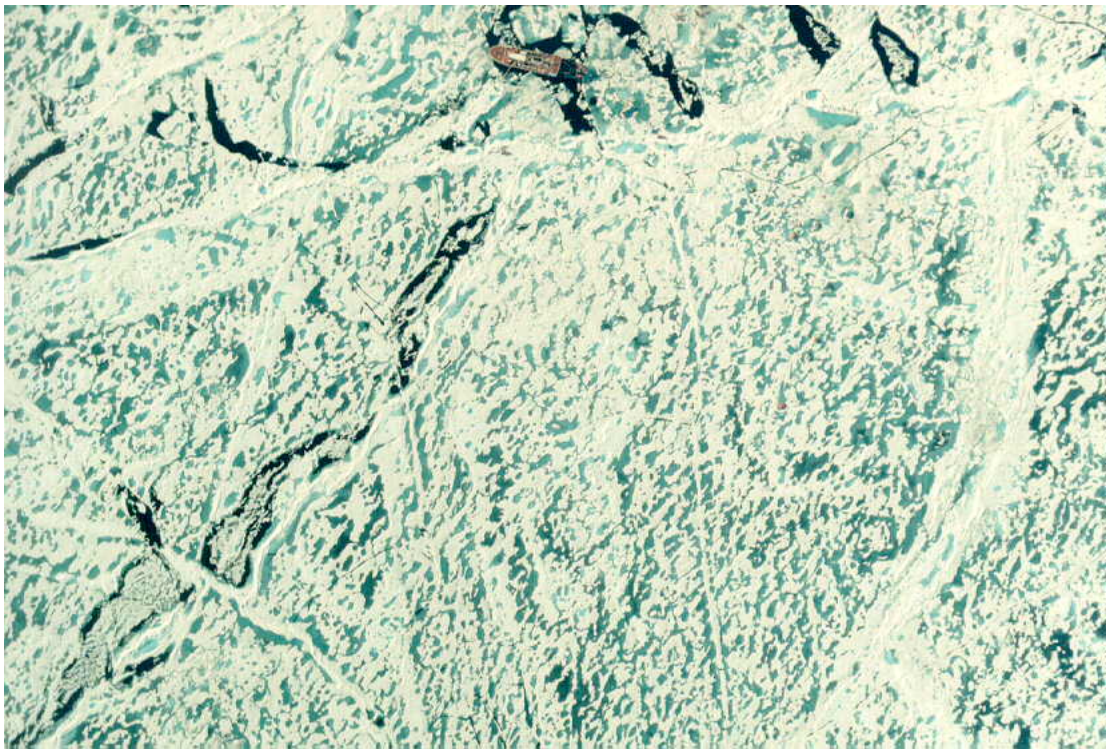

Figure 1.1: An aerial photograph of melt ponds that shows their prevalence on the summer sea-ice surface, the darkest regions have the lowest albedo, this is the open ocean, the lighter blue regions are melt ponds. This photograph taken from Perovich *et al.* (1999) was taken on 25th July as pond cover was ubiquitous across the ice surface but before ponds had deepened or melted through to the ocean. The 322 foot long ship in the top centre of the photograph gives an indication of the scale of the ponds.

Figure 1.2: Arctic sea ice melt pond. Photograph taken on 21st July as part of the albedo study on the SHEBA field trip. Image taken from Perovich *et al.* (1999).

early September ponds begin to freeze over again, Fetterer & Untersteiner (1998) and by the beginning of October frozen over ponds are indistinguishable from the rest of the ice pack, Perovich *et al.* (2002). Fetterer & Untersteiner (1998) observed ponds with a width of up to 400 m. Individual area of melt ponds ranges from 2 m^2 to 8000 m^2 according to Tucker III *et al.* (1999) depending on factors such as the ice topography and permeability of the ice. Tucker III *et al.* (1999) observed a mean pond area of 63 m^2 and a median pond area of 14 m^2, these pond observations were made in July and August, when ponds have developed. Pond area changes as melting increases, for example, Tschudi *et al.* (2001) observed median pond area increase from 15.3 m^2 at the beginning of July to 19.2 m^2 at the end of July.

Pond depth may vary depending on ice topography, melt rates and ice permeability, but a mean depth of 0.35 m was observed by Perovich *et al.* (2002).

While melt ponds have been observed on the sea ice surface in both hemispheres,

Wadhams (2000), Fetterer & Untersteiner (1998), they are far more prevalent in the Arctic. In the Antarctic melt ponds are a less common summer-time feature of sea ice, which is thought to be because the atmosphere is cooler and drier causing the ice surface to be cooler and ice to sublimate rather than melt, Thomas & Dieckmann (2003); also snow is too thick to melt completely in the summer in many areas. In the Arctic melt ponds are a more prominent, consistent feature of the summer-time sea-ice surface so this thesis focusses on a model to simulate the evolution of ponds on Arctic sea ice.

1.2 Introduction to Sea Ice

Sea ice covers approximately 5% to 7% of the Earth's surface. Sea ice is ice that forms from the freezing of the ocean surface, it has a matrix structure combining crystals of pure ice with pockets and channels of brine between the crystals. Sea ice is highly reflective, it is an important part of the climate system because it can alter the radiation budget. Sea ice extent varies: in the winter sea ice covers the entire Arctic ocean, with an area of 1.6×10^7 km^2, Wadhams (2000). In the summer increased solar radiation over the Arctic causes sea ice to melt so that its area is reduced. In 2007, a record minimum extent of 4.3×10^6 km^2 was recorded, Maslanik *et al.* (2007), this is illustrated in figure 1.3. The thickness and properties of the sea ice vary as it melts from the surface. Surface melt ponds are one of the surface properties that affect the absorption and reflection of radiation.

Sea ice forms at lower temperatures than freshwater ice as the salt lowers the freezing temperature of sea water. As the surface of the ocean cools the density of the surface water increases so that it has a greater density than the warmer water below and convection cools the upper layer, 10-100 m, of the ocean.

Sea ice is an alloy of water and salts; the freezing temperature of the alloy depends on

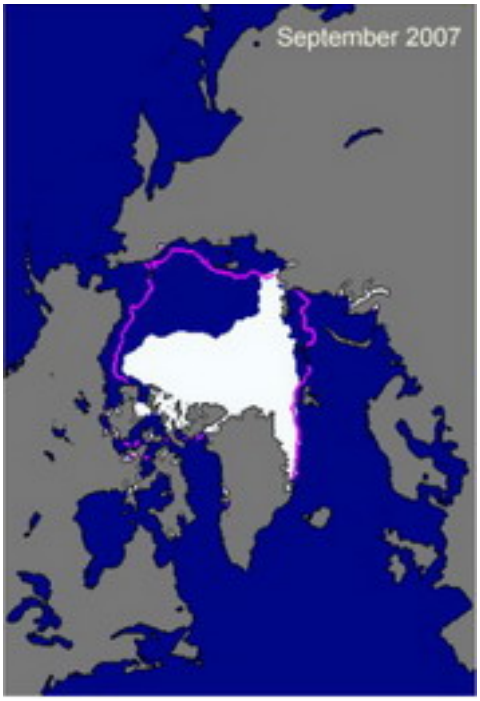

Figure 1.3: Record minimum sea ice extent in September 2007. The magenta line indicates the median minimum extent between 1979 and 2000. Image from the National Snow and Ice Data Center Sea Ice Index.

its composition (how saline it is), for the ocean the freezing temperature is approximately -2 ^{o}C. The components of the alloy do not freeze together, so pure ice forms first rejecting the solute back into the liquid phase, sea ice forms in such a way that sea ice is a matrix of solid pure ice surrounded by saline pockets. The salinity of the liquid phase of the alloy is determined by the liquidus curve. The liquidus curve shows the temperature at which solid crystals (in this case ice) can coexist with melt of a given salinity in thermodynamic equilibrium. This is shown on the phase diagram, figure 1.4.

As sea water is cooled below its freezing point ice begins to form and the ratio of pure ice to brine increases, which causes the salinity of the brine to increase. For example, sea water with an initial salinity of 35 psu (where psu is practical salinity units, defined as the ratio of electrical conductivity of a sample to that of a standard solution of potassium chloride) will start to form ice when it is cooled to -2 ^{o}C, and once the temperature has decreased to -10 ^{o}C the salinity of the brine will have increased to 140 psu. The ratio of

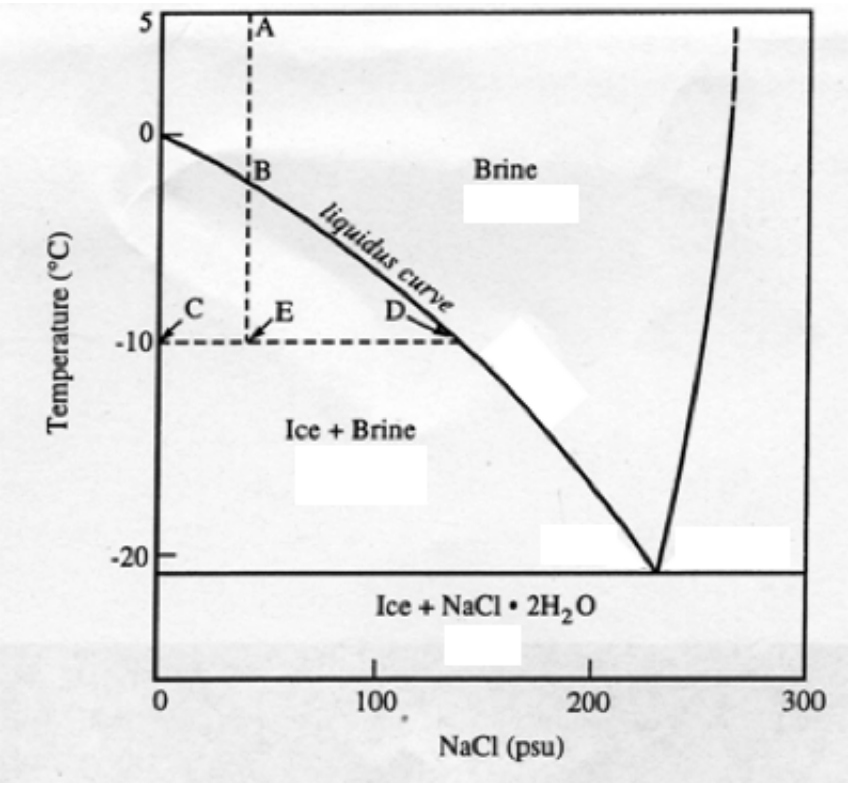

Figure 1.4: Phase diagram for brine, after Curry & Webster (1999). The liquidus curve denotes the temperature at which ice formed from brine of a particular salinity can coexist with melt in thermodynamic equilibrium. The vertical line that begins at A marks brine of salinity 35 psu, brine of this salinity first forms ice at -2 ^{o}C, this is marked by B on the diagram. The ratio CE:ED is the ratio of ice to liquid for brine of salinity 35 psu at a temperature of -10 ^{o}C.

ice to liquid is the ratio CE:ED in figure 1.4 for sea water with an initial salinity of 35 psu at -10 ^{o}C.

The molecular crystal structure of ice is described as open, with oxygen atoms sitting along planes. This structure causes solid ice to have a lower density than liquid water, Weeks & Ackley (1986). When ice forms it is energetically "easier" for further crystals to grow in the same plane as the oxygen atoms as there a fewer bonds to be made between ions in this direction; the preferred direction of growth is called the basal plane.

When the ocean reaches its freezing temperature and begins to freeze at its surface, it freezes into circular horizontally aligned discs that are a maximum of 2-3 mm in diameter. The basal plane is usually in the horizontal direction so the discs expand horizontally outwards until growth becomes unstable and a series of horizontal arms are formed, these break off and combine with other discs and needles of ice suspended in the ocean, this is called frazil ice. These crystals are broken up by the motion of the ocean until they freeze together to form areas of ice called grease ice. Grease ice areas join together to form a thin transparent ice sheet called a nila. As water molecules freeze to the base of the ice, the ice becomes white in colour, this process is called congelation growth, Wadhams (2000). At this stage the ice begins a columnar growth process that distinguishes it from all other ice types. It is easier for freezing molecules to be attached along the basal plane, therefore ice growth will be most rapid in the places where an exposed crystal has a vertical basal plane, this causes columns to develop. The crystal structure is not open enough to allow salt ions into the solid, therefore the columns form from pure water, with brine trapped between the columns. Air bubbles can also be trapped during this process.

Sea ice cools from the surface and there is a temperature gradient within in the sea ice which induces a salinity gradient in the brine pockets in order to maintain thermodynamic equilibrium. The most dense brine is closest to the surface, Cox & Weeks (1974). These

conditions are unstable so convective overturning of the brine may take place. This process, called gravity drainage, allows channels to be set up between the brine pockets and brine to gradually drain out of the sea ice. In addition, the upward motion of the sea ice enhances gravity drainage, Notz (2005). During the summer brine is flushed out of the sea ice by melt water with a positive hydraulic head draining through the ice, which is the major mechanism of desalination of sea ice, Untersteiner (1968).

First-year ice is the term used to describe ice in the melt season that has grown over the previous winter; it is usually relatively smooth with a thickness of 1-2 m, Perovich *et al.* (2003). Multi-year ice is ice that has survived at least one winter, it is generally thicker than first-year ice and its surface is deformed by mechanical processes and by melting during previous melt seasons. Sea ice is constantly in motion, driven largely by the wind. Wind stress can cause the sea-ice pack to diverge creating areas of open ocean between ice floes; the areas of open ocean are known as leads. Wind stress can also cause the sea-ice pack to converge which causes sea ice to be crushed into piles of ice blocks on the above and below sea level, this process is known as ridging.

1.3 The Importance of Sea Ice to Climate

Sea ice influences the climate through the ice–albedo feedback, and by moderating the flux of moisture, heat and momentum between the atmosphere and the ocean. It affects the thermohaline circulation and it may affect atmospheric circulation and precipitation, Rodo & Comin (2003).

The albedo of sea ice is significantly greater than the albedo of the ocean and the area of the ocean covered in sea ice is highly variable, this is a property of sea ice that makes it important to the climate system. If there is a perturbation that causes the atmospheric surface temperature to decrease, then additional ice and snow, both of which have high

albedos, will form increasing the area of the Earth's surface covered in ice and snow. The total surface albedo of the Earth will increase. This will cause a larger amount of solar radiation to be reflected away from the Earth's surface which will cause the global surface temperature to decrease further. This is a positive feedback mechanism called the ice-albedo feedback mechanism, McGuffie & Henderson-Seller (2005). At the poles a decrease in temperature could therefore cause a large increase in the surface area covered in ice, but an increase in temperature could cause large reductions in the surface area of ice.

Sea ice acts as a barrier between the atmosphere and ocean; sea ice both controls and is controlled by the flux of moisture, momentum and heat from the ocean and the atmosphere. For example, since sea ice insulates the ocean from the atmosphere, it reduces the rate of cooling of the ocean. At the same time sea ice reduces the rate at which the surface air temperature increases, Thomas & Dieckmann (2003). This will cause changes in regional atmospheric circulation. Precipitation is governed by the flux of moisture into the atmosphere which is affected by temperature, as the temperature of the ocean and atmosphere are affected by the presence of sea ice so is the amount of precipitation regionally.

Thermohaline circulation is the three-dimensional overturning of water forced by salinity and temperature differences. This is a deep water circulation cycle that is driven by heating at low latitudes and cooling at high latitudes as well as influx of fresh water at high latitudes, Slaymaker & Kelly (2007). The influx of fresh water is in part due to sea ice; as sea ice drains and melts in the summer there is an influx of low-salinity water into the ocean.

The extent and thickness of sea ice has been found to be linked to the duration of the melt season, Perovich *et al.* (2003), Laxon *et al.* (2003); if the melt season is long the thickness of ice and area covered in ice may be lower at the end of the subsequent

winter; irrespective of the winter conditions. At this point it is unclear what the impact of a reduction in the thickness or extent of sea ice could cause. It is probable that due to feedbacks, such as the ice–albedo feedback, an increase in temperature will result in a reduction of sea ice extent, but this may not necessarily be a linear process and the whole system is still not fully understood. Due to the feedback mechanisms it has been postulated that an increase in air temperature will induce a reduction in the mean extent of sea ice. Whelan *et al.* (2007) predict that as soon as 2013 the Arctic will be ice free in the summer months, however Bamber & Payne (2004) more conservatively suggest that if present trends gathered from satellite data are correct then it is possible that if the mean sea-ice thickness continues to decrease at the current rate, which is 4 cm a year then in 50 years there could be no sea ice remaining at all in the summer months, Bamber & Payne (2004). However even if the entire summer sea-ice cover is removed the effects of this are unclear. Some possibilities are that the newly exposed Arctic ocean could act as a sink for carbon dioxide, thus reducing the amount of carbon dioxide in the air, Bamber & Payne (2004), which may cause a reduction in atmospheric temperature that may cause sea ice to form. An alternative situation put forward by Wadhams (2000) is that for landfast sea ice an increase in temperature could cause an increase in precipitation which could add to a total amount of fresh water coming into the ocean. This will cause a low-salinity layer at the surface of the ocean which will encourage the formation of more sea ice. The influx of more low-salinity water into the ocean could reduce the basal heat flux into the sea ice and therefore the net effect would be to increase ice thickness.

1.4 Sea Ice in Climate Models

Sea ice is a good indicator of changes in climate because it is very thin, compared to the other types of ice in the cryosphere. This means that sea ice responds to changes

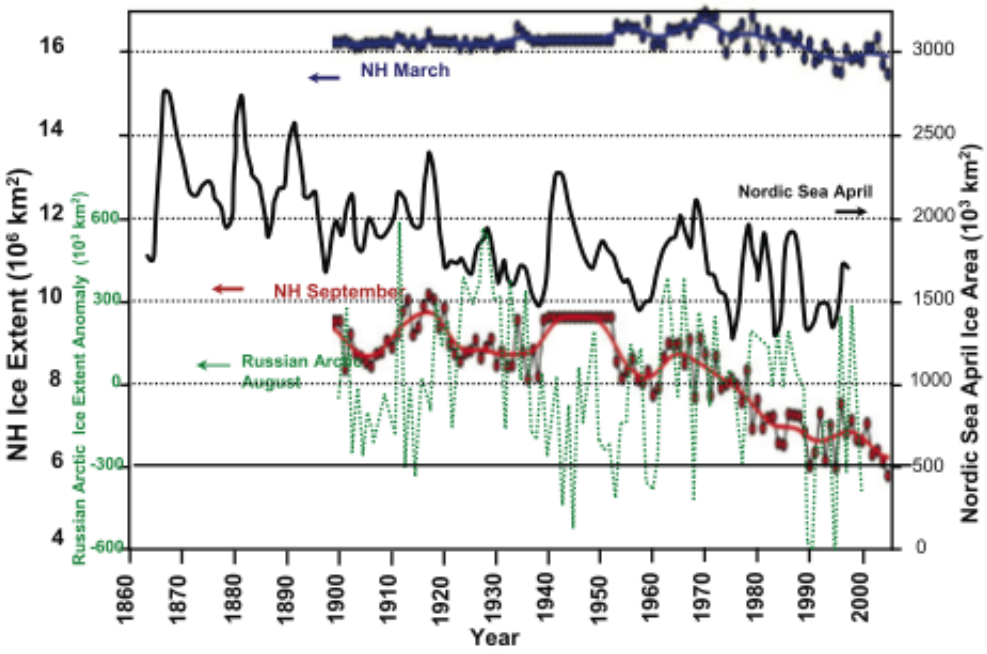

Figure 1.5: Times series of sea ice extent in the Northern Hemisphere. Curves show interdecadal variation and symbols indicate yearly values. Blue and red curves show Northern Hemisphere sea ice extent for March and September from the Hadley Centre Sea Ice and Sea Surface Temperature data set; the black curve is the April Nordic sea ice extent; and the dotted green is the August ice extent anomaly in Russian Arctic seas. Image taken from Lemke *et al.* (2007).

in the atmosphere and ocean more rapidly that other ice types in the cryosphere, such as ice sheets and glaciers. As well as this, due to the ice–albedo feedback, the impact of any changes in climate are amplified at the poles. Sea ice is used as an indicator for climate change in both observations and in modelling, Houghton *et al.* (2001). However because sea ice responds to changes in the ocean and changes in the atmosphere and the timescales for changes in these systems are different and because of feedbacks due to the coupled interactions, sea ice exhibits much variability over interdecadal timescales, this can be seen in figure 1.5 which is a combination of data on sea ice extent in the Northern Hemisphere from satellite, ship reports and coastal observations, Lemke *et al.* (2007). Therefore care is needed to establish whether changes in sea ice are due to natural variability or longer term climate change.

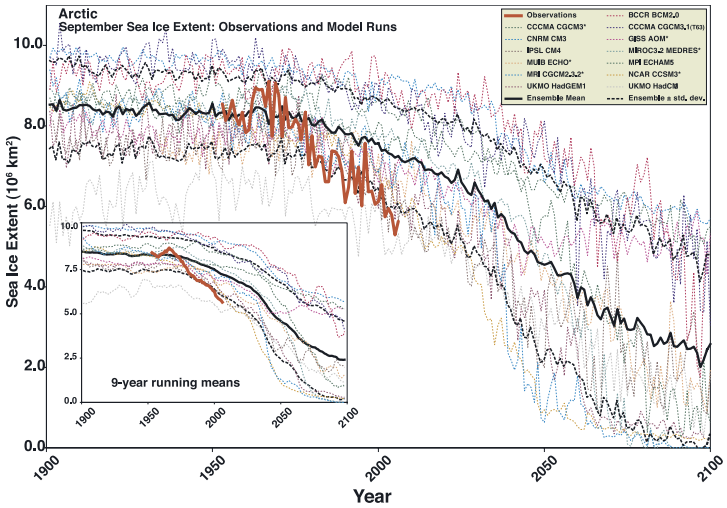

Figure 1.6: Arctic September observations of sea ice extent ($\times 10^6$ km^2), the thick red line and 13 climate models used in the Intergovernmental Panel on Climate Change Fourth Assessment Report. The solid black line is the mean of the multi-model ensemble mean and standard deviation from the mean is shown by the dotted black line. Models with more than one ensemble member are indicated with an asterisk. The inset panel shows the nine year running mean. The graph is taken from Stroeve *et al.* (2007). The disparity between model performance and observations may be due to the simplistic modelling of sea ice physics.

Currently global climate models are being used to predict the possible impact of increased levels of carbon dioxide on the climate. In these models sea ice is used to establish whether any change in climate has taken place. However due to the coupled nature of sea ice, it responds to both the atmosphere and the ocean, sea ice needs to be modelled in great detail in order for accurate predictions to be made. If sea ice is modelled too simplistically the errors will feed back into both atmosphere and ocean components. Figure 1.6 shows the disparity between observations of Arctic sea ice September extent and the mean September sea ice extent of the climate models used in the Intergovernmental Panel on Climate Change Fourth Assesment Report. The poor performance of the models could be due to the simplicity of sea ice physics in the climate models.

The latest generation of global climate models are three-dimensional models that model fluxes between the systems that make up the climate, they have components that model

atmosphere, ocean, land and so on. The ocean component now usually contains a sea-ice component. The sea-ice component estimates the thermodynamic growth of sea ice and the movement of sea ice across the ocean, ridging and divergence of ice are also modelled. In each model component fluxes are evaluated at a number of grid points. In the sea-ice model component a grid cell could represent a surface area of approximately 10 000 km^2. Any process that takes place on a scale smaller than this must be parameterised.

Currently there is no parameterisation to evaluate the area of the surface covered in melt ponds, even though melt ponds can have a significant impact on the surface albedo of sea ice. There is much variability in global climate models and often models are initialised by modelling the current climate as closely as possible and then running into the future to allow future climate conditions to be predicted, one of the methods of checking that the simulation begins with current climate is to compare modelled sea ice extent with observed sea ice extent. However if the sea ice component has parameterisations that do not reflect reality then there can be limited confidence in the outcome.

The area of the sea-ice surface covered in melt ponds affects the surface albedo of sea ice, therefore in order to provide an accurate albedo of sea ice it is necessary to provide an accurate area of surface covered in ponds. In order to do this we need to understand why melt ponds form and how they evolve. The model presented in this thesis examines the formation and evolution of Arctic melt ponds.

1.5 The Phenomena of Melt Ponds

1.5.1 The Lifecycle of a Pond

Melt pond observations described were gathered as part of the Surface Heat Budget of the Arctic, year long field trip, Perovich *et al.* (1999)(hereafter referred to as SHEBA). The field trip provided an extensive set of melt pond observations along with measurements of

sea-ice thickness, snow depth, sea-ice ablation and sea-ice albedo which will be referred to throughout this thesis. The trends that define the four stages of melt are broadly observed across all ice types, Perovich *et al.* (2003), Tucker III *et al.* (1999), Fetterer & Untersteiner (1998), Yackel *et al.* (2000). The four stages of pond evolution are: surface flooding; pond development; vertical drainage; freeze up. The SHEBA melt pond observations described here were made on sections of multi-year ice. The melt season during this observation period lasted 80 days rather than the average of 55 days observed by Russian drifting stations, Lindsay (1998). However the length of the Arctic melt season in all regions has increased by more than one week per decade since 1979, so that in 2005 the longest ever recorded melt season of 121 days in the central Arctic was recorded, Stroeve *et al.* (2006). Thus the SHEBA melt season length is representative of current conditions in the Arctic.

1.5.2 Stage One: Surface Flooding

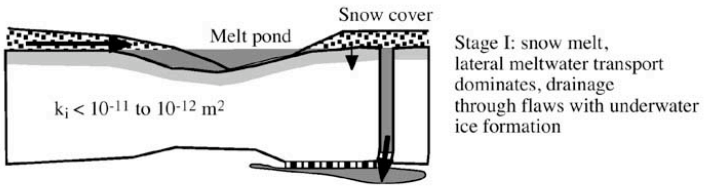

Figure 1.7: Stage One: snow melts and drains laterally across the ice surface, water is lost from the surface through cracks and flaws in the ice. k_j is the vertical ice permeability. Image taken from Eicken *et al.* (2002)

Stage one, illustrated in figure 1.7 begins around Julian Day 149 and ends around Julian Day 175. During this period snow melts and becomes saturated and exposed ice begins to melt at the surface. Vertical ice permeability is low, 10^{-12} - 10^{-11} m^2. As snow and ice melts meltwater percolates into the upper surface of the sea ice. The temperature here is below the melting temperature of sea ice and melt water freezes on contact with the sea ice. In this way the drainage channels of the sea ice are sealed off from the surface melt, Holt & Digby (1985), Eicken *et al.* (2002). Melt water floods the surface and can travel 10

m-100 m laterally across the sea-ice surface driven by differences in hydraulic gradient due to surface topography and differing melt rates Eicken *et al.* (2004). Melt water collects in depressions in the ice, Fetterer & Untersteiner (1998), and channels connecting ponded areas are established. The main source of pond drainage is through cracks, leads and flaws in the ice.

1.5.3 Stage Two: Pond Development

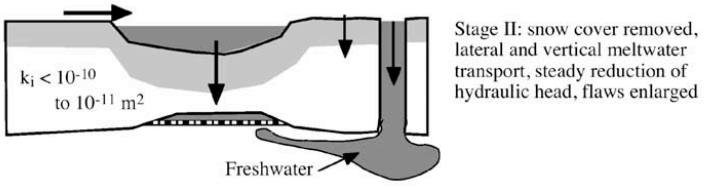

Figure 1.8: Stage Two: snow cover has been removed, vertical ice permeability has increased which allow ponds to drain through the ice, reducing their hydraulic head. k_j is the vertical ice permeability. Image taken from Eicken *et al.* (2002)

Stage two, shown in figure 1.8, continues until about Julian Day 190. Most of the snow has now melted, pond coverage peaks and then ponds shrink back and the edges of ponds are recognisable, this is due to an increase in permeability in the ice allowing both lateral and vertical drainage through the ice. At the same time melt-water production increases and the ice surface is warmed due to enhanced melting beneath ponds. Ice beneath ponds can melt 2-3 times faster than bare ice, Fetterer & Untersteiner (1998).

1.5.4 Stage Three: Vertical Drainage

Stage three, shown in figure 1.9, continues until about Julian Day 207. Vertical permeability is now two orders of magnitude larger than at the beginning of the melt season. Vertical drainage is now much faster than lateral drainage, lateral drainage takes place mainly at the edges of ponds and off floe edges. Ponds have drained to sea level, although melt water production increases due to lateral heat flux through leads and cracks. Ponds

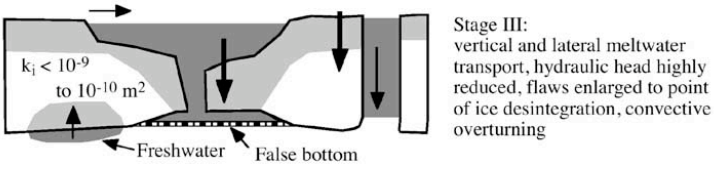

Figure 1.9: Stage Three: ponds drain to sea level, surface water is lost through thaw holes. k_j is the vertical ice permeability. Image taken from Eicken *et al.* (2002)

remain at the locations where they first formed but become deeper and wider, Perovich *et al.* (2002).

1.5.5 Stage Four: Freeze Up

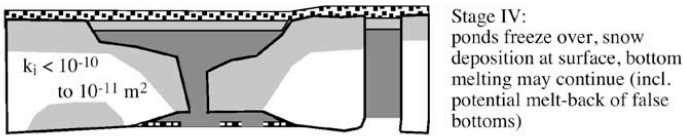

Figure 1.10: Stage Four: pond surfaces freeze over and are covered with fresh snow fall. k_j is the vertical ice permeability. Image taken from Eicken *et al.* (2002)

Stage four, shown in figure 1.10, is freeze up. Ponds that have not drained completely freeze over again at the surface and eventually become covered in snow.

1.5.6 Comparison of Ponds on First-Year Ice and Multi-Year Ice

The four stages of pond evolution described above relate specifically to observations on a particular area of multi-year ice, however with a few differences the four stages are commonly observed across all ice types. First-year ice shows a greater variability in pond fraction than multi-year ice, El Naggar *et al.* (1998). When ponds are present on first-year ice the pond fraction is generally larger than the pond fraction on multi-year ice. Fetterer & Untersteiner (1998) observed first-year sea-ice pond fractions between 0.3 and 0.5, but in some areas pond fraction has been as large as 0.75, Hanesiak *et al.* (2001). Some first-year

ice has been observed to have no melt ponds present at all, Eicken *et al.* (2002), Perovich *et al.* (2002). Initial pond formation on first-year ice appears to be in areas of wind blown snow, with melting snow providing initial melt water, Fetterer & Untersteiner (1998), this assertion was inferred from the majority of ponds being orthogonal to the prevailing wind, Yackel *et al.* (2000). On first-year ice individual ponds cover approximately twice the surface area of ponds on multi-year ice and often channels connect the ponds, Yackel *et al.* (2000), Fetterer & Untersteiner (1998). Perovich *et al.* (2002).

Multi-year ice generally has a lower fraction of the sea-ice surface covered in ponds but has a greater number of ponds than first-year ice. Ponds form in the lowest regions of the sea ice surface, these are often the depressions created by ponds in previous years.

Although some observations, Tucker III *et al.* (1999), have found that pond depth is not related to pond area, ponds on first-year ice, which usually have larger areas than ponds on multi-year ice, are generally less deep than ponds on multi-year ice.

1.6 Aims and Preview of the Model

The aim of this thesis is to improve our understanding of the physics that governs the formation and evolution of sea-ice melt ponds, particularly the horizontal evolution as this has an impact on the albedo of the sea-ice surface in the summer. The sensitivity of pond coverage, pond depth, pond size and ice ablation to changes in ice topography, snow topography and vertical permeability is examined using a new melt-pond model developed in this thesis.

The melt-pond–sea-ice model combines a horizontal cellular automaton with a vertical one-dimensional thermodynamic model to simulate the horizontal and vertical growth of melt ponds on a sea-ice floe. The domain represents a 200 m $\times$ 200 m section of a sea-ice floe. The cellular automaton comprises a grid of 40$\times$40 cells each with a horizontal

surface that represents 25 m^2 and variable depth. For every cell the melt or growth rate of the ice is calculated using the thermodynamic model. Sea level with respect to the floe is modelled and transport of water across or through the ice is modelled with Darcy's Law for flow through a porous medium. Transport of water across the sea-ice surface is modelled by the transfer of water between cells, a group of cells with a surface of water form a melt pond.

1.7 Structure of Thesis

Chapter 2 sets the model developed in this thesis into its scientific background, introducing several previous melt-pond – sea-ice models. In chapter 3, I develop a cellular-automaton melt-pond–sea-ice model. Due to lack of suitable ice and snow topography data in chapter 4 I introduce a stochastic method used to create ice and snow topographies that are used as initial conditions for the melt-pond–sea-ice model developed for this thesis. In chapters 5 and 6, I present standard case first-year ice and multi-year ice simulations and compare them to sensitivity studies in which I vary ice and snow topographies and vertical ice permeability. I show that model output is insensitive to changes in ice topography that are statistically similar. Finally, in chapters 7 and 8, I compare the melt-pond–sea-ice model to previous models and observations and show how the model advancements described in this thesis have enhanced our understanding of the physics that underlies pond formation and confirmed the importance of sea-ice topography in governing the fraction of the ice surface covered in ponds.

Chapter 2

Critical Analysis of Previous Melt Pond Models

2.1 Introduction

This chapter aims to provide a summary of the main developments in the modelling of sea ice, in particular a description of sea-ice models that include a melt-pond parameterisation. Early sea-ice thermodynamic models such as those presented by Semtner (1976) and Maykut & Untersteiner (1971) did not include any pond parameterisation. The first sea-ice model to include a melt-pond parameterisation was the sea-ice model of Mellor & Kantha (1989), here a portion of melt water is retained at the sea-ice surface. The water did not have any impact on surface albedo and did not act as a latent heat store. The retained surface water is transformed into ice again in the autumn so that the presence of ponds increased ice thickness. It was, however, recognised that sea-ice thickness did have a sensitivity to melt ponds.

A driving motivation for modelling melt ponds on sea ice is to establish a melt-pond representation that is simple enough to be included in the sea-ice component of global

climate models. To do this it has been recognised that the sea-ice and melt-pond model has to have a foundation in the physics that governs melt pond growth, if pond growth is expected to be realistic. The Ebert & Curry (1993) and Ebert *et al.* (1995) models were the first sea-ice models to include a melt pond parameterisation that affects the sea ice surface and these are described in section 2.2; section 2.3 examines the small-scale sea-ice model by Taylor & Feltham (2004), this models the physical processes that govern the evolution of melt-pond depth and sea-ice thickness; section 2.4 examines the Lüthje *et al.* (2006) model which is a cellular automaton, this is the first model to investigate the horizontal evolution of melt ponds over a summer melt season; section 2.5 describes the Flocco & Feltham (2007) model which offers a physically-based parameterisation of melt ponds building on the results of the Lüthje *et al.* (2006) model and is designed to be included in a Global Climate Model.

2.2 The Ebert & Curry (1993) and Ebert *et al.* (1995) Models

The Ebert & Curry (1993) model was the first sea ice model to include a physically-based melt-pond parameterisation. Through modelling the physics with more precision than earlier models the model described in Ebert & Curry (1993) aimed to examine feedback loops between sea ice and the atmosphere and examine the sensitivity of ice thickness to surface albedo. Ebert & Curry (1993) also investigated whether the sea ice components used in global climate models are accurate enough to provide results which reflect reality. The Ebert & Curry (1993) model uses the Maykut & Untersteiner (1971) model as its base and improves on it by using a radiation model to calculate the radiation that reaches the ice surface and the radiation that penetrates the ice rather than using the potentially low estimate used in the Maykut & Untersteiner (1971) model. Ice thickness was previ-

ously found to be very sensitive to changes in surface albedo, Shine & Henderson-Sellers (1985), and therefore an albedo scheme following the albedo scheme described in Shine & Henderson-Sellers (1985) was included in the Ebert & Curry (1993) model. In this scheme albedo depends on snow cover, state of snow cover (dry snow or melting snow), ice thickness, ice optical properties (which are dependent on ice age), and surface state; spectral variation and dependence on the solar zenith angle are parameterised and the total albedo is weighted by the proportion of diffuse and direct radiation. Most important to this discussion is that the melt-pond parameterisation affects the surface albedo. This model concentrates entirely on the thermodynamics of sea ice, but does include a lead fraction.

The Ebert & Curry (1993) model represents a portion of sea ice that has uniform depth and is horizontally homogeneous. A one-dimensional, nonlinear, heat-diffusion equation is solved in the sea ice and fractional surface properties are prescribed. The model can represent winter and summer sea ice. In winter the ice surface is covered in snow. Snow can accumulate at a rate externally prescribed and in summer months it can melt away. Unlike most other models precipitation continues throughout the summer. Heat-conduction equations are solved for the snow layer and the internal snow temperature is calculated. The temperature is assumed to be continuous across the snow–sea-ice boundary. Sea ice is split into two layers, a thin layer at the surface of the ice where most of the radiation is absorbed and a larger internal layer following Maykut & Untersteiner (1971). Sea ice is assumed to be a solid but brine pockets, which are a source of latent heat and therefore slow ice growth and melt rates, are taken into account implicitly. The model is forced by prescribed shortwave and longwave radiation, which is calculated from a coupled radiation model run using a radiation model described in Curry & Ebert (1992). When ice or snow is not melting the total heat flux leaving the ice or snow must be equal to the total flux

entering the surface of the ice or snow, this allows the surface temperature of the ice or snow to be calculated. During melting the surface temperature of the ice or snow is forced to be at its melting temperature. The heat flux out of the ice or snow is then calculated assuming this surface temperature and the net heat flux at the surface determines the rate of melting.

During summer when snow has melted a pond parameterisation is activated. A prescribed fractional area of each surface type is assumed to be covered with ponds. The pond covered area begins at its maximum coverage and reduces steadily to its minimum over the course of a month. The maximum fraction of the surface are covered with ponds is 0.25 and the minimum is 0.1. Pond depth is established from the amount of heat flux into the melt pond, therefore ponded ice melts at an enhanced rate.

Since the model represents a large area of sea ice, melt water run off must be modelled. Only 0.15 of the total water produced remains at the surface in ponds with the remainder lost from the ice surface through leads. The fraction of water lost was established through sensitivity studies. Pond depth has a prescribed maximum, this is chosen to be 0.8 m, which is a reasonable average over the entire summer season. In the winter months the sea-ice surface is immediately returned to ice and latent heat stored in the pond is added to the total flux emitted from the ice surface.

Leads are modelled by assuming that a fraction of the total area is open water. Incoming heat flux is absorbed straight into the ocean. This affects the heat flux at the base of the ice allowing for a more accurate calculation of basal melting, which depends mainly on the heat flux due to leads and not on the temperature of the mixed layer of the ocean.

Radiation absorbed in the sea ice is calculated using Beer's Law, this means that the albedo of the surface must be prescribed. Surface types are each prescribed an albedo and the total albedo is a weighted fraction of the albedo from each surface type. The surface

types taken into account are open water, dry snow, melting snow, bare sea ice, and ponded sea ice.

Sensitivity tests were undertaken in order to discover the sensitivity of sea-ice thickness to model parameters and to identify feedback loops. The parameters about which there was most uncertainty were tested. Significantly the main areas where there existed uncertainty were connected to melt ponds. Sea-ice thickness was found to be most sensitive to the run off fraction. The run off fraction affected melt-pond depth and melt-pond volume directly and this affected the surface albedo. Increasing the volume of surface melt water reduces the surface albedo of the sea ice, this increases the heat flux into the ice surface which then increases the volume of melting of the ice. The additional melt increases the pond depth and volume of surface water further, this is identified as a feedback loop.

Changes in the minimum and maximum pond fraction were also found to have a large effect on sea-ice thickness. When melt ponds were ignored, the equilibrium sea-ice thickness increased from 2.88 m in the standard case to 5 m. When a maximum pond fraction greater than 0.55 was used the sea ice melted away entirely in the summer months. This model therefore clearly identifies surface area covered in melt ponds as an important factor in establishing sea ice thickness.

The impact of pond depth on sea ice thickness is only small, despite the albedo of sea ice depending on pond depth. A low maximum pond depth is enforced, this limits the minimum albedo which suppresses any feedback. If pond depth were able to evolve freely it is probable that a more significant sensitivity would have been found.

The surface albedo feedback loop was found to be the main way in which melt ponds affected sea-ice thickness. The decrease in the total average albedo caused an increase in surface ablation in the model. There was more surface ablation than the Maykut & Untersteiner (1971) model, which did not include a melt-pond parameterisation.

The melt-pond parameterisation was recognised as an essential part of a sea-ice model. The surface albedo is the area of most uncertainty and therefore this along with a more realistic criteria for the run off fraction are most desirable to improving the Ebert & Curry (1993) melt-pond–sea-ice model. The model described in Ebert *et al.* (1995), which builds on the Ebert & Curry (1993) model, goes some way to improving the melt-pond parameterisation. The aim of the Ebert *et al.* (1995) model is to examine in more detail the distribution of absorbed radiation through the sea ice with a particular emphasis on the melt-pond parameterisation.

The Ebert *et al.* (1995) model uses as its foundation the model described in Ebert & Curry (1993) along with the radiation model described in Curry & Ebert (1992). The enhancements in this version are the inclusion of ice thickness categories. In the previous model sea ice was assumed to be a horizontally homogeneous slab; in this model the volume of ice is made up of smaller volumes of ice with different thicknesses and properties. In this way new first-year ice is represented as well as thick ridged ice. In total there are fifteen ice categories, each category has its own melt pond fraction. Each ice category makes up part of the total fractional area, the area of each ice category depends on the relative abundance of that ice type in reality. Minimum and maximum pond fractions are again prescribed, for first-year ice these are 0.5 and 0.9 and for multi-year ice 0.1 and 0.25. Pond depth is allowed to grow to be at most half the thickness of sea ice in that category. Limiting the pond depth still causes inaccuracies in radiation absorbed and stored in the ice. The new melt-pond parameterisation also allows radiation into ice below a pond which can heat the pond. The long term impact on ice thickness due to this however is not examined because the model simulates a summer season only.

The pattern of pond coverage is reasonable with pond coverage being at its maximum when melt ponds first appear. Pond coverage then decreases as pond depth increases

later in the season. Simulations of the Ebert *et al.* (1995) model showed that melt ponds caused an increase of shortwave radiation transmitted into the interior of the sea ice by fifty percent.

The Ebert & Curry (1993) model and the Ebert *et al.* (1995) model are sophisticated sea-ice models and highlighted the importance of understanding the sea-ice–albedo feedback mechanism. A limitation of those models are the assumptions that had to be made about area covered in ponds, pond depth and run off fraction. Additionally, since the increase in incoming radiation is responsible for pond formation, in order to model surface melting more accurately it is necessary to calculate radiation absorption and surface albedo more realistically.

2.3 The Taylor & Feltham (2004) Model

The model described in Taylor & Feltham (2004) is a one-dimensional sea-ice model that simulates a detailed vertical evolution of a single slab of ice and its developing pond. Ice dynamics are not modelled. The model allows surface albedo to be calculated rather than prescribed. This model has been developed to examine the influence of radiation on melt-pond depth.

The radiation model used in the Taylor & Feltham (2004) model is a reduced version of the radiation model described in Perovich (1990). The Perovich (1990) sea ice model is split into a number of layers that may have differing optical properties whereas Taylor & Feltham (2004) simplifies this by considering sea ice to be a single optical layer. The Perovich (1990) radiation model calculates spectral albedo and transmittance of snow and ice given their extinction coefficients and scattering properties. Upwelling and downwelling radiation is determined, leading the model to be described as a two-stream model. It is assumed that there is no reflection at the interfaces between layers of different properties

and no upwelling radiation from the base of the sea ice. The Perovich (1990) radiation model is incorporated into the Taylor & Feltham (2004) model with the additional assumption that sea ice is vertically homogeneous with respect to the optical properties. Taylor (2003) showed that the assumption of vertical homogeneity was satisfactory in a two-stream model with suitably averaged optical properties. The layers in which irradiance is evaluated are melt pond, ice covered internal melt region and ice. There is a snow depth prescribed in the model, however snow is assumed to be so effective at reflecting radiation and absorbing radiation at the surface that none is transmitted. The advantage of this radiation model is that the surface albedo can be calculated for optical properties that can be estimated empirically.

Heat transport through sea ice uses the mushy-layer model, Feltham *et al.* (2006). A mushy layer consists of a rigid matrix of pure solid (ice) bathed in its impurity rich melt (brine). Sea ice is well-modelled as a mushy layer formed from sodium-chloride solution.

Heat transport through the snow is modelled with a heat-diffusion equation as in Ebert & Curry (1993). The pattern of snow fall is identical to that of Maykut & Untersteiner (1971). The external parameters that force the model are the parameters needed to calculate sensible heat flux and latent heat flux at the surface and base of the ice. These parameters are incoming shortwave and longwave radiation, air temperature, specific humidity, average wind speed, and ocean heat flux. The temperature at the base of the ice is fixed so that the moving boundary as ice melts and freezes can be modelled with the Stefan condition.

Vertical drainage of melt water through the sea ice is constant, in the standard case the drainage rate is 2 cm day^{-1}.

In the standard case this model showed good agreement with SHEBA results. Ponds developed initially several days later than observations but several days before the Ebert

& Curry (1993) and Ebert *et al.* (1995) models. Melt-pond surface albedo decreases continually from pond formation until freeze up although a maximum pond depth of 0.33 m is reached earlier in the melt season. Winter ice regrowth did not begin until day 322, internal ice temperature as freeze up took place was found to be higher than the ice temperature determined by the Maykut & Untersteiner (1971) model at the same time, thus demonstrating the impact of the latent heat store. The higher temperatures meant that at the end of the year the ice thickness was 0.177 m less than the initial ice thickness of 2 m.

Sensitivity studies found that maximum pond depth was most sensitive to the fraction of incident radiation that was absorbed into the interior of the melt pond, which is affected by changes in the cloud cover and is therefore somewhat uncertain. Maximum pond depth was also found to be sensitive to the drainage rate which is constant in this model. An increase in snow depth caused an increase in maximum pond depth since the extra initial surface melt water lowers the albedo at the start of the season and causes an increase in melting over the season.

The Taylor & Feltham (2004) model has improved the physical understanding of melt ponds and provided several more areas of study. In particular it highlighted the impact of snow cover on pond depth and ice thickness, and uncertainty in pond drainage and the radiation parameters.

2.4 The Lüthje *et al.* (2006) Model

The sea-ice model presented in Lüthje *et al.* (2006) simulates the horizontal as well as the vertical evolution of melt ponds in order to investigate which parameters affect the area covered in melt ponds and total surface ablation. The region modelled is a 125 m $\times$ 125 m sea-ice floe, which is split into 2.5 m wide grid cells each of which have an individual ice

thickness. The model focusses on water transport within this area. Melt water formation and vertical drainage in each cell evolve independently of other cells, melt water is transported between cells to simulate horizontal water transport. Run off through leads and mechanical ice deformation processes are not modelled. Ice depths are given every 2.5 m, ice depth is assumed constant over this distance and equations solved in each grid cell are one dimensional. Thus the grid can be supposed to be made up of rectangular prisms with square horizontal surfaces and differing vertical thickness. The surface of each grid cell can be either bare ice or ponded ice (so the minimum pond area is the surface area of a cell which is 6.25 m^2). The model simulates melt pond evolution over a single summer melt season. The processes modelled are ice melting and water transport horizontally between cells or vertically through a cell. Each grid cell is initially in hydrostatic equilibrium.

Bare ice melting is assumed to take place at a fixed rate. To take into account the increased melt rate when ponds are present, the melt rate, m, of ice beneath ponds is given by

$$m = Em_i, \tag{2.1}$$

where m_i is the melt rate of bare ice, E is the factor by which melting is enhanced. It is assumed that there is a maximum depth of pond beyond which melt rate is no longer enhanced, h_{max}. The enhancement factor is given by

$$E = \left(1 + \frac{m_p h_{pond}}{m_i h_{max}}\right), \tag{2.2}$$

where m_p is a constant parameter and pond depth is h_{pond}. When pond depth is greater than h_{max} the enhancement factor is given by

$$E = 1 + \frac{m_p}{m_i}. \tag{2.3}$$

The model is initialised by converting freeboard determined from laser altimetry data into depth using hydrostacy and assumed densities. The laser reflects from the snow surface, when present, and the topography obtained from the altimetry data therefore gives a combined snow and ice depth. The Lüthje *et al.* (2006) model does not discriminate between snow and ice melt. Several initial topographies were specified so first year ice and multi year ice could be considered separately and differences between them highlighted. Melting at the base of the ice is not modelled.

Vertical drainage in every cell takes place at a fixed rate of 0.8 cm day^{-1} in the standard case, which is much lower than the vertical drainage rate of 1.2 cm day^{-1} in Taylor & Feltham (2004). It has been suggested, Eicken *et al.* (2002), that ponds drain rapidly to sea level in the space of a few hours, however in this model, since sea level is not modelled, using a more realistic drainage rate would cause melt ponds to disappear entirely.

Once vertical drainage has taken place in every cell, horizontal drainage between cells takes place if there is any water still available. Horizontal drainage is modelled by Darcy's Law, which defines the rate of flow through a porous medium due to a hydraulic pressure gradient.

The Lüthje *et al.* (2006) model was able to simulate known patterns of pond coverage for first-year and multi-year ice, with first-year ice having a larger portion of the area covered in ponds which are large and shallower than on multi-year ice. Comparison of the standard case with observations, Tschudi *et al.* (2001), Nazintsev (1964), Perovich *et al.* (1999), shows that this model overestimates melt pond coverage for 29 days of the melt season.

It was found that the area covered in melt ponds was controlled most strongly by topography. However changes in horizontal permeability also affected the area covered with ponds. Horizontal permeability caused a fractional increase in pond coverage of 0.2

when it was reduced by 2 orders of magnitude. The effect on surface ablation of altering horizontal permeability was much smaller.

The total ablation in this model is 0.92 m in the standard case, this is the same as the standard case value in Taylor & Feltham (2004) but greater than the standard case values in earlier models, Ebert & Curry (1993), Ebert *et al.* (1995). The smaller ablation in these earlier models is probably due to the run off fraction. Lüthje *et al.* (2006) and Taylor & Feltham (2004) models are the only models which do not prescribe a run off fraction.

2.5 The Flocco & Feltham (2007) Model

A driving motivation for developing high resolution melt-pond models is to gain an understanding of the evolution of melt ponds and their impact on other sea-ice parameters so that a parameterisation of melt ponds can be included in global climate models. The model developed by Flocco & Feltham (2007) is a melt-pond–sea-ice model that offers a method for including a physically based melt-pond parameterisation in a global climate model. This model uses the sea-ice thickness distribution models used in current climate models such as CICE (the sea ice component used in the Hadley Centre Global Climate Model) and simulates the physical processes of ice melting, water redistribution and pond drainage.

The Flocco & Feltham (2007) model simulates ice melting, water redistribution and vertical drainage. Only the summer melt season is modelled therefore no ice refreezing takes place. Other simplifications are that bare ice and snow melt rates are fixed in the same manner as Lüthje *et al.* (2006) and snow thickness is distributed randomly between ice classes. In the standard case no run off is modelled.

Sea ice is described by the Thorndike *et al.* (1975) ice thickness distribution function. The Thorndike *et al.* (1975) model proposes the change in distribution of sea-ice thick-

ness with time is a result of thermodynamic processes (melting and freezing), mechanical deformations (such as ridging) and advection. For simplicity in sea-ice model components of global climate models, the ice-thickness distribution is divided into a number of discrete classes. Once ice thickness changes due to melting, for example, ice thickness is redistributed between classes and the fractional area of each ice class is updated.

The Flocco & Feltham (2007) model aims to improve on the thermodynamic section of the ice distribution model by including a melt-pond parameterisation, therefore the dynamic sections of the sea-ice thickness distribution function are ignored.

In the Flocco & Feltham (2007) model it is assumed that the ice in each ice thickness category is in hydrostatic equilibrium initially and the total volume of ice represented will be in hydrostatic equilibrium continually. This assumption is reasonable and allows the ice to evolve so that regions can be below sea level throughout the melt season. The ice-thickness distribution is split into two separate ice-thickness distributions, one represents the ice thickness above the sea level initially, this is the surface thickness and the other represents ice thickness below the sea level initially, this is the basal thickness. The basal-thickness distribution and the surface-thickness distribution evolve separately. The advantage of this method is that the effects of topography, which cannot be represented explicitly, can be parameterised.

The process of melting is modelled in an analogous way to that of Lüthje *et al.* (2006). Bare ice melts at a fixed rate and ponded ice melts at an enhanced rate that depends on the depth of melt pond at that location. Basal melt rate is constant. Every ice thickness class is covered with a random snow cover initially, once snow melt begins snow is forced to melt at a rate enhanced by a factor of 10. This approximation is suitable here as the purpose is to model pond evolution and snow cover merely provides an initial volume of water to form ponds.

Once melt water is formed the total volume of melt water is redistributed so that the ice category with the lowest surface height is filled first. Once the water depth reaches the surface height of the next lowest ice category the same process takes place and so on until all the melt water produced has been redistributed. The lowest surface height category is always filled first and the thickest ice surface category is filled last. In this way an approximation of melt water redistribution on a small scale is reproduced.

Melt water is removed from the ice surface through vertical drainage, modelled by Darcy's Law for flow through a porous medium. Vertical permeability evolves with time.

In the Flocco & Feltham (2007) model, melt water that does not drain vertically out of the ice is all used in pond formation. In reality the volume of water that runs off is unknown and most estimates appear to have little or no physical basis, Maykut & Untersteiner (1971), Ebert & Curry (1993). This has an immediate effect on pond depth and pond coverage. Here pond depths are deeper than other modelled pond depths for this reason, however pond area covered shows a good agreement with observations. The inclusion of a run off parameter had the effect of lowering pond depth and maximum area covered in ponds, but only by 1%.

The model was able to effectively simulate the thickness distributions of first-year and multi-year ice. An initial first-year ice thickness distribution resulted in 66% of the surface covered in ponds at maximum coverage, compared with an initial multi-year ice thickness distribution resulting in an area covered in ponds as 43%.

Sensitivity of pond fraction, pond depth and ablation to snow was investigated. With no snow cover a maximum pond fraction of 43% was reached and overall there was less melt water produced. Due to the fixed melt rates in the Flocco & Feltham (2007) model, that have been established through sensitivity studies in Lüthje *et al.* (2006), it is impossible to investigate the true role of snow cover. A thick snow cover agreed more closely with

observations, causing an increase in maximum pond depth and a decrease in area covered in ponds since the snow took longer to melt.

Reducing the number of ice categories, which is equivalent to making the ice surface smoother, caused vertical percolation back into the ice, reduced the pond depth and increased pond coverage, although the model was still able to simulate a pond coverage that has a good agreement with the current knowledge of pond coverage.

2.6 Conclusions

The sea-ice–melt-pond models described in this chapter provide a background to the model developed for this thesis. The Ebert & Curry (1993) and Ebert *et al.* (1995) models are physically based sea-ice models that identified melt ponds as important to the mass balance of sea ice and also as playing a role in the ice–albedo feedback mechanism. However a limitation of the Ebert *et al.* (1995) model is that the melt pond fraction and melt pond depth are not allowed to evolve independently but are constrained by assumptions, hence the true nature of the influence that melt ponds have on ice thickness and extent is not revealed with this model.

The Taylor & Feltham (2004) model is the first model that really investigates the physical processes that govern ice melting together with pond formation. Since this model is one-dimensional neither the influence of topography nor the horizontal evolution of melt ponds can be investigated. However, this model provides a sophisticated representation of the one dimensional evolution of the melt-pond–sea-ice system and is used as a component of the melt-pond–sea-ice model described in this thesis.

The Lüthje *et al.* (2006) model has several important limitations. In particular, the model governing water transport is far too simple: vertical drainage is assumed to be constant, whereas observations suggest that vertical drainage takes place rapidly and at

varying rates over the melt season. Vertical drainage rate is determined by the hydraulic head, that is the height of the melt pond surface above sea level, and the vertical permeability of the underlying ice, neither of which are modelled in Lüthje *et al.* (2006). As well as this melting of bare ice is assumed to take place at a fixed rate with no adjustments taken into account for the time of year, refreezing is not modelled and no differentiation is made between snow and ice melting. As it stands this model cannot be used to assess the role that ice topography plays in pond cover, however the cellular automaton design is a time effective method for modelling areas of the sea-ice surface. The cellular design is used as the basis for the melt-pond–sea-ice model described in this thesis.

As mentioned in chapter 1 the goal of the melt-pond–sea-ice model described in this thesis is to improve our understanding of the physics that govern the melt pond cover and to investigate the sensitivity of melt pond cover to snow and ice topography and permeability in order that a more physically based melt pond parameterisation can be developed for inclusion in global climate models. The Flocco & Feltham (2007) model is an example of a physically based parameterisation and has been included here so that comparisons can be made with the small scale model developed for this thesis and a model intended to be used within a global climate model.

The remaining chapters of this thesis develop a melt-pond–sea-ice model that combines the Taylor & Feltham (2004) model with aspects of the Lüthje *et al.* (2006) model. This three-dimensional sea-ice model models heat transport through sea ice in a similar manner to that of Ebert *et al.* (1995) with the additions of an improved radiation model that allows albedo to be determined and a small-scale topography model following the cellular automaton approach of Lüthje *et al.* (2006) but with a more realistic treatment of meltwater transport.

Chapters 3 and 4 present the melt-pond–sea-ice model and the method used to generate

an ice topography. Model results are presented in chapters 5 and 6 and chapter 7 includes a section where the results of the melt-pond–sea-ice model are compared to the results of models described in this chapter.

Chapter 3

The Model

3.1 Introduction

The model described in this chapter combines the one-dimensional thermodynamic model of Taylor & Feltham (2004) with the cellular automaton design of the Lüthje *et al.* (2006) model described in chapter 2. Water transport across and through the sea ice is defined by the cellular automaton model and melting and freezing processes are described by the one-dimensional thermodynamic model. The treatment of meltwater drainage presented here allows the hydraulic head of melt ponds to be calculated and the permeability of the ice to vary, in contrast to earlier models. The model described in this chapter represents an arbitrary section of the sea-ice surface. A topography model, described in chapter 4, was used to create a realistic sea-ice surface topography so that the physical surface of sea ice and its interactions with surface water can be accurately represented. Thus the model described in this chapter is an improvement on the earlier sea-ice models described in chapter 2. The purpose of the model described here is to simulate the physical processes that govern the thermodynamics and hydrology of a sea ice floe in order to investigate the vertical and horizontal evolution of surface melt ponds and their dependence on snow and ice initial topographies.

The vertical heat transport model is applied in every cell of the automaton and is based on the one-dimensional thermodynamic model described in Taylor & Feltham (2004) and in Chapter 2. Although the cellular automaton model uses the same cellular evolution concept of the model described in Lüthje *et al.* (2006) the model described in this thesis has been redesigned entirely and includes a number of improvements and additions to the cellular automaton model described in Lüthje *et al.* (2006), these are: the entire modelled domain is positioned in hydrostatic equilibrium and sea level with respect to the floe is monitored and evolves with time as the mass of the modelled floe changes; the vertical and horizontal drainage rates of water through the ice are modelled by Darcy's Law; there is a permeability model that allows horizontal ice permeability to vary with time linked to the solid fraction of the ice (this varies and is described by the mushy-layer equations that model heat transfer); there is a separate snow cover topography that melts at a rate dependent on the temperature of the snow; and, finally, the topography model, described in chapter 4, allows snow and ice topography to be generated based on statistical characteristics of the ice and snow, the ice surface and base heights are generated separately which allows cells to be initialised with surface heights below sea level. The topography model does not model ridged ice, due to lack of relevant measurements of the thickness and statistics of heavily flawed ice.

The cellular model simulates melt-pond evolution across a horizontal grid, and consists of cells that each represent a volume of sea ice. The one-dimensional thermodynamic model is applied individually to each cell, and models heat transport through snow, water and ice; hence melt-water production and surface albedo are captured. The cellular model was programmed using C++, with each cell calling a separate one-dimensional thermodynamic model written in C++ by Taylor (2003) for his PhD thesis. It is necessary to run the thermodynamic model at a lower spatial and temporal resolution than in Taylor

& Feltham (2004), firstly due to time constraints in running the model but also to ensure that the cellular automaton and thermodynamic sub models are of comparable accuracy. The resolution of the thermodynamic module was tested in isolation from the cellular automaton model to ensure that the lower resolution results were not significantly different from the higher resolution results. The resolution chosen for the thermodynamic module was the highest resolution that could be used within the time constraints.

Initial ice and snow topographies were generated using a stochastic spatial data model, calibrated using data from the SHEBA field experiments. The generation of the surface topographies is discussed in detail in Chapter 4.

The cellular automaton model and the processes by which water is removed from cells and transferred from cells is described in section 3.2. In section 3.3 the vertical heat transport model, which is applied in every cell, is described.

3.2 Cellular Automaton

3.2.1 The Cellular Domain

The cellular automaton grid consists of a group of cells that evolve largely independently of one another, but do, however, interact through the transport of water between cells. Each cell represents a square area of sea ice that is 25 m^2. Within each 25m^2 cell, ice thickness, melt water depth and snow cover are assumed to be uniform. The grid contains 40×40 cells, therefore the entire grid represents a 40 000 m^2 area of a sea-ice floe. The area of the grid is constrained to this size so that it can represent an arbitrary section of a sea-ice floe without the complication of having to take edge effects into consideration. The boundaries of the grid are periodic: melt water transported out of any edge cell is transported back into the opposite edge cell. This means that the fraction of melt water lost to the ocean through leads is neglected. If a cell melts completely then subsequent water transport into

this cell is lost to the open ocean. A schematic of the cellular automaton model is shown in figure 3.1

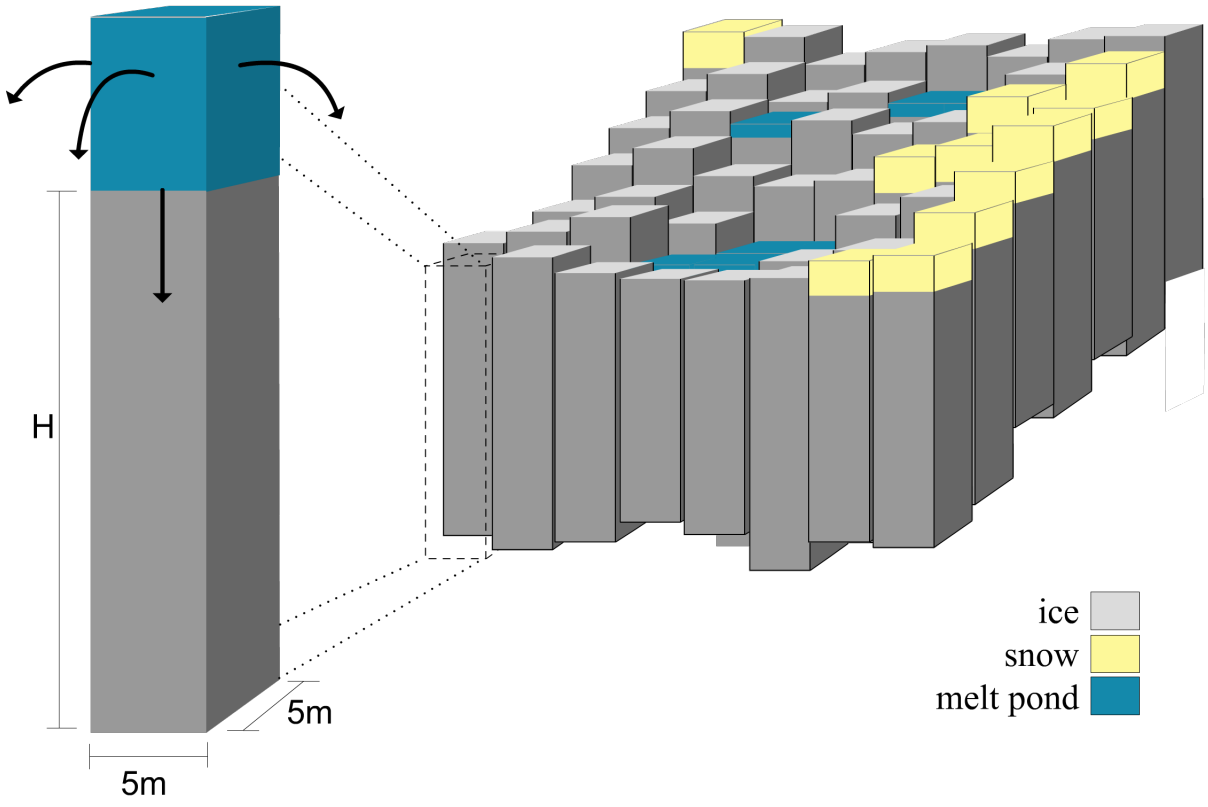

Figure 3.1: A schematic diagram of the cellular automaton. Each cell has an individual ice thickness, H, and has a horizontal surface area of 25 m^2. Melting decreases the ice thickness in a cell and allows a pond to form on the surface. Water can drain through a cell or can be transported to adjacent cells.

An outline of the chronology of the processes modelled is as follows: (1) One-dimensional thermodynamic equations, described in section 3.3, are solved in the vertical direction in every cell to calculate the heat flux through the ice, snow and melt water (if it exists). (2) These calculations establish the volume of melt water produced, basal ablation and the saturation of the snow on a cell by cell basis. Snow becomes saturated as its temperature increases and the first ponds form from melted snow. Before the snow cover has entirely melted water trapped within the snow can be transported horizontally to adjacent cells.

The initial pond depth depends on the saturation of the snow at the instant the snow melts through completely. (3) Each time step water flows between adjacent cells, driven by differences in hydraulic head between the cells. Sea level with respect to the floe is established and is used to calculate hydraulic head in each cell. The volume of horizontal water transport into adjacent cells is calculated using Darcy's Law for flow through a porous medium. (4) Vertical drainage through the ice in each cell is calculated using Darcy's Law for flow through a porous medium. (5) The volume of water transported in and out of cells is updated and one cycle of the automaton is complete.

The simulated physical processes that comprise the model are described in the following sections. These are the calculation of sea level, horizontal and vertical water transport, and ice permeability which determines the velocity of water transport.

3.2.2 Sea Level and Hydrostatic Equilibrium

The surface of sea ice is deformed by mechanical processes such as ridging, or thermodynamic processes such as the formation and drainage of melt ponds and the freezing over of partially drained ponds, Fetterer & Untersteiner (1998), and therefore in places the sea-ice surface is likely to have a negative freeboard. Therefore the assumption of cell-wise hydrostatic equilibrium is unrealistic. In this model the entire floe is in hydrostatic equilibrium but not individual cells. Assuming the floe is in hydrostatic equilibrium the initial position of the surface of the sea with respect to the floe can be established, after this changes in sea level are updated as mass is removed from the surface and base of the ice.

The initial ice topography is created by combining two grids of ice thicknesses. One thickness represents the depth of ice below sea level, called the basal thickness, the other represents the difference in height between the ice surface and sea level. Basal thicknesses must be positive values but surface thicknesses can be either positive or negative. These

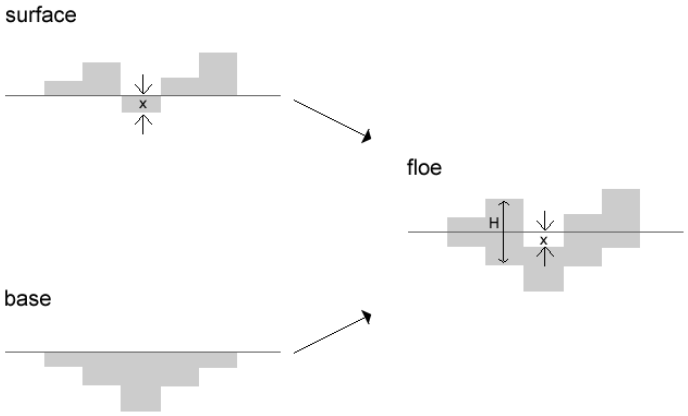

Figure 3.2: Ice depth below sea level is combined with ice surface height above sea level (which includes negative values), creating a floe with cells which have an initial negative surface height.

are combined to give the ice thickness in each cell, this is illustrated in figure 3.2. Sea level is adjusted and an additional snow layer is added to each cell. Mean draft, D, is calculated in every timestep by

$$D = \frac{\sum(x_i + x_s + x_p)}{\rho A}, \tag{3.1}$$

where x is mass of ice, snow and water in each cell, index i represents ice, s represents snow, and p represents melt pond, ρ is water density, and A is total floe area.

3.2.3 Hydrology

Area covered in melt ponds is affected by horizontal and vertical water transport, Eicken *et al.* (2002). Water can be removed from the grid by vertical drainage. Water can be transported between cells by horizontal drainage which depends on the difference in hydraulic head between cells. Vertical and horizontal drainage are calculated in each cell.

Vertical and horizontal water transport are described by Darcy's Law which is an empirical law for flow through a porous medium. The fluid flux, or Darcy velocity, q is

given by

$$q = -\frac{\prod}{\nu}\nabla(p - \rho g z), \tag{3.2}$$

where $\prod$ is the permeability tensor, ν is the kinematic viscosity, a property of the fluid, p is pressure, ρ is the fluid density, g is gravitational acceleration, Bear (1988). We assume for simplicity that sea ice is a saturated media.

In the vertical direction the Darcy velocity, v, reduces to

$$v = -\pi_v \frac{g\rho_m}{\mu}\frac{z_h}{H}, \tag{3.3}$$

where π_v is the vertical ice permeability, g is gravitational acceleration, μ is dynamic viscosity, which, for water is 10^{-3} kg m^{-1} s^{-1}, ρ_m is the density of melt water, which is initially formed from melted snow, and is taken to be 1000 kg m^{-3}, z_h is the vertical component of the hydraulic head, which is the height of the melt pond surface above sea level and H is ice thickness.

In the horizontal direction the Darcy velocity, u, is given by

$$u = -\pi_h \frac{g\rho_m}{\mu}\nabla\psi, \tag{3.4}$$

where π_h is the ice permeability in the horizontal direction, and ψ is the fluid surface height. In the horizontal direction the Darcy velocity is dependent on the gradient of hydraulic head between cells.

Vertical and horizontal water transport is described by equations 3.3 and 3.4. If there is insufficient melt water in a cell then melt water distribution is calculated using the following method: there are four horizontal directions in which water can potentially be transferred, therefore the cell with the greatest difference in hydraulic head receives its allocation of water first, then the next biggest hydraulic head gradient and so on, so the

adjacent cell with the smallest hydraulic head gradient receives water flux last, if there is any water remaining. Because the permeability at the ice surface is higher in the horizontal direction than in the vertical direction any melt water transport horizontally is calculated first and the volume of vertical drainage is calculated if there is any water remaining in the cell.

Flooding of the sea ice, the process by which sea water is forced up through the sea ice to the ice surface when the ice surface height is below sea level is not modelled. This is because at the start of the melt season the ice is too impermeable for this process to be possible. Later in the season, when the sea ice is permeable enough to allow flooding, the ice surface has ponds which are deeper and have surfaces at sea level in which case flooding would not occur.

3.2.4 Permeability

Permeability in sea ice is a result of its matrix structure (see Chapter 1). Brine pockets or pores connect and create drainage channels in the sea ice. To maintain local thermodynamic equilibrium the size of the pores will adapt in response to heat transfer. The structure of the pores can be split into two pore types: primary pores and secondary pores. Primary pores are the brine pockets that form during the initial formation of sea ice. Primary pores will usually have a diameter of 0.1 mm or smaller. As the ice ages brine drainage causes primary pores to increase in size until they form vertical channels with smaller channels connected to the sides, Freitag & Eicken (2003), at this stage they become classified as secondary pores. Secondary pores are much larger in size, from 0.1 mm to several mm. Secondary pores are the pores that determine the permeability of sea ice. The permeability can vary with the age of the ice, the type of ice, and the temperature of the ice.

The studies by Freitag & Eicken (2003) and Eicken *et al.* (2002) noted that ice per-

meability varied by several orders of magnitude between the early and late melt season and by several orders of magnitude due to ice type. Freitag & Eicken (2003) measured vertical sea-ice permeability to be in the region of $10^{-11} - 10^{-7}$ m^2 whilst Eicken *et al.* (2002) found a minimum measurable vertical permeability of 6×10^{-12} m^2 with a mean of 2×10^{-10} m^2.

Horizontal permeability was found to have a mean value of 4.3×10^{-12} m^2 by Freitag & Eicken (2003), just one order of magnitude smaller than the minimum vertical permeability. Eicken *et al.* (2002) found that some horizontal permeabilities were between 4.4×10^{-12} m^2 and 4×10^{-10}m^2 which is the same range as vertical permeabilities.

Golden *et al.* (2007) introduced a semi-empirical parameterisation for vertical permeability. Vertical permeability, π_v is determined by the solid volume fraction, ϕ, of ice,

$$\pi_v = 3 \times (1 - \phi)^3 \times 10^{-10} \text{ m}^2. \tag{3.5}$$

In the model described here vertical flow is limited by the lowest permeability in a vertical column. During the melt season this occurs at the base of the sea ice, where the solid fraction is considered to be constant since the temperature is fixed at the freezing temperature of sea water. In this case the vertical permeability does not vary with time and we take its value to be $\pi_v = 2.4 \times 10^{-12}$ m^2. This permeability is at the low end of the scale of observational results, however even with a permeability of this scale ponds drain to sea level in a matter of hours.

There is no corresponding model for horizontal permeability, but since permeability in the horizontal direction at any depth within the sea ice is expected to be lower than the permeability in the vertical direction at the same depth, due to the columnar structure of sea ice, we assume that horizontal permeability will always be two orders of magnitude smaller than vertical permeability, following Feltham *et al.* (2006). Horizontal ice

permeability is determined by

$$\pi_h = 3 \times (1 - \phi)^3 \times 10^{-12} \text{ m}^2, \tag{3.6}$$

where ϕ is the solid fraction at the upper ice surface.

Figure 3.3: An ice core showing the deteriorated, porous layer where most horizontal water transport through ice takes place. In this core the layer is approximately 6 cm thick. Taken from Eicken *et al.* (2002).

The structure of sea ice is such that the upper surface and several centimetres below the sea ice surface is often a highly porous, crusty layer of sea ice, as shown in the figure 3.3, Eicken *et al.* (2002). We assume that most horizontal water transport will take place in this porous crust. The solid fraction in the sea ice crust is much lower that in the ice below and therefore the permeability will be greater here than at any other depth in the sea ice. The permeability at the base of the ice in the summer melt season is small enough to make horizontal water flux greater than vertical water flux. Therefore in the model described in this thesis horizontal water flux is calculated before vertical water flux.

To take into account the effect of an impermeable layer of refrozen snow at the start of

the melt season, Eicken *et al.* (2004), vertical permeability is taken to be zero until snow in that cell has melted away entirely. Snow is assumed to have a horizontal permeability of 3×10^{-9} m^2.

3.3 Vertical Heat Transport

3.3.1 Introduction

One-dimensional thermodynamic equations are solved for every cell in the grid. The vertical heat transport model comprises a radiation model to establish the upwelling and downwelling irradiance and a thermodynamic model that determines the transfer of heat throughout the depth of the sea ice and melt pond. Melting can take place at both the surface and base of the ice depth.

3.3.2 The Radiation Model

The radiation model used here is a scaled down version of the model described in Perovich (1990) and identical to the model described in Taylor & Feltham (2004). In the Perovich (1990) model transmission of incoming and outgoing radiation is measured at a number of points within a one-dimensional sea-ice depth. The amount of absorption or reflection of radiation at a point within the sea ice depends on the sea ice optical properties which can change with depth. In the reduced radiation model used here the optical properties of sea ice do not vary with depth. However the melt pond and snow cover is considered as a separate layer each with its own optical properties. The optical properties vary with time, to take into account the physical changes in sea ice that occur over the melt season. The amount of absorption and reflection of radiation depends on the optical properties of sea ice.

As described in Chapter 1 the ratio of pure ice to brine is constantly adapting to

maintain local thermodynamic equilibrium within the sea ice structure, therefore changes in temperature cause significant changes to the the physical properties of sea ice, Perovich (1996). Changes in physical properties alter the optical properties of sea ice, and hence the albedo. The optical properties of sea ice that affect the transfer of radiation at the surface and within the sea ice are those properties that affect the amount of absorption and scattering of radiation. In sea ice the physical properties that can cause the optical properties to change are brine pockets, air pockets, the ice itself, and contaminants in the ice such as sediments, biota or other organic matter. Contaminants are either brought into the pond by the wind or ocean spray, or were trapped within the brine pockets when the ice first formed. Scattering occurs mainly due to air bubbles and brine pockets. The absorption coefficient of sea ice can be calculated by combining the absorption coefficients of ice, brine pockets, air pockets and contaminants.

For simplicity, in the radiation model we use here the optical properties of sea ice are constant with depth, but vary with time.

The optical properties of sea ice are evaluated and are used in the calculation of the incoming and outgoing radiation in the sea ice, this allows the net radiation at each point and the albedo to be calculated. Spectral variation in the radiation and optical properties is ignored, as shown to be reasonable in Taylor (2003). In this model the incoming and outgoing radiation is modelled in the sea ice and melt pond. The snow layer is considered to attenuate radiation effectively at its surface and the radiation into the snow layer is not considered. In the case of a frozen over pond the radiation is modelled in three layers: the frozen lid on the pond, the pond itself, and the sea ice beneath the pond. This is shown in figure 3.4. If the surface of the pond is not frozen over the number of layers reduces to two.

The model is described as a two-stream radiation model because both incoming and

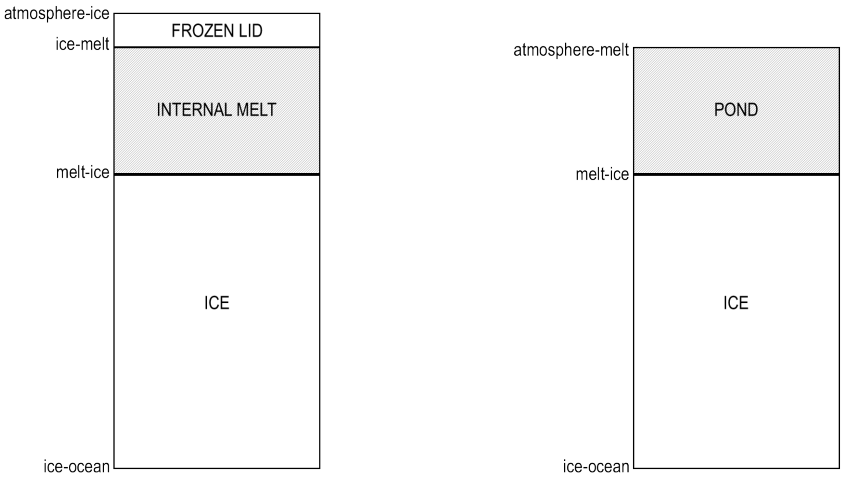

Figure 3.4: Schematic illustrating the layers in the radiation model. The maximum number of layers is three: the frozen surface of a pond, and internal melt region and the sea ice layer, this is shown in the left hand diagram. If the surface of the ice is not frozen over there could be two layers: a pond and the sea ice layer beneath.

outgoing irradiance are evaluated, the net irradiance is the difference between them. The equation governing the downwelling irradiance in each layer, $F_{\downarrow i}$, is

$$\frac{\partial F_{\downarrow i}}{\partial z_i} = -(k_i + r_i)F_{\downarrow i} + r_i F_{\uparrow i} \tag{3.7}$$

and the equation governing upwelling irradiance in each layer, $F_{\uparrow i}$, is

$$\frac{\partial F_{\uparrow i}}{\partial z_i} = (k_i + r_i)F_{\uparrow i} - r_i F_{\downarrow i}, \tag{3.8}$$

where k_i is the absorption coefficient in the layer, r_i is the scattering coefficient in the layer, z_i is the position within each layer and $i = 0, 1, 2$ is used to indicate the layer.

There is considered to be no scattering in the case of the melt pond, which is valid for ponds less than 1 m deep, Taylor (2003), in this case $r = 0$. The downwelling and upwelling irradiance then reduce respectively to

$$F_{\downarrow i} = A_i e^{-\kappa_i z_i}, \tag{3.9}$$

and

$$F_{\uparrow i} = B_i e^{-\kappa_i z_i}, \tag{3.10}$$

where A_i and B_i depend on the optical properties and thickness and $\kappa_i = k_i$ is the extinction coefficient in the layer.

When the surface is an ice surface, either solid ice or the refrozen surface of a pond, in which case there is scattering, $r \neq 0$, the general solution is

$$F_{\downarrow i} = s_i C_i e^{\kappa_i z_i} + \frac{D_i}{s_i} e^{-\kappa_i z_i}, \tag{3.11}$$

$$F_{\uparrow i} = C_i e^{\kappa_i z_i} + D_i e^{-\kappa_i z_i}, \tag{3.12}$$

where C_i and D_i depend on optical properties and depth, $\kappa_i^2 = k_i^2 + 2k_i r_i$,$s_i = \frac{(\kappa_i - k_i)}{(\kappa_i + k_i)}$ is an optical parameter that depends on the absorption and scattering coefficients in the layer.

Between the internal-melt–ice boundary and the melt-pond–ice boundary and upper-ice-surface–internal-melt boundary there is considered to be no refraction at the interface between the surfaces. At the atmosphere–ice boundary or pond surface there there is a Fresnel reflection component. Thus the boundary condition at the upper surface is

$$F_{\downarrow 0}(z_0 = 0) = (1 - R_0) F_{SW} + R_0 F_{\uparrow 0}(z_0 = 0), \tag{3.13}$$

where $R_0 = 0.05$, Taylor (2003), is the Fresnel reflection coefficient and F_{SW} is the incident shortwave radiation.

At the the lower ice surface there is again expected to be no Fresnel reflection compo-

nent, the boundary at the base of the sea ice is

$$F_{\uparrow 2}(z_2 = h_2) = 0, \tag{3.14}$$

where h_2 is the depth of the layer.

To conserve energy the irradiance fluxes are continuous across the boundaries of each layer, the boundary conditions between the internal layers are

$$F_{\downarrow i}(z_i = h_i) = F_{\downarrow i+1}(z_{i+1} = 0) \tag{3.15}$$

and

$$F_{\uparrow i}(z_i = h_i) = F_{\uparrow i+1}(z_{i+1} = 0), \tag{3.16}$$

where $i = 0, 1, 2$ are the layers.

3.3.3 Heat Transport Through Sea Ice

Sea ice is modelled as a mushy layer. A mushy layer is defined as a binary alloy in which there is an almost pure solid matrix with an interstitial, impurity-rich liquid phase. In sea ice the solid matrix is pure ice and the liquid phase is brine Wettlaufer *et al.* (1997). The mushy-layer model is equivalent to the sea-ice model used in Maykut & Untersteiner (1971) and Ebert & Curry (1993) but with an advection term to account for brine transport, Feltham *et al.* (2006). The advantage of this new model for sea ice is that the ratio of liquid brine to pure ice is explicitly modelled. As long as bulk salinity is assumed to be constant, the solid fraction is dependent only on temperature.

We can assume that because the time scale of salt diffusion between the ice crystals (1000 s) is much smaller than the time scale of the diffusion of sensible and latent heat across the mushy layer that the mushy layer is in local thermodynamic equilibrium,

Feltham *et al.* (2006). For simplicity the solid and liquid densities are taken to be equal. It is also assumed that the temperature at the base of the ice is constant and at the freezing temperature of the ocean, -1.8 ^{o}C. The local heat balance in sea ice is governed by heat transport though advection and diffusion, latent heat released or absorbed due to phase change and absorption of solar radiation. With these assumptions, the one-dimensional local heat budget in sea ice is

$$(\rho c)_{seaice}\frac{\partial T}{\partial t} + (\rho c)_l U\frac{\partial T}{\partial z} = \frac{\partial}{\partial z}(k_{seaice}\frac{\partial T}{\partial z}) + \rho_s \mathcal{L}\frac{\partial \phi}{\partial t} - \frac{\partial}{\partial z}F_{net}(z), \tag{3.17}$$

where $(\rho c)_{seaice}$ is the volumetric specific heat capacity of the sea ice, T is the temperature within the sea ice, $(\rho c)_l = 4.185 \times 10^6$ J m^{-3} K^{-1} is the volumetric specific heat capacity of the interstitial brine, $U = u/(1-\phi)$ is interstitial Darcy velocity of brine, k_{seaice} is the thermal conductivity of the sea ice, $\rho_s \mathcal{L} = 3.0133 \times 10^8$ J m^{-3} is the latent heat of fusion of the ice, ϕ is the solid fraction and $F_{net}(z) = F_{\downarrow} - F_{\uparrow}$ is the total radiant heat energy at a depth z.

The thermal conductivity and volumetric specific heat capacity of the sea ice are defined as functions of the solid fraction. Volumetric heat capacity is defined as

$$(\rho c)_{seaice} = (\rho c)_s \phi + (\rho c)_l (1-\phi), \tag{3.18}$$

$(\rho c)_s = 4.185 \times 10^6$ J m^{-3} K^{-1} is the volumetric heat capacity of the ice. Volumetric thermal conductivity of sea ice is defined as

$$k_{seaice} = k_s \phi + k_l (1-\phi), \tag{3.19}$$

where $k_s = 2$ W m^{-1} K^{-1} is the thermal conductivity of the ice and $k_l = 0.5$ W m^{-1} K^{-1} is the thermal conductivity of the brine.

Sea ice is assumed to be in local thermodynamic equilibrium, therefore salt concentration and temperature are related by the liquidus curve, this is illustrated in section 1.2. In the region of the freezing temperature of water the liquidus curve is linear, this linear relationship is assumed to be valid at all temperatures following Taylor (2003). Temperature and salt concentration are therefore related by

$$T = T_L(C) = -\Gamma C + T_L(0), \tag{3.20}$$

where $T_L(C)$ is the equilibrium freezing temperature for a concentration of the solute C, $T_L(0)$ is the equilibrium freezing temperature at zero concentration and $\Gamma - 0.0524$ K / psu assuming that seawater can be modelled as a sodium-chloride–water solution with a concentration of 35 psu, thus $T_L(C)$=271.2 K and $T_L(0)$=273 K.

The bulk salinity of sea ice, which is the concentration of salt per unit volume of sea ice, is defined by

$$C_{bulk} = \phi C_s + (1 - \phi)C, \tag{3.21}$$

where C_s, the salt concentration in the solid ice is taken to be 0 psu following Taylor (2003) and Weeks & Ackley (1986).

Whilst the bulk salinity of ice depends on its history, Untersteiner (1968) most models treat bulk salinity as constant, for example Ebert & Curry (1993) which is a reasonable assumption for most sea ice, Weeks & Ackley (1986). Assuming that the local bulk salinity is constant allows the solid volume fraction of the sea ice to be written as a function of temperature using equations 3.20 and 3.21.

Using the new expression for the solid volume fraction, the solid volume fraction in

the mushy layer equation can be replaced to give

$$(\rho c)_{seaice}\frac{\partial T}{\partial t} + (\rho c)_l U\frac{\partial T}{\partial z} = \frac{\partial}{\partial}(k_{seaice}\frac{\partial T}{\partial z}) + \rho_s \mathcal{L}\frac{T_s - T_{bulk}}{(T_S - T)^2}\frac{\partial T}{\partial t} - \frac{\partial}{\partial z}F_{net}(z), \qquad (3.22)$$

where

$$(\rho c)_m = ((\rho c)_s - (\rho c)_l)\frac{T_{bulk} - T}{T_s - T} + (\rho c)_l \qquad (3.23)$$

and

$$k_m = (k_s - k_l)\frac{T_{bulk} - T}{T_s - T} + k_l, \qquad (3.24)$$

where $T_s = T_L(C_s)$=273 K, the equilibrium freezing temperature of pure water. $T_{bulk} = T_L(C_{bulk})$=272.69 K the equilibrium freezing temperature of brine with the bulk salinity.

3.3.4 Heat Transport within Snow

Following Maykut & Untersteiner (1971) and Taylor & Feltham (2004) heat transport through snow is modelled by the heat diffusion equation,

$$\rho_{snow} c_{snow}\frac{\partial T}{\partial t} = k_{snow}\frac{\partial^2 T}{\partial z^2}, \qquad (3.25)$$

where the density of snow before melting is ρ_{snow}, c_{snow} is the volumetric specific heat capacity of snow and k_{snow} is the thermal conductivity of snow. Dry snow density is 330 kg m^{-3}, this value increases as snow melts and becomes saturated with snow. The heat capacity of snow is 2092 J kg^{-1}K^{-1} and the thermal conductivity of snow is 0.31 W m^{-1}K^{-1}.

In the same manner as Taylor & Feltham (2004) it is assumed that snow is very effective at scattering radiation at its surface and therefore radiation within the snow cover is neglected.

3.3.5 Heat Transport in Melt Ponds and Internal Melt Regions

Melt ponds are assumed to be have a salinity of 3.9 psu following Taylor (2003), due to a small volume of brine mixing with the snow melt as the sea-ice surface melts, and are assumed to have the same salinity throughout due to turbulent mixing. The low surface-air temperature causes the pond surface temperature to be below the temperature at which the density of brine is at its maximum, which for this assumed salinity is approximately 276 K. Since the water at the surface of the pond, which has a higher temperature due to radiation absorbed at the surface, will have a higher density than the cooler water at the base of the pond, a convective motion is set up where the dense warm water falls and the less dense, cool water rises. The convective mixing in the pond will continue as long as the surface is warmed by the sun. It is assumed that the pond is well mixed in the central region and the evolution of core temperature is sought. In the Taylor & Feltham (2004) model convection within the pond can either be laminar or turbulent. The critical Rayleigh number decides whether the pond will have turbulent convection or not. Since the Rayleigh number exceeds the critical Rayleigh number for ponds of even 1 cm in depth sufficiently it is assumed that convection within the pond will always be fully turbulent and heat transfer modelled using the four-thirds rule, Taylor (2003). In this case energy transfer within the central region of the pond is governed by

$$(\rho c)_{pond} h_{pond} \frac{\partial T}{\partial t} = -F(T_{lower}) - F(T_{upper}) - F_{net}(h_{upper}) - F_{net}(h_{lower}), \qquad (3.26)$$

where $(\rho c)_{pond}$ is the volumetric specific heat capacity of the pond, h_{pond} is the depth of the pond, T is the core temperature of the pond, T_{lower} is the temperature at the lower boundary of the pond and T_{upper} is the temperature at the upper boundary of the pond, $F_{net}(h_{upper})$ is the net irradiance at the upper surface of the melt pond and $F_{net}(h_{upper})$ is the net irradiance at the lower surface of the melt pond.

In the boundary layer heat flux is assumed to be independent of the depth of the boundary layer. So heat at the boundary can be modelled by the four-thirds law for turbulent convection, Batchelor & Moffatt (2000). The heat flux, F_C, out of the liquid layer at the upper boundary is given by

$$F_C(T) = \mathrm{Sgn}(T - T_{boundary})J|T - T_{boundary}|^{4/3} \tag{3.27}$$

where T is the core temperature of the pond, $T_{boundary}$ is the temperature at the boundary and

$$J = \gamma(\frac{g\alpha^* k_{pond}^2}{\nu})^{1/3}, \tag{3.28}$$

where ν is the kinematic viscosity of the pond, k_{pond} is its thermal diffusivity and α^* is the coefficient of thermal expansion and $\gamma = 0.1$ is a constant of proportionality.

3.3.6 Boundary Conditions

Net Energy at the Upper-Surface–Atmosphere Interface

At the interface between the atmosphere and the uppermost layer the net energy flux must be balanced. The uppermost layer can be snow, melt pond or bare sea ice. There are separate surface energy balances for each surface type. Sensible heat flux, F_{sens}, and latent heat flux, F_{lat} are defined respectively by

$$F_{sens} = \rho_{air} c_{air} C_T v_{wind}(T_{air} - T_0) \tag{3.29}$$

and

$$F_{lat} = \rho_{air} \mathcal{L} C_T v_{wind}(q_{air} - q_0), \tag{3.30}$$

for each layer, where $\rho_{air} = 1.275$ kg m^{-3} is the density of dry air, $c_{air} = 1005$ J kg^{-1} K^{-1} is the specific heat capacity of dry air, T_{air} is the surface air temperature (measured at a reference level 10 m above the surface), v_{wind} is wind speed (measured at a reference level 10 m above the surface), $\mathcal{L} = 2.501 \times 10^6$ J kg^{-1} is the the latent heat of vaporisation, q_0 is the specific humidity at the surface, q_{air} is the specific humidity (measured at a reference level 10 m above the surface), T_0 is the surface temperature and C_T is the stability dependent bulk transfer coefficient which takes a different value for each surface type. The value of C_T for melt ponds is taken to be the same as leads following Taylor & Feltham (2004), this simplification was made due to lack of relevant measurements for leads although the error implied by this approximation is unlikely to be significant since the sensible and latent heat fluxes are smaller than the radiative fluxes. The daily values for moisture and atmospheric temperature are approximated from a cubic spline interpolation of the monthly mean values in the same manner as Ebert & Curry (1993). The wind speed is taken from SHEBA data.

The net energy flux at the upper surface for the case of a melt pond is

$$E_{pond} = F_C(T_o) + F_{LW} - \epsilon\sigma {T_o}^4 + (1 - i_o)(1 - \alpha)F_{SW} - F_{sens} - F_{lat}, \tag{3.31}$$

where the incoming shortwave radiation, F_{SW}, and longwave radiation, F_{LW}, are calculated in the radiation model (described in the previous section) and $F_C(T_0)$ is the heat flux at the upper surface of the pond, i_o is the fraction of incoming radiation that penetrates the material and therefore does not act at the surface (for the melt pond the value $i_o = 0.6$), α is the surface albedo, $\epsilon = 0.97$ is the emissivity of the pond, $\sigma = 5.67 \times 10^{-8}$ is the Stefan-Boltzmann constant, and T_0 is the temperature at the surface of the pond.

For a bare ice layer the net energy flux at the upper boundary is given by

$$E_{seaice} = k\frac{\partial T}{\partial z} + F_{LW} - \epsilon\sigma {T_0}^4 + (1 - i_o)(1 - \alpha)F_{SW} - F_{sens} - F_{lat}, \tag{3.32}$$

here i_o is required to be either $\frac{i_o}{i_1}$, where i_1 is the net irradiance at the first internal grid point, or 0.4, whichever is smaller Taylor & Feltham (2004). This is to force melting to begin at the surface and not internally.

For snow the net surface energy flux is given by

$$E_{snow} = k\frac{\partial T}{\partial z} + F_{LW} - \epsilon\sigma {T_o}^4 + (1 - \alpha)F_{SW} - F_{sens} - F_{lat}, \tag{3.33}$$

here there is no i_o since no radiation is assumed to transmitted into the ice.

Melting Conditions

Bare ice before pond has formed

Before melting begins the energy flux balance at the ice surface must be

$$E_{seaice} = 0. \tag{3.34}$$

Once the ice surface melting temperature is reached, for simplicity the ice surface melting temperature is held constant at -0.2^{o}C as the surface is relatively fresh due to melting snow cover, the energy flux at the surface must be equal to the latent heat energy needed to melt the sea ice:

$$E_{seaice} = \rho_s \mathcal{L}\phi\frac{dh_s}{dt}, \tag{3.35}$$

where h_s is the sea-ice depth.

Pond

As soon as a pond develops on the surface (after one timestep) the boundary conditions change. The energy balance at the pond–atmosphere boundary when ice is melting is

$$E_{pond} = 0, \tag{3.36}$$

and the velocity of the upper ice surface, h_p is

$$\rho \mathcal{L} \phi \frac{dh_p}{dt} = k_m \frac{\partial T}{\partial z} + F_C((T_L(C_{pond}))), \tag{3.37}$$

where $T_L(C_{pond})$ is the equilibrium freezing temperature at concentration C_{pond} and F_C is the heat flux out of the pond. This is a moving boundary problem as ice melts at the surface (ice never grows from the upper surface) and the Stefan condition is needed to establish the velocity with which the ice surface changes. In order to use the Stefan condition to explicitly define the the evolving position of the surface it must be assumed that the solid fraction at the surface of the ice is greater than zero, Taylor & Feltham (2004).

Refrozen Pond

When the melt pond refreezes the internal melt region is assumed to have the same bulk salinity properties as the sea ice. The refrozen surface is again at the melting temperature of sea ice. In this case the speed at the boundary of the refrozen surface and the internal melt region is

$$\rho \mathcal{L} \phi \frac{dh_p}{dt} = k_m \frac{\partial T}{\partial z} - F_c((T_L(C_{pond}))). \tag{3.38}$$

Ice Base

At the sea-ice–ocean boundary it is assumed that the sea ice is at the freezing temperature of the ocean (assumed to be constant). Here the velocity of the boundary determined

with the Stefan condition is given as

$$\rho_s \mathcal{L} \phi \frac{dh_i}{dt} = k_{seaice} \frac{\partial T}{\partial z} - F_{ocean}, \tag{3.39}$$

where F_{ocean} is the heat flux from the ocean into the sea ice.

Snow

In the case before snow melting has started at the snow upper surface

$$E_{snow} = 0. \tag{3.40}$$

When the snow surface reaches its melting temperature, 0 ^{o}C heat flux and temperature are assumed to be continuous across the snow–ice boundary, that is

$$k_{snow} \frac{\partial T}{\partial z} = k_{ice} \frac{\partial T}{\partial z}. \tag{3.41}$$

The temperature profile within the snow is never calculated in this model, only the surface temperature is evaluated, so to calculate the initial depth of snow melt a linear temperature profile is assumed and the change in snow thickness is calculated, the snow thickness, h, at a time t, as melting starts is determined by

$$h(t) = h(t - \delta t) - \frac{c_{snow} h(t - \delta t)(T_0 - T_{ice})}{2\mathcal{L}_{snow}}, \tag{3.42}$$

where δt is the length of a timestep, c_{snow} is the specific heat capacity of snow, $\mathcal{L}_{snow}$ is the latent heat of snow, T_0 is the surface temperature of the snow and T_{ice} is the temperature at the snow ice interface before melting has taken place. After this initial melting has taken place the snow layer becomes isothermal and now the requirement at the upper snow surface is that the net energy at the surface needs to balance the latent heat needed

to melt the snow:

$$E_{snow} = \rho_{snow}\mathcal{L}_{snow}\frac{dh_{snow}}{dt}. \tag{3.43}$$

The melted snow layer is used to form the initial pond depth. This requires the melted snow to be included in the snow layer, causing densification. The changing density of snow is calculated by a quadratic equation which allows mass to be conserved, Taylor & Feltham (2004). In addition to this the water content in snow is allowed to pass between cells as part of the horizontal water transport. For simplicity the water transported into adjacent cells is recorded but does not affect the density of the snow. The depth of water is added to the initial water depth once the initial melt pond forms.

3.4 Method of Solution for the Thermodynamic Model

The governing equations to be solved in each layer (pond, snow and ice) contain moving boundaries. The equations and boundary conditions are nondimensionalised, using a lengthscale L, a timescale $\tau = L^2/\kappa_l$ and a flux scale F, and transformed to a new co-ordinate system where the domain is fixed, as shown in Taylor (2003). The transformation takes the (z, t) co-ordinate system to the (z', t') co-ordinate system,

$$z' = \frac{z - h_a}{h_b - h_a},\ t' = t, \tag{3.44}$$

where $h_a < h_b$ are the positions of the boundaries in the layer. The solution procedure treats the boundaries (h_a, h_b) as fixed, solves the heat transport equations with fixed temperatures at the boundaries for one timestep, and then uses the Stefan conditions to update boundary locations and determine the amount of freezing or melting. The heat transport equations in the (z', t') co-ordinate system are first-order parabolic differential equations which can be solved using the D03PCF routine from the Numerical Algorithms

Group Library. The routine uses standard finite difference methods and the method of lines.

3.5 Summary

In this chapter the combined cellular automaton and thermodynamic model were introduced. The cellular automaton splits an arbitrary section of a sea ice floe into rectangular prisms, called cells, with sides 5 m in length and with depths defined by the topography model explained in chapter 4. In each cell heat transport equations are solved to determine the volume of melt. Darcy's Law is used to evaluate the volume of water transport out of a cell in both the vertical and horizontal directions. Water transport in the horizontal direction puts cells in communication with each other. Sea level with respect to the entire ice floe, that is the whole grid of cells, is calculated at each timestep and is used in the calculation of hydraulic head of water in each cell.

Heat transport within the sea ice is governed by the mushy-layer equations, these treat sea ice as a binary alloy of pure ice and brine. The mushy-layer equations are solved in the vertical direction only, in each cell. Heat transport within the snow is determined by a heat diffusion equation and heat transport within the pond is established using the assumption of turbulent convection within the pond. The irradiance source term in the heat transport equations is established through the radiation model, forced with SHEBA data, Taylor (2003). The radiation model calculates irradiance within the melt ponds and sea ice.

The cellular automaton water and heat transport model described here is initialised with ice and snow topography data which is outlined in the chapter 4. In chapters 5 and 6, I show the results of models runs of the melt-pond-sea-ice model described here where initial ice and snow topographies and ice permeability are varied. In chapter 7, I compare

results from the model described here with previous sea-ice–melt-pond models and with observational data.

Chapter 4

Stochastic Ice and Snow Thickness Topography Generation and SHEBA Forcing Data

This chapter outlines the method used to create ice and snow topographies that are used as initial conditions for the melt-pond–sea-ice model described in chapter 3. Statistical data was taken from the available observational data and was used to simulate an ice and snow surface on the correct scale to be used as initial input data to the cellular automaton model. The method allows an unlimited number of surface topographies to be created and was used here to create a number of topographies representing rough and smooth first-year and multi-year ice and rough, smooth, thick and thick snow covers. This chapter comprises a brief outline below of the importance of snow and ice topography to the evolution of melt ponds why it was necessary to create an initial ice and snow topography model, following this I describe the mathematics that underlies the stochastic topography model and explain how the available ice and snow thickness data was used to create snow and ice topographies.

Field data, Perovich *et al.* (1999), Fetterer & Untersteiner (1998) and Eicken *et al.* (2004), suggest that initial melt-pond surface shape and size is governed by sea-ice topography, with ponds forming in depressions on the sea-ice surface. The influence of sea-ice topography persists throughout the melt season since the melt rate beneath ponds is greater than the melt rate of bare ice so that ponds deepen and widen and remain at the lowest points on the sea ice surface. On multi-year ice melt ponds are thought to form in depressions formed by melt ponds the previous year. Sea-ice topography also governs the water transport through its influence on melt pond hydraulic head. It has also been suggested that snow topography can influence pond coverage and pond depth, Eicken *et al.* (2004) and Taylor & Feltham (2004). At present there is no data available that can be used directly as ice and snow surface topography input data to the model described in the previous chapter. Instead, ice topography is represented by a statistical model calibrated using the mean and variance of ice thicknesses from the SHEBA field study.

The simulation technique belongs to the field of geostatistics. Geostatistics is a group of statistical methods that have been developed to take into account the physical spatial relationship between measurements that exists when modelling natural phenomena. Classical statistical techniques have been adapted so that spatial distribution can be predicted or simulated, Isaaks & Srivastava (1989). Here a random-field model is used to make an unconditional simulation of ice and snow topography. An unconditional simulation is a simulation where a surface is created without any points on the surface being predefined. The method requires some knowledge of the physical surface, in particular how measurements separated by a particular distance vary with each other. This can be used to select a theoretical mathematical model for the relationship between measurements at all locations, which is then used to generate random field simulations.

In this section the relevant mathematics are introduced followed by an explanation

of how the theoretical models are used to generate random field simulations. First a random field is defined, then the models that can be used to characterise a random field are introduced, an explanation of how the models are used to generate realisations of the random field is given and finally the available data and assumptions are discussed.

4.1 The Random Field and the Semivariogram

A random function is a function which is described by a probability model. A random field is a random-function model where the underlying probability model describes the behaviour of the variable being modelled over physical distances. A random field can be described by a covariance model and its mean or by its semivariogram (defined in section 4.2). Any random function provides a number of possible outcomes for every situation, a realisation of a random field is the set of values generated in a particular case. For example, we want to model ice-surface topography so we can generate hundreds of possible ice surfaces that have the same statistical properties as the real ice surface and are therefore representations of the ice surface. For convenience here we assume that the ice and snow surfaces are isotropic: this means that they look the same when measured in any direction; and stationary, this means a random field looks similar in different parts of the domain. These assumptions allow the surface to be described entirely by its mean and covariance. Structures such as ridges, however, cannot be modelled under these assumptions.

4.2 Covariance Model and Semivariogram

A measure of the conditional variation of two variables around their means is the covariance. Covariance is defined as

$$\sigma_{ij} = \frac{1}{n}\sum_{\alpha=1}^{n}(z_i(\alpha) - j_i)\cdot(z_j(\alpha) - j_j), \tag{4.1}$$

where j_i and j_j are the arithmetic means of the variables $z_i(\alpha)$ and $z_j(\alpha)$ and n is the number of measurements made.

With spatial data we often need to look at the relationship between values separated by a particular distance, the separation distance h is called the lag. The covariance can be extended so that the relationship between measurements at all lags can be described by a single model. This is called the covariance function and is defined by

$$C(h) = \frac{1}{N(h)} \sum_{\alpha=1}^{N(h)} z(u_\alpha) \cdot z(u_\alpha + h) - m_{-h} \cdot m_{+h}, \tag{4.2}$$

where

$$m_{-h} = \frac{1}{N(h)} \sum_{\alpha=1}^{N(h)} z(u_\alpha), \tag{4.3}$$

and

$$m_{+h} = \frac{1}{N(h)} \sum_{\alpha=1}^{N(h)} z(u_\alpha + h), \tag{4.4}$$

are the lag means, $N(h)$ is the number of pairs of data that are measured at that lag and in that direction. Typically, and in the case of snow and ice topographies, similarity between measurements decreases as h increases, so that

$$C(h) \to 0 \text{ as } \ h \to \infty. \tag{4.5}$$

Another convenient, related method to describe spatial distribution is the semivariogram. The semivariogram is a measure of *dissimilarity* between measurements separated by a vector $\mathbf{h}$ where $\mathbf{h} = \mathbf{h}(h, \theta)$. The experimental semivariogram is defined as

$$\gamma(\mathbf{h}) = \frac{1}{2N(\mathbf{h})} \sum_{\alpha=1}^{N(\mathbf{h})} [z(u_\alpha) - z(u_\alpha + \mathbf{h})]^2. \tag{4.6}$$

The semivariogram increases as $\mathbf{h}$ increases.

Here we assume that the region we want to recreate is stationary so that the covariance function and semivariogram look the same in every direction, and $\mathbf{h}$ is a measure of distance only, therefore $\mathbf{h} = h$. The covariance function and semivariogram, $\gamma(h)$, of a random field are related by

$$\gamma(h) = C(0) - C(h). \tag{4.7}$$

If we suppose that

$$C(h) \to 0, \text{ as } h \to \infty, \tag{4.8}$$

then

$$\gamma(h) \to C(0), \text{ as } h \to \infty. \tag{4.9}$$

The latter limit is known as the sill value of the semivariogram and is a useful parameter, $C(0)$ is the covariance of a variable with itself, i.e. the variance.

4.3 The Sill, Range and Nugget Effect

The sill is the limiting value of a semivariogram, and the range is the lag at which the sill is reached, this is shown in figure 4.1. The range can be interpreted as the lag distance beyond which there is no longer any correlation between measurements.

The small scale structure of a random field is described by the behaviour of the covariance model or semivariogram near the origin. There are four typical behaviour types, these are parabolic, linear, nugget effect and pure nugget. Parabolic behaviour at the origin indicates a strong correlation between values that are separated by small distances and implies a smooth regular surface. Linear behaviour suggests a surface that is less regular than one that has parabolic behaviour but there is still a strong correlation so the surface represented is reasonably smooth. The nugget effect describes a discontinuity at the origin and describes a surface that is very irregular over small distances. The pure nugget effect

describes a surface where there is no correlation whatsoever over short distances. This surface has no structure at all and is entirely random, Chiles & Delfiner (1999).

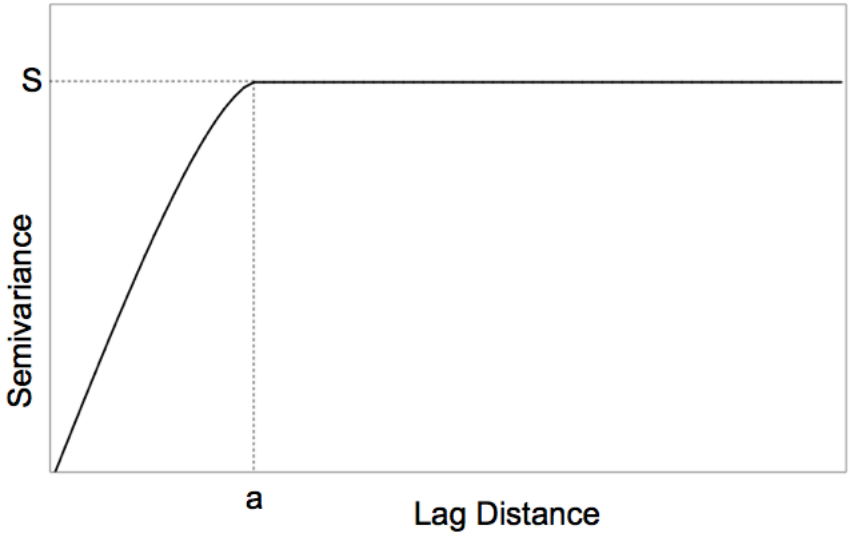

Figure 4.1: The spherical semivariogram. S marks the sill and a is the range.

4.4 The Theoretical Spherical Covariance Model

We now have sufficient knowledge to construct a random field. An empirical semivariogram can be plotted and a theoretical semivariogram can be fitted to this based on the behaviour of the empirical semivariogram at the origin and whether or not the empirical semivariogram is bounded.

Based on the available data described in section 4.5, sea ice and snow thickness distribution can be modelled by a spherical semivariogram, Sturm *et al.* (2002), shown in figure 4.1. The behaviour at the origin is linear and a sill is identifiable. Sea-ice and snow topographies are therefore supposed to be reasonably smooth on a short scale but with a finite range beyond which there is no correlation. The theoretical covariance model is defined by

$$C(h) = \frac{2}{\pi}\left[\arccos(\frac{h}{a}) - \frac{h}{a}\sqrt{(1-\frac{h^2}{a^2})}\right], \; h \; < \; a \tag{4.10}$$

and

$$C(h) = 0,\ h\ \geq\ a \tag{4.11}$$

when a is the range. For snow the range has been found to be 20 m and for ice it is 10 m, Sturm *et al.* (2002). The semivariogram can be plotted using the relation $\gamma(h) = C(0) - C(h)$.

4.5 Snow and Ice Thickness Data

Due to the limited availability of sea-ice topography and snow topography data, and in particular combined data it is assumed that both snow and ice topographies are isotropic and that there is no correlation between snow depth and ice thickness. Therefore two independent topographies are generated, one for the ice topography and one for the snow topography. A two week study of Arctic snow cover distribution was made by Sturm *et al.* (2002) as part of the SHEBA field study. Over this period in April and May 21169 measurements of snow depth on a variety of ice types was made. Probability density functions for the observations are shown in figure 4.2.

Mean snow depth was 33.7 cm with a standard deviation of 19.3 cm. Snow depths ranged from 0 to 1.50 m. Snow depths were measured on a range of ice types including smooth first-year ice, a combination of multi-year ice with refrozen ponds and some first-year ice, hummocky multi-year ice, and deformed ice. Sturm *et al.* (2002) also found that snow cover could be modelled by a spherical semivariogram with a range of 20 m for snow of all thicknesses and on all types of ice. The experimental semivariograms are shown in figure 4.3. The sill increases as the ice roughness increases. For this study, mean snow depth and variance has been chosen based on these results for each ice type modelled.

Small-scale spatial analysis of sea ice is unfortunately much more limited, the most comprehensive data set being from the SHEBA field study. Measurements were taken at

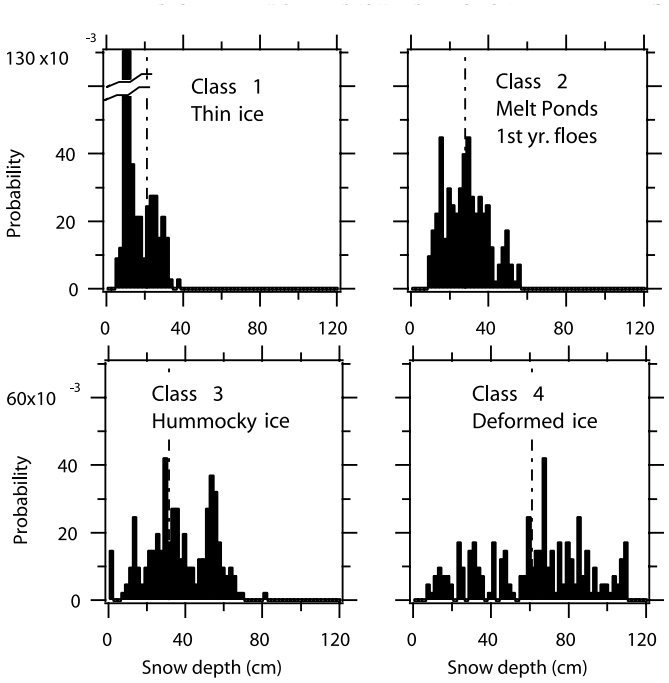

Figure 4.2: Probability distribution functions of snow thicknesses on thin ice, first-year ice with melt ponds, hummocky ice and deformed ice. The dashed line shows the mean snow depth. Snow thickness data was collected as part of the SHEBA field study. Image from Sturm *et al.* (2002).

intervals of 5 m along a series of straight lines of between 200 m and 500 m in length across the sea ice surface. Since ice thickness changes throughout the year and the model is to be initialised with ice at its maximum winter thickness before melting begins the useable data is even more limited. For this reason a probability distribution function of the ice data is not shown. However the data was used to give an estimate of possible mean ice thickness and variance in ice thickness for each ice type evaluated. The sea-ice range is taken to be 10 m following Sturm *et al.* (2002).

Table 4.1 shows the mean ice and snow thickness and ice and snow variance used to generate the standard case for multi-year and first-year ice. The fields were generated using "R Project" Random Fields package. The generated topographies are not intended to reconstruct existing topographies but to simulate a likely snow or ice topography, that can be entirely classified as first-year ice or multi-year ice and so on, something which is

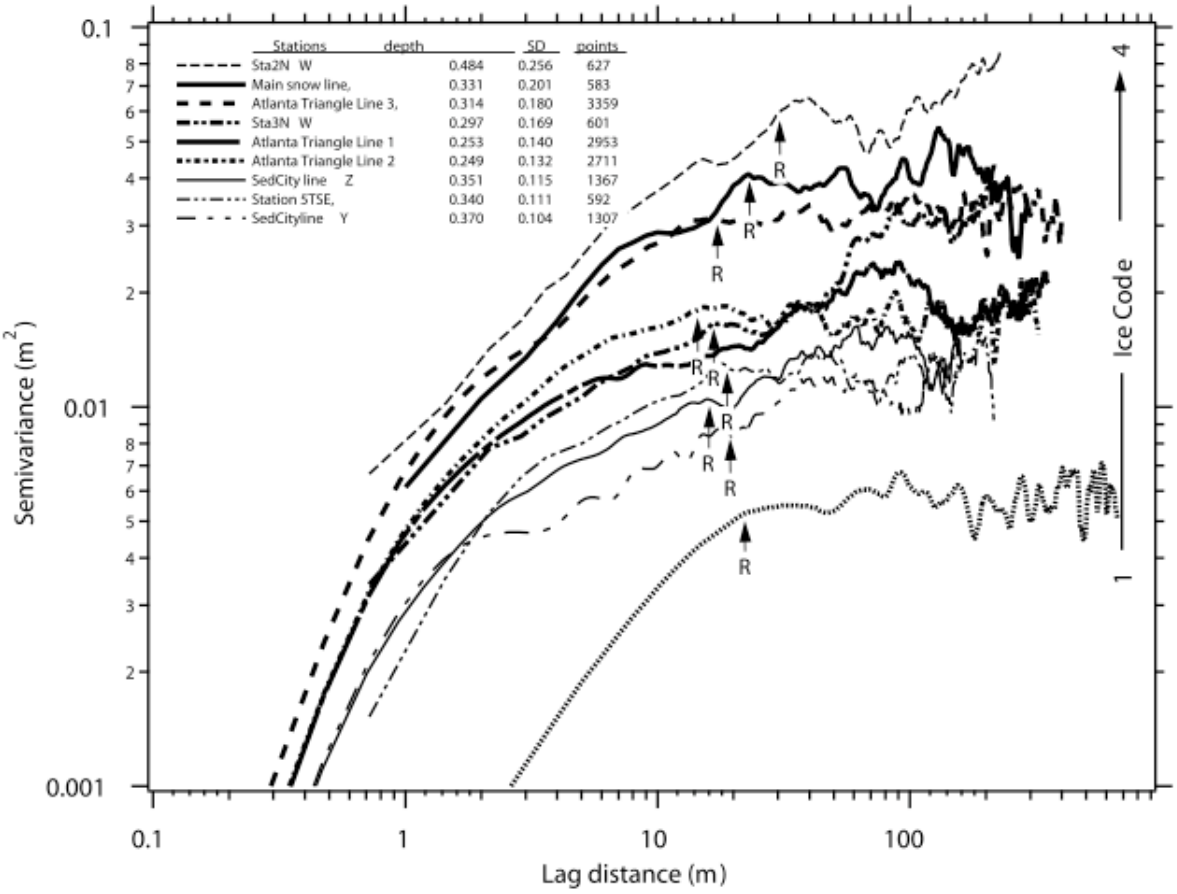

Figure 4.3: Semivariograms of snow depth on various ice types, from the SHEBA field study. R marks the semivariance range, which is approximately 20 m for snow on all ice types. The ice code on the right hand side indicates the ice type on which the snow was measured, ice code 1 is smooth ice the roughness of the ice surface increases on the scale so that ice code 4 is deformed ice. The key on the left hand side gives the location where the measurements were taken, mean snow depth, standard deviation and the number of data points. Image taken from Sturm *et al.* (2002).

uncommon in the field, as multi-year ice and first-year ice often appear together and not in isolation, Sturm *et al.* (2002). Therefore, having established that relationships between distances across the ice or snow surface could be modelled with a spherical semivariance model mean ice thickness and standard deviations were chosen to be in the range of observational data but they do not correspond exactly to data.

Ice Type	Ice Mean (m)	Ice Variance (m^2)	Snow Mean (m)	Snow Variance (m^2)
Multi Year	2.50	0.81	0.3	0.0625
First Year	1.70	0.04	0.3	0.0225

Table 4.1: Table of mean and variance of ice thickness and snow thickness(metres) for first-year and multi-year ice. These are the values used to create initial ice and snow surface topographies for the standard cases.

The ice topographies were generated as two individual topographies one representing ice thickness above sea level and one representing the ice thickness below sea level. The mean and variance values refer to the combined (ice above sea level and below sea level) topography. Probability distribution functions for ice thickness and snow depth in the first-year ice standard case and the multi-year ice standard case are shown in figures 4.4 and 4.5 respectively.

The standard cases represent level first-year ice and level multi-year ice with snow covers that would be expected in those cases. For the sensitivity studies snow covers representing thick snow, thin snow, rough snow and smooth snow on first-year ice and the same for multi-year ice were generated; rough and smooth first-year ice and multi-year ice topographies were also generated. The results of the sensitivity studies are described in chapter 5 and chapter 6.

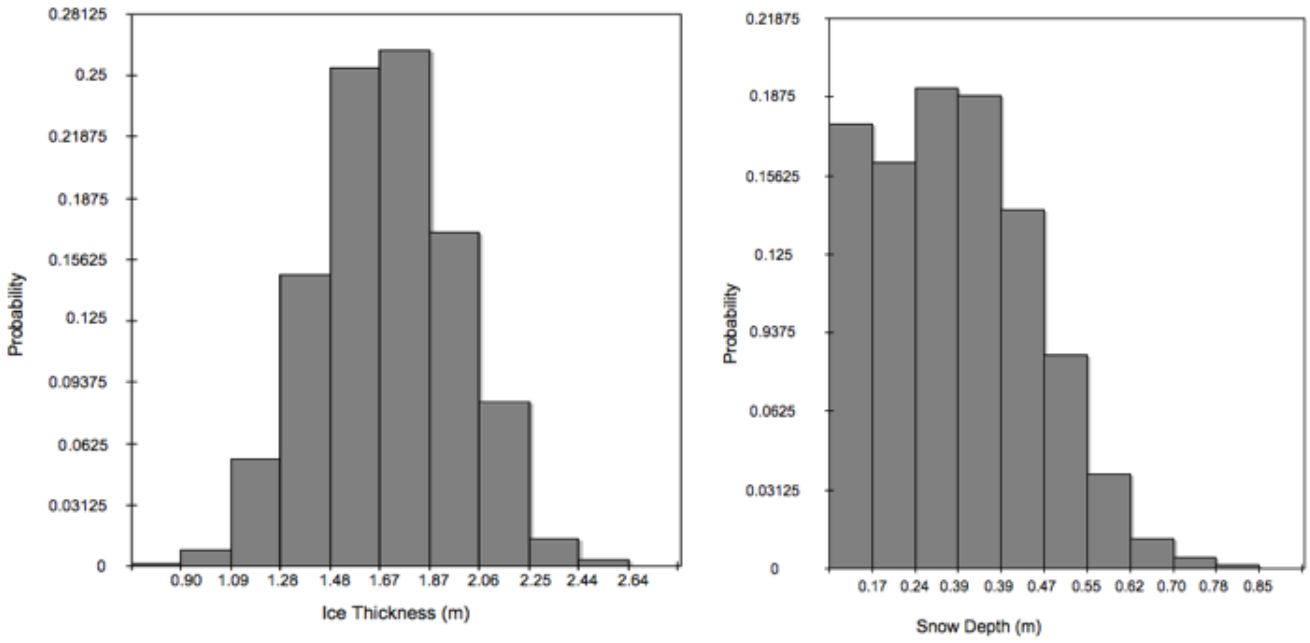

Figure 4.4: Probability distribution functions for generated first-year ice and snow topographies.

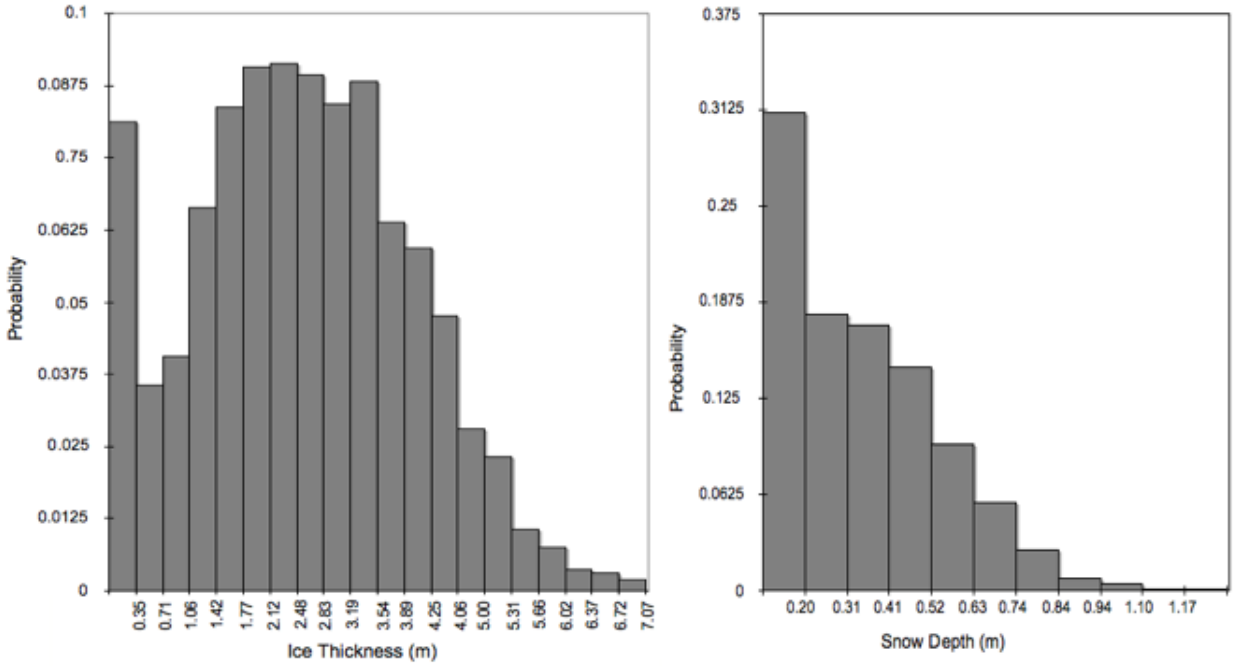

Figure 4.5: Probability distribution functions for generated multi-year ice and snow topographies.

4.6 Forcing Data

The incoming forcing parameters used in the thermodynamic component of the melt-pond–sea-ice model described in this thesis are incoming shortwave radiation, incoming longwave radiation, ocean heat flux and parameters used in the determination of sensible and latent heat flux. Parameters used to determine sensible and latent heat flux are air temperature at 10 m, wind speed at 10 m and parameters used to determine latent heat flux are air pressure and saturation specific humidity measured at 10 m.

Forcing data is identical to that of Taylor (2003), which is derived from the SHEBA Flux Group Field Study data. There is assumed to be no diurnal variation in the model forcing and the forcing data varies continually on a 365 day cycle.

For simplicity, ocean heat flux is taken to be constant 2 W m^{-2} as shown to be reasonable by Taylor (2003).

The forcing data used in the sensible and latent heat flux parameterisations, which are estimated from the SHEBA Flux Group data, are monthly averages which are linearly interpolated, except for wind speed at 10 m. The standard deviation in wind speed over the year was small, so wind speed is considered to be constant and the annual monthly average value of 4.90 m s^{-1} is used. The mid-monthly forcing values for air temperature, air pressure and saturation specific humidity are shown in table 4.2.

For incoming shortwave and longwave radiation least-squares profiles were fitted to the data and predicted values established from these. Figure 4.6 and figure 4.7 show the observed and predicted values for incoming shortwave and longwave radiation respectively.

Month	Jan	Feb	Mar	Apr	May	Jun	Jul	Aug	Sep	Oct	Nov	Dec
Air Temp (K)	243.7	242.4	250.4	256.0	263.7	272.2	273.1	271.7	269.0	260.6	252.3	241.1
Air Press (kPa)	102.9	102.1	101.7	101.5	101.8	101.7	101.6	100.5	101.5	1012	100.9	101.8
Sat. Spec. Hum	0.29	0.23	0.56	0.89	1.79	3.33	3.68	2.73		1.71	0.68	0.21

Table 4.2: Table of mid-monthly forcing data used in the melt-pond–sea-ice model.

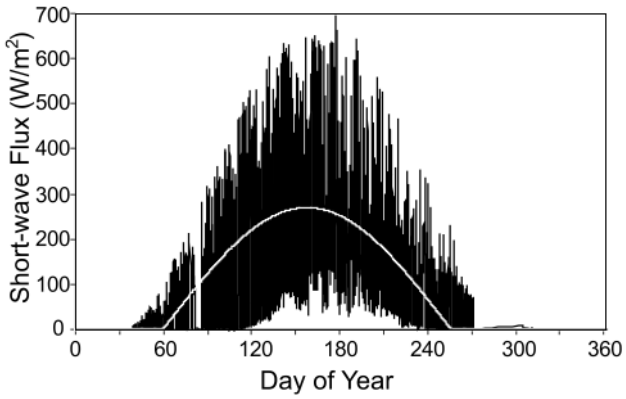

Figure 4.6: Observed (thin line) and predicted (thick line) evolution of shortwave radiation with time, using SHEBA Flux Group data. Day 0 is January 1 1997.

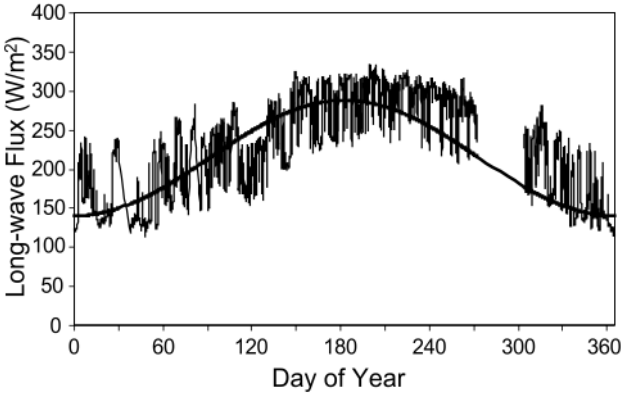

Figure 4.7: Observed (black line) and predicted (white line) evolution of longwave radiation with time, using SHEBA Flux Group data. Day 0 is January 1 1997

4.7 Summary

In this chapter I introduced the method used to create ice and snow thickness topographies, I showed how the statistical data was collated from ice and snow thickness observations and explained how this could be used to simulate an ice and snow surface. The ice and snow topographies that were generated are used to initialise the melt-pond–sea-ice model to explore the influence of snow and ice topography on pond coverage. Topographies representing conditions on first-year and multi-year ice were generated. I also detailed the forcing data used for parameterisations in the one-dimensional thermodynamic model, these were derived from the SHEBA field data.

Chapter 5

Simulations of Sea-Ice Melt Ponds on Snow-Covered First-Year Ice

In this section nine simulations of the sea-ice–melt-pond model are described. The purpose of these simulations is to examine the sensitivity of aerial pond fraction, pond depth and surface ablation to snow topography, ice topography and vertical ice permeability. The albedo of the surface is calculated in each cell as part of the thermodynamic model. The albedo of the total domain can be calculated from the individual cell values. The ice and snow topographies represent conditions found on first-year sea ice. The model is run for one melt season, from day 140 to day 230 using forcing data for incoming shortwave radiation, air temperature, specific humidity, air pressure, wind speed and ocean heat flux all derived from SHEBA data following Taylor (2003). Simulations using different realisations of the surface topographies generated from the same mean thicknesses and standard deviations in general yielded similar results, therefore a single sea-ice and snow topography realisation is chosen to represent the standard case. The similarity between two model simulations that have sea-ice topographies with the same mean ice thickness and standard deviation, but that are spatially different is shown in section 5.1. The standard

case results are described first, followed by the simulations which use the standard case ice topography and vary the snow topographies, next are cases where the standard case snow cover is used and the ice topography is altered, and, finally, cases where both the standard case snow and ice topography are used and the vertical ice permeability is varied.

In brief, the simulations showed that varying the roughness of the snow surface had a much smaller impact on pond coverage throughout the season than altering snow thickness. Decreasing snow thickness reduced pond cover and increasing snow thickness caused the ice surface to be flooded with ponds and most of the ice melted away entirely. Reducing ice roughness delayed the onset of significant pond coverage but did not affect the maximum area covered in ponds significantly. Increasing ice roughness from the standard case caused an increase in pond fraction. Increasing permeability caused pond coverage to be reduced and reducing permeability caused the surface to be flooded with ponds. The most interesting result was that increasing snow thickness caused a significant increase in the mass of ice that melted from the floe.

5.1 Standard Case

The standard first-year ice simulation uses mean ice and snow thickness values obtained from first-year ice during the SHEBA field experiment. Mean ice thickness is 1.7 m, with a standard deviation of 0.2 m. The generated snow topography has a mean thickness of 0.3 m and a standard deviation of 0.15 m, however since I impose non-zero snow cover on all the cells, to solve the problem of generated negative values of snow cover, the actual mean snow thickness is 0.31 m. The initial snow and ice thicknesses and the height of the ice surface and snow surface above sea level are shown in figure 5.1. The ice thickness topography was generated as an ice thickness below sea level and an ice thickness above sea level, hence the areas with the greatest ice thickness in the top left panel of figure 5.2 is

are not necessarily the areas with greatest ice surface height above sea level (shown in the top right panel of figure 5.2). The run was initialised with conditions for Julian Day 140 (May 20) and run for 90 days with time steps of 1 hour. In each grid cell the horizontal surface is identified as a pond, bare ice, open ocean or snow. Mean ice thickness, mean pond depth and mean snow thickness are shown in figure 5.3. Figure 5.2 shows contour plots of the pond fraction on day 175, day 180, day 190 and day 210. The relative fractions of the surface covered in ponds (solid red), snow (light blue) and open ocean (dark blue) are shown in figure 5.3. The contour plots, figure 5.2, show that the first ponds to appear are small and isolated, the ponds increase in area as more melt water becomes available and new ponds appear. By day 190 ponds are deeper and greater in area and some ponds have joined together. By day 210 ponds are much deeper but their surface area has decreased. Some of the large ponded areas have melted through entirely so that open ocean is exposed.

In the standard run (figure 5.3) the first ponds form on day 167 as the thinnest snow melts away, 7% of the surface is covered with ponds at this time. Because the snow topography contains clusters of snow with similar thicknesses in adjacent cells, the distribution of snow thickness is not even, so once the thinnest snow has bee removed snow fraction remains constant for several days until thicker snow is removed entirely from grid cells. A local maximum of 38% pond coverage is reached on day 179 which coincides with all remaining snow being removed. By day 183 the thinnest ice melts away, these cells are now classified as open ocean and water transported into these cells is considered lost to the ocean. The increase in drainage areas, due to cells melting through, occurs at the same time as an increase in melt rate, which results in a 10% increase in pond coverage, between day 185 and 187. By day 187 pond fraction reaches its maximum value of 49%. Mean pond area, shown in figure 5.7 reaches its maximum at around this time.

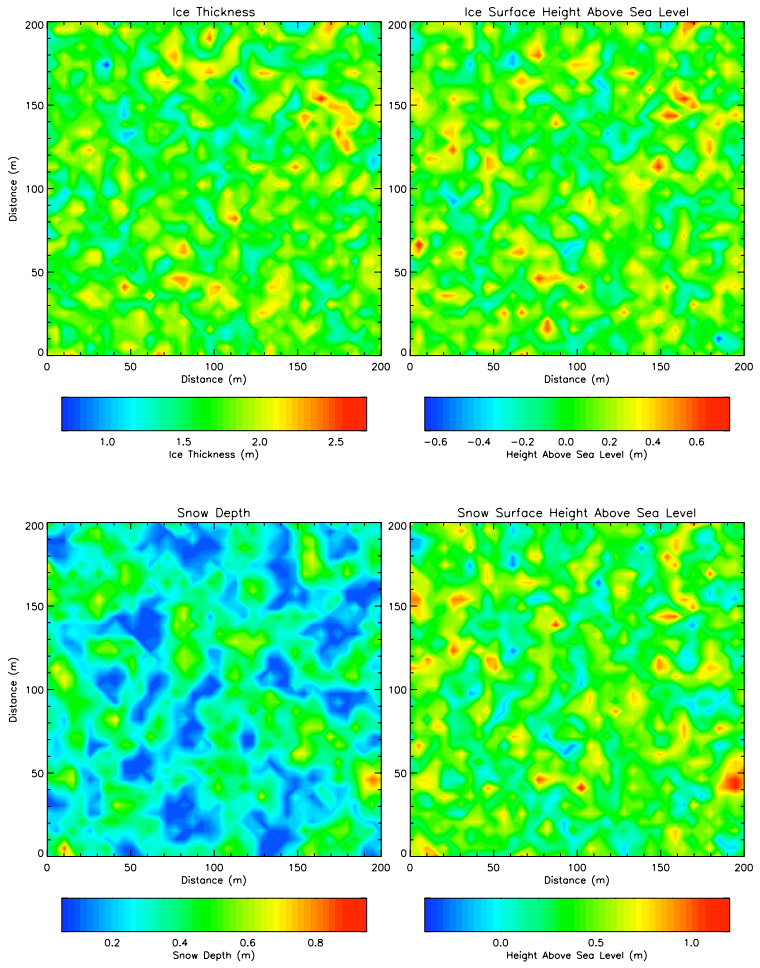

Figure 5.1: Contour plots of the initial mean ice thickness and snow depth in each cell, in the left hand column. The right hand column shows the height of the ice surface above sea level and the height of the snow surface above sea level. Surface heights above sea level can be negative.

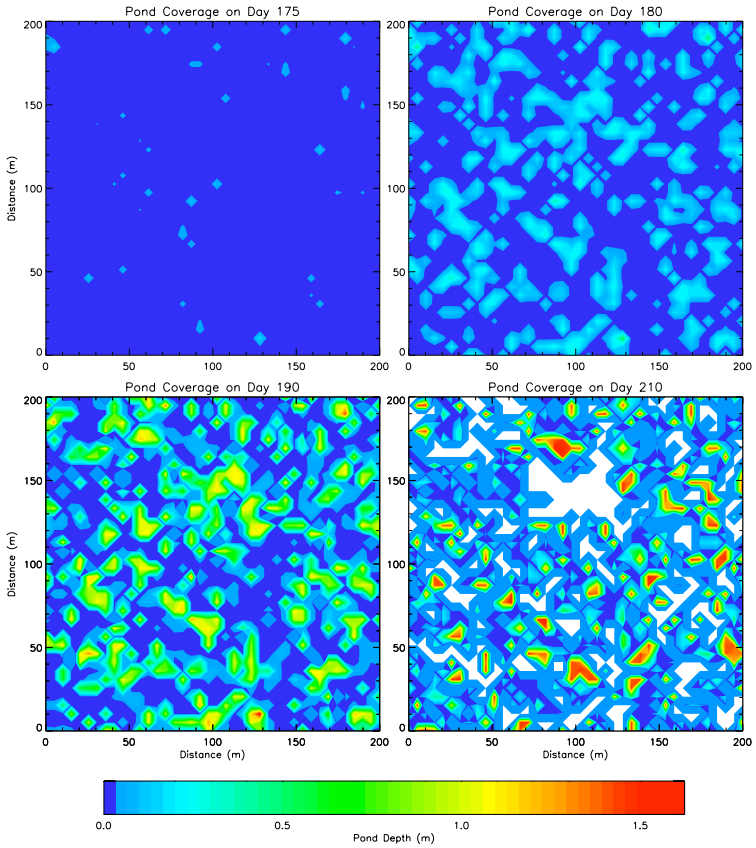

Figure 5.2: Contour plots showing simulated pond depth during the melt season. The top left panel shows pond depth on the day that ponds initially form and the bottom right panel shows pond coverage before freeze up. Dark blue represents bare ice and pond depth scale is illustrated in the colour bar with red for the deepest ponds. White regions are areas where sea ice has melted through entirely.

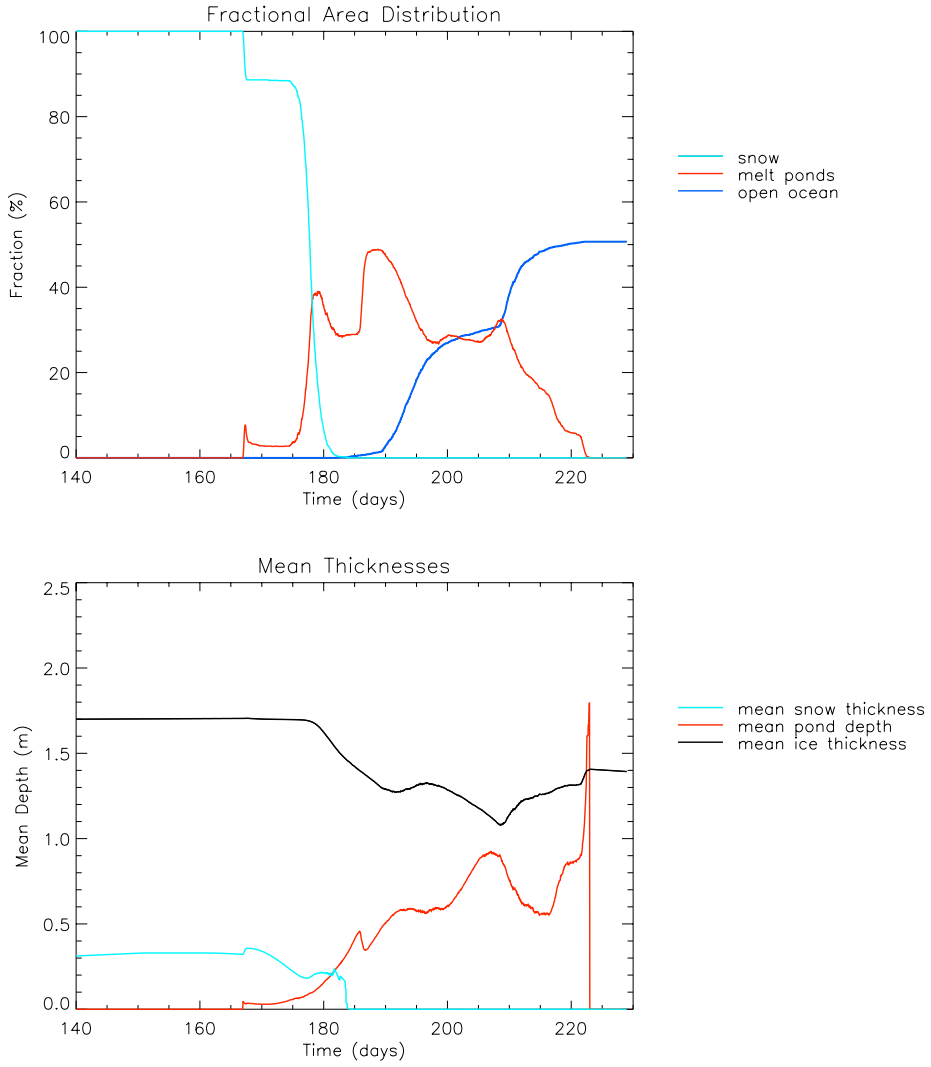

Figure 5.3: Top: Variation in the fractional distribution of surface area with time for the standard first-year ice case, where mean ice thickness is 1.7 m, standard deviation in ice thickness of 0.20 m, mean snow thickness is 0.31 m and standard deviation in snow thickness is 0.15 m. Fraction of the surface with a snow cover (light blue), fraction of the surface covered with melt ponds (red), fraction of the ice surface area covered in ponds (dashed red), fraction of the surface with no ice cover (open ocean) is dark blue. Bottom: Change in mean snow depth (light blue), mean pond depth (red) and mean ice thickness (black) with time for the standard first-year ice case.

Pond surfaces are mainly at sea level at this stage and as melt water production rate is balanced by drainage rate, mean pond depth remains almost constant at approximately 0.6 m. Pond fraction declines from day 190 onward, as ponds drain directly into the ocean and ocean fraction increases more rapidly. Pond depth, however, continues to increase due to enhanced melting beneath ponds, and water being transported horizontally across the surface to cells with the smallest ice surface height. Mean pond depth reaches a local maximum of 0.9 m on day 207 which is just before the decline in pond coverage due to surface freezing; subsequently mean ice thickness increases rapidly as pond surfaces freeze over (5.3). Thinner ponds freeze over before deeper ponds which causes an increase in mean pond depth from day 215. The maximum mean pond depth of 1.87 m occurs at the end of the season, there is only one pond remaining at this time, the deepest pond which is the last pond to freeze over. Pond fraction decreases steadily as ponds freeze over.

The percentage decrease in mass of ice and snow over the whole melt season is 62.2%; the volume of melt expressed as a depth of ice per unit area, or total ice ablation, is 1.01 m. The area averaged albedo of the entire domain (this includes open ocean cells), shown in figure 5.8 (solid line), decreases fairly steadily with time once snow has begun melting until day 205. Whilst pond fraction and ocean fraction remain constant the average albedo also remains constant, which is almost the case between day 209 and day 216 when the average albedo is at its minimum value of 0.32. The albedo increases again as ponds freeze over. By the end of the season the albedo has increased to 0.39, which is still well below the winter-time value, this is due to 50% of the surface now being open ocean.

The fractional distribution of the surface covered in snow, ponds, bare ice or open ocean is very similar for any initial ice and snow topographies with the same initial mean thickness and standard deviation. This is illustrated in figure 5.4 which shows the fractional distribution of the surface and the mean depths for the ice thickness distribution

shown in figure 5.5. The snow topography is the same snow topography as in the standard case. Due to the similarity in results between first-year ice cases with different initial ice topography realisations, a single first-year ice standard case, the standard case described above, is compared to sensitivity studies.

Figure 5.5 is a contour plot for an ice thickness topography with the same mean ice thickness and standard deviation as the standard case described above. Results from a simulation using this initial ice topography are shown in figures 5.4, these results demonstrate the similarity with the standard case described above.

5.2 Sensitivity to Snow Topography

Snow melt provides the initial volume of water to form ponds. Here snow cover mean depth and distribution are altered in order to assess the sensitivity of pond fraction and total ablation to snow cover. The four snow topographies considered represent rough snow, smooth snow, thick snow and thin snow. Each of these snow types are created from statistics of snow topographies that have been observed on first-year ice (see chapter 4).

5.2.1 Rough Snow

The rough snow topography represents the snow that would be expected on "hummocky" ice, Sturm *et al.* (2002). To assess the sensitivity to snow surface roughness the mean snow depth is the same as in the standard case, 0.3 m, although due to the imposed non-zero snow depth in every cell the actual mean snow depth in this case is 0.34 m. The standard deviation is increased from 0.15 m to 0.25 m. Fractional distribution of the surface into snow, ponds and ocean and mean snow thickness, pond depth and ice thickness are shown in figure 5.6. Changing the variability in the snow cover had very little impact on maximum pond fraction, evolution of pond fraction, pond depth or total

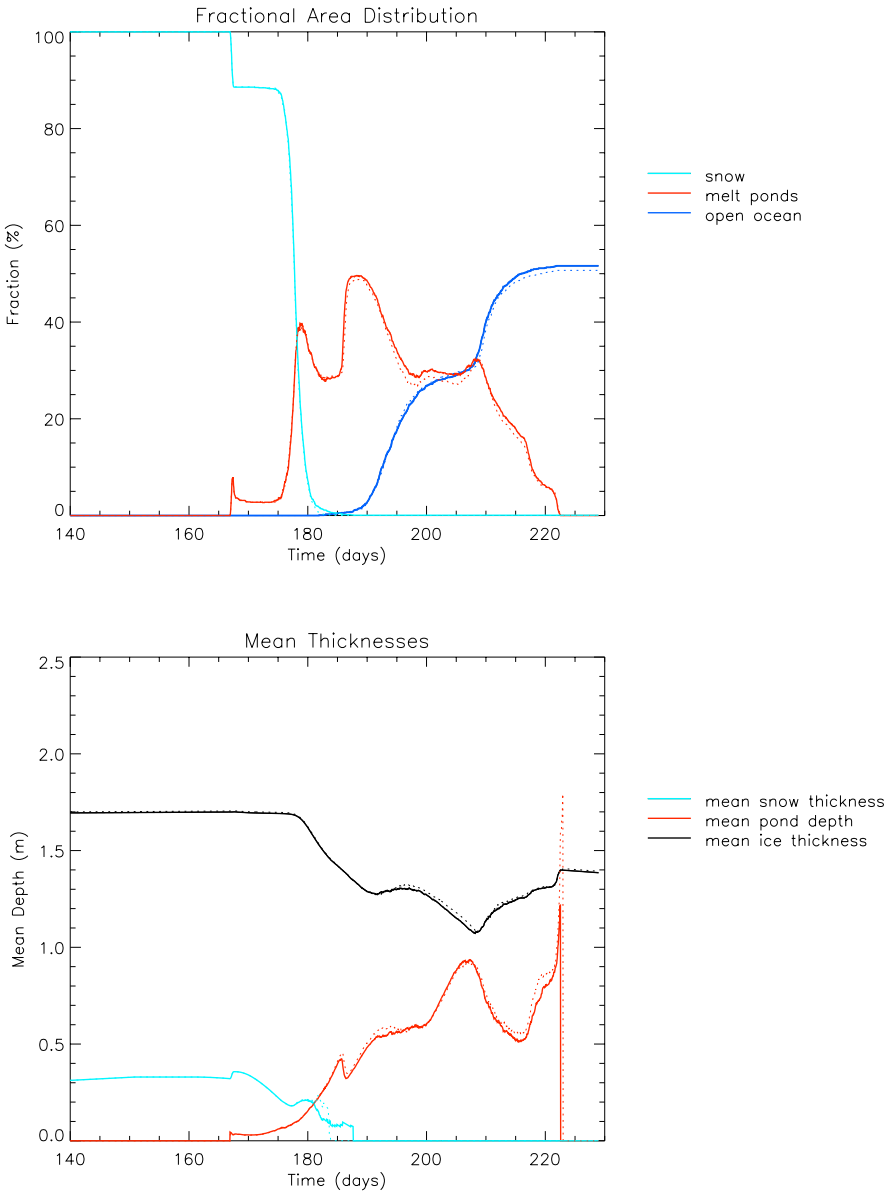

Figure 5.4: Top: Variation in the fractional distribution of surface area with time for the alternative standard first-year ice case, where mean ice thickness is 1.7 m, standard deviation in ice thickness of 0.2 m, mean snow thickness is 0.31 m and standard deviation in snow thickness is 0.15 m. Fraction of the surface with a snow cover (light blue), fraction of the surface covered with melt ponds (red), fraction of the surface with no ice cover (open ocean) is dark blue. The dashed lines represent the corresponding values for the standard first-year ice case shown in figure 5.3. Bottom: Change in mean snow depth (light blue), mean pond depth (red) and mean ice thickness (black) with time for the standard first-year ice case. The dashed lines represent the corresponding values for the standard first-year ice case shown in figure 5.3.

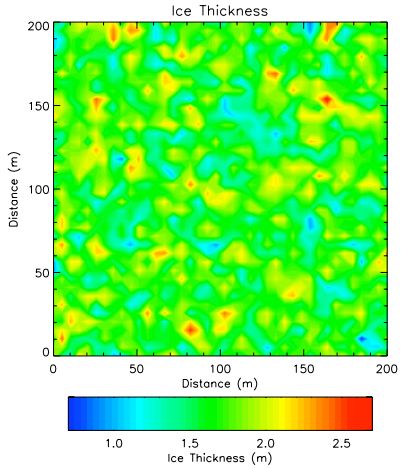

Figure 5.5: Contour plot of the initial mean ice thickness for an alternative first-year ice standard case. Mean ice thickness is 1.7 m and standard deviation is 0.20 m. Despite the spatial differences between this topography and the standard case topography shown in figure 5.1 evolution of pond depth and pond fraction is very similar to the standard case described above. The similarity in evolution in fractional area distribution and change in mean depth of ice, snow and pond is shown in figure 5.4.

ice ablation.

The increased variability in snow thickness resulted in there being more cells with a thin snow cover than in the standard case. Snow melting begins on the same date as the standard case, day 167, with 20% of cells having snow cover removed entirely on this day compared to 11.5% in the standard case. This leads to an initial pond fraction of 12.7% which is almost double the initial pond fraction of 7% in the standard case. Snow cover is completely removed from all cells on day 188, which is four days later than the standard case, this is because the maximum snow thickness is greater in the rough snow case than in the standard case. Other than this the evolution of pond coverage is very similar, the peaks in pond coverage appear at the same times and are of a similar magnitude. The maximum pond fraction is slightly larger at 53.6 % in the rough snow case compared to 48.8% in the standard case. Evolution of mean pond area, shown in figure 5.7, is similar in the rough snow case and the standard case. For most of the simulation mean pond areas in both cases is very close, however in the rough snow case mean pond area increases to a

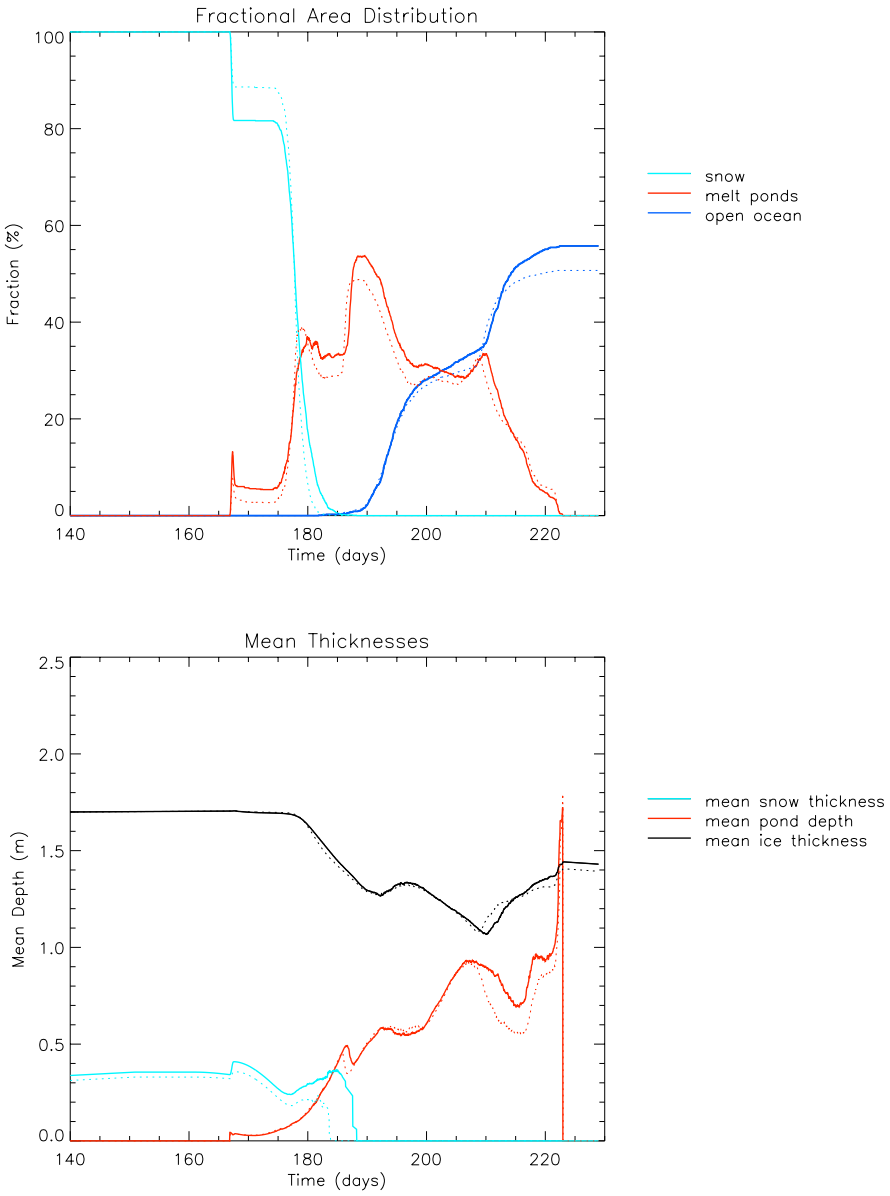

Figure 5.6: Top: Variation in the fractional distribution of surface area with time for the rough case, where mean ice thickness is 1.7 m, standard deviation in ice thickness of 0.2 m, mean snow thickness is 0.31 m and standard deviation in snow thickness is 0.15 m. Fraction of the surface with a snow cover (light blue), fraction of the surface covered with melt ponds (red), fraction of the surface with no ice cover (open ocean) is dark blue. The dashed lines represent the corresponding values for the standard first-year ice case shown in figure 5.3. Bottom: Change in mean snow depth (light blue), mean pond depth (red) and mean ice thickness (black) with time for the rough snow case. The dashed lines represent the corresponding values for the standard first-year ice case shown in figure 5.3.

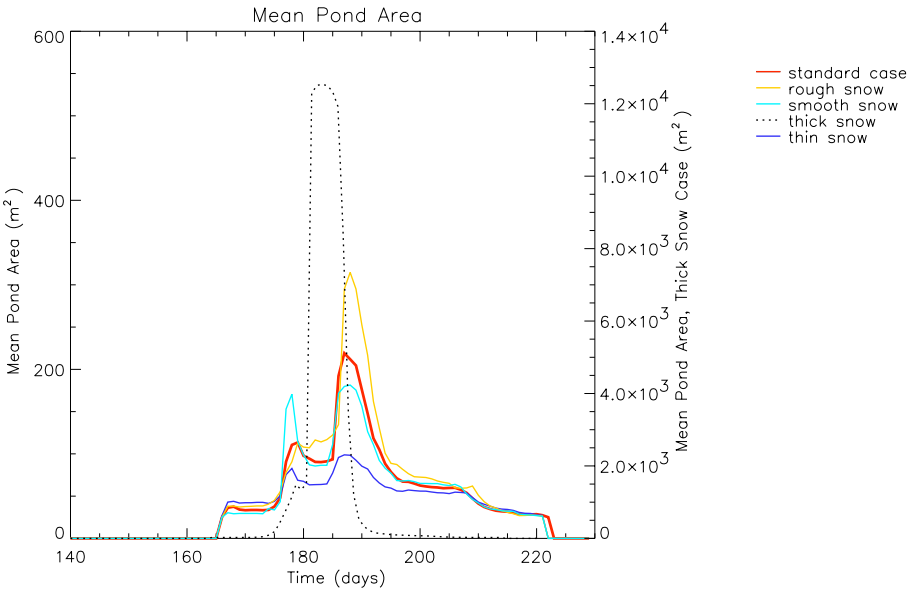

Figure 5.7: Mean individual pond area for the standard case (red) and snow sensitivity studies. Scale for the thick snow case (dotted black) in on the right hand side.

maximum of 314.7 m^2 around day 190 compared to a maximum of 219.1 m^2 at the same time in the standard case. By the end of the 90 day simulation the open ocean fraction is 55.8% which is nearly 6% more open ocean than the 50% in the standard case, with the total ablation in the rough snow case over the season being 1.07 m compared to 1.01 m in the standard case.

Despite the difference in the initial snow distribution, mean pond depth is almost identical until day 186 when the mean pond depth in the rough snow case is 13 cm deeper than in the standard case. Mean pond depth is then the same as the standard case until the maximum pond depth is reached on day 207, after this the pond depth in the rough snow case exceeds the mean pond depth in the standard case. The maximum pond depth of 1.88 m in the rough snow case is only 1 cm greater than the maximum pond depth of 1.87 m in the standard case. The maximum pond depth occurs at the same location as in the standard case, with the water driven there by ice topography.

As soon as the snow cover is removed the average surface albedo, figure 5.8, in the

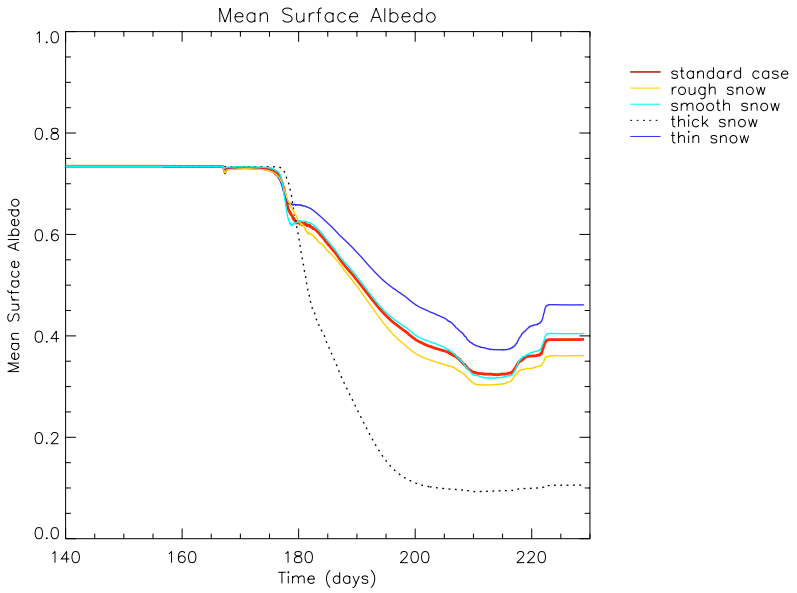

Figure 5.8: Change of aerially averaged surface albedo with time for the standard case and snow sensitivity studies.

rough snow case is consistently slightly lower than in the standard case, but evolves in the same way due to roughly the same evolution of pond coverage.

5.2.2 Smooth Snow

The smooth snow topography has the same mean thickness as the standard case, 0.3 m, but with a standard deviation of 0.1 m as compared to 0.15 m for the standard case; this standard deviation is the standard deviation in snow depth observed on thin ice by Sturm *et al.* (2002). The results, shown in figure 5.9 for the smooth snow case very closely mirror the standard case. Initial pond formation occurs on day 167, the same time as in the standard case, but snow cover is removed in all cells one day earlier in the smooth snow case than in the standard case. There are fewer cells with thin snow meaning that fewer cells are exposed when initial pond formation takes place, initial pond fraction is therefore smaller in the smooth snow case than in the standard case; only 1.6% of the surface is covered in ponds initially compared to 7% in the standard case. On day 178, as snow is

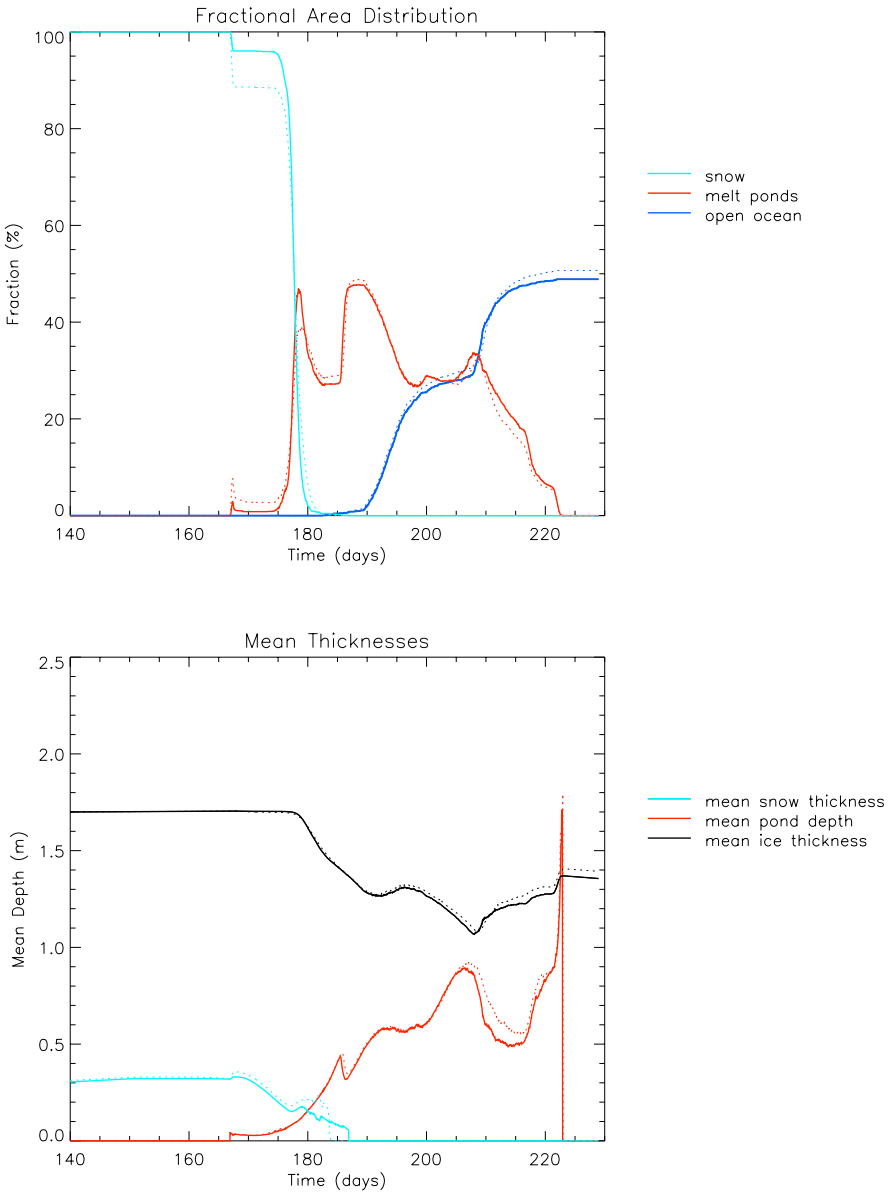

Figure 5.9: Top: Variation in the fractional distribution of surface area with time for the smooth snow case, where mean ice thickness is 1.7 m, standard deviation in ice thickness of 0.2 m, mean snow thickness is 0.31 m and standard deviation in snow thickness is 0.15 m. Fraction of the surface with a snow cover (light blue), fraction of the surface covered with melt ponds (red), fraction of the surface with no ice cover (open ocean) is dark blue. The dashed lines represent the corresponding values for the standard first-year ice case shown in figure 5.3. Bottom: Change in mean snow depth (light blue), mean pond depth (red) and mean ice thickness (black) with time for the smooth snow case. The dashed lines represent the corresponding values for the standard first-year ice case shown in figure 5.3.

removed entirely from the majority of cells, pond coverage exceeds the pond coverage in the standard case, jumping to 45.9% compared to 38.4% in the standard case. The pond fraction and ocean fraction are almost identical to the standard case for the rest of the season, with differences in the fraction of the area covered in ponds being at most 2% at any time. The final ocean fraction in the smooth snow case at the end of the season is approximately 2% less than in the standard case. There is a little more difference between mean pond area in the smooth snow case and the standard case. Mean pond area in the smooth snow case is greater than the standard case between day 175 and day 180, this is due to the surface being flooded as most of the snow melts through at roughly the same time in the smooth snow case. Maximum mean pond area occurs at the same time in both the standard case and the smooth snow case. In the standard case the maximum mean pond area is 219.1 m^2 whereas in the smooth snow case the maximum mean pond area is much lower at 181.4 m^2.

Mean pond depth is the same in the smooth snow case and the standard case until day 207 when the maximum area covered in ponds is reached. From this point onwards mean pond depth in the smooth snow case increases as mean pond depth in the standard case increases and decreases as mean pond depth in the standard case decreases but mean pond depth in the smooth snow case is smaller than in the standard case until the end of the season, this is when there are only a few deep ponds remaining. At this point the mean pond depth in both cases coincide. The smaller mean pond depths, despite very similar pond fraction is probably due to the more even distribution of snow melt across the surface and therefore less localised enhanced melting so the ice surface remains slightly smoother than the standard case even once melting has begun.

Total surface ablation is the same for the smooth snow case and the standard case. The ice volume has been reduced by 59%, less than a percent difference to the standard

case.

Due to the similar pond and ocean fractions in the smooth snow and standard cases the average surface albedo in the smooth snow case, figure 5.8, closely follows the albedo of the standard case throughout the 90 days.

The smooth snow case shows great similarity to the standard case. The only differences are at the start of the melt season when snow is present, once the snow has melted ponds form in the same areas of the surface as the standard case. Such similarity is probably due to the standard deviation in the smooth snow case being fairly close to that of the standard case.

5.2.3 Thick Snow

The role of snow thickness on snow, sea ice and melt pond evolution was investigated. An example of a thick snow cover was chosen with a mean thickness of 0.5 m (0.3 m in the standard case), this was selected as a snow depth that is realistic for first-year ice, based on the observations of Sturm *et al.* (2002), but is thicker than the mean first-year ice observed snow depth. Due to the imposed non-zero snow thickness in all cells the actual initial mean snow thickness measured in the model is 0.53 m. The standard deviation in snow thickness remains identical to the standard case value of 0.15 m. The fractional area distribution and mean depths are shown in figure 5.10. In the thick snow case the snow cover takes longer to reach its melting temperature compared to the thinner snow in the standard case. The first bare ice cells are exposed (due to snow melting through entirely in a cell) on day 176 which is 9 days later than in the standard case. Snow cover is removed from all cells over the next 9 days and due to the increased volume of water compared to the standard case the ice surface is flooded with deep ponds, at their maximum extent ponds cover 94.4% of the ice surface. Between day 180 and 187 the ice surface is covered with a few very large ponds that cover most of the surface, the mean pond area at this

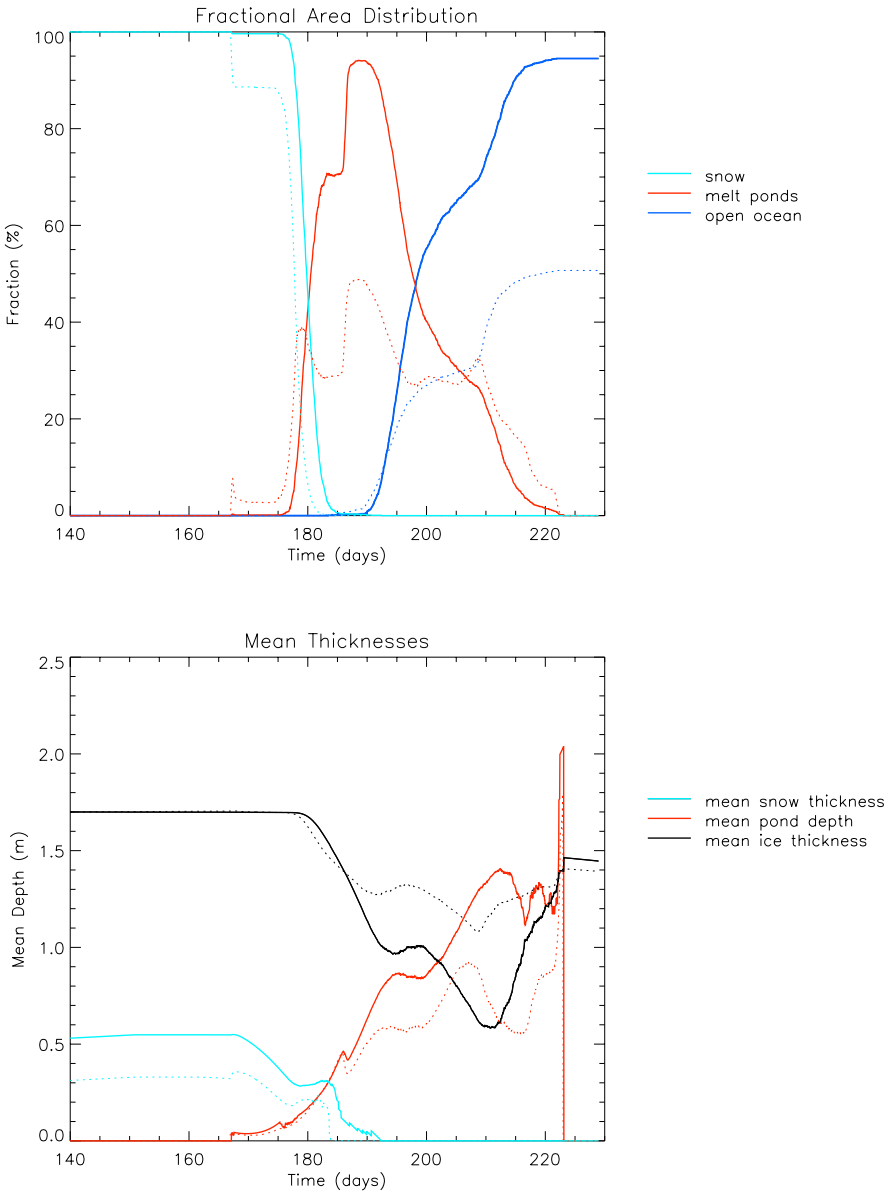

Figure 5.10: Top: Variation in the fractional distribution of surface area with time for the thick snow case, where mean ice thickness is 1.7 m, standard deviation in ice thickness of 0.2 m, mean snow thickness is 0.31 m and standard deviation in snow thickness is 0.15 m. Fraction of the surface with a snow cover (light blue), fraction of the surface covered with melt ponds (red), fraction of the surface with no ice cover (open ocean) is dark blue. The dashed lines represent the corresponding values for the standard first-year ice case shown in figure 5.3. Bottom: Change in mean snow depth (light blue), mean pond depth (red) and mean ice thickness (black) with time for the thick snow case. The dashed lines represent the corresponding values for the standard first-year ice case shown in figure 5.3.

time is 12533.3 m^2, which is a third of the domain area.

The ice surface remains flooded even as horizontal permeability increases, however the extra radiation absorbed by melt ponds compared to ice caused enhanced melting beneath ponds, consequently the ocean fraction rapidly increases from day 190 and by the end of the simulation only 5.5% of the total surface area still contains ice.

Due to the high ocean fraction and high volume of surface water the surface albedo, figure 5.8, drops rapidly as soon as ponds are able to form. Surface albedo is lower than the standard case from day 180 to the end of the simulation and significantly lower for much of this period, the minimum albedo is 0.009.

The thick snow sensitivity study shows that melt pond cover was highly sensitive to snow depth. Whilst the greater snow thickness meant that the initial mass of the floe was larger than in the standard case the the decrease in mass at the end of the simulation was 65338 kg (95.7%) compared to 40642 kg (62.2%) in the standard case.

5.2.4 Thin Snow

The mean snow depth here is 0.2 m, actually 0.24 m once the non-zero snow thickness snow condition has been imposed, which is 6 cm less than the mean snow thickness of 0.3 m in the standard case. The mean snow depth used in the thin snow case has been observed on thin ice, Sturm *et al.* (2002). Snow topography standard deviation is 0.15 m, which is the same as in the standard case. Fractional area distribution and mean depths are shown in figure 5.11. Despite the reduction in mean snow depth, snow cover is totally removed from all cells only a few hours earlier than the standard case. However since the initial volume of melt water produced by melting snow in the thin snow case is less than in the standard case (the initial volume of snow is 9440 m^3 compared to 12480 m^3 in the standard case), the mean pond depth and pond fraction are smaller than the standard case throughout the season. The maximum pond fraction, which occurs at the same time

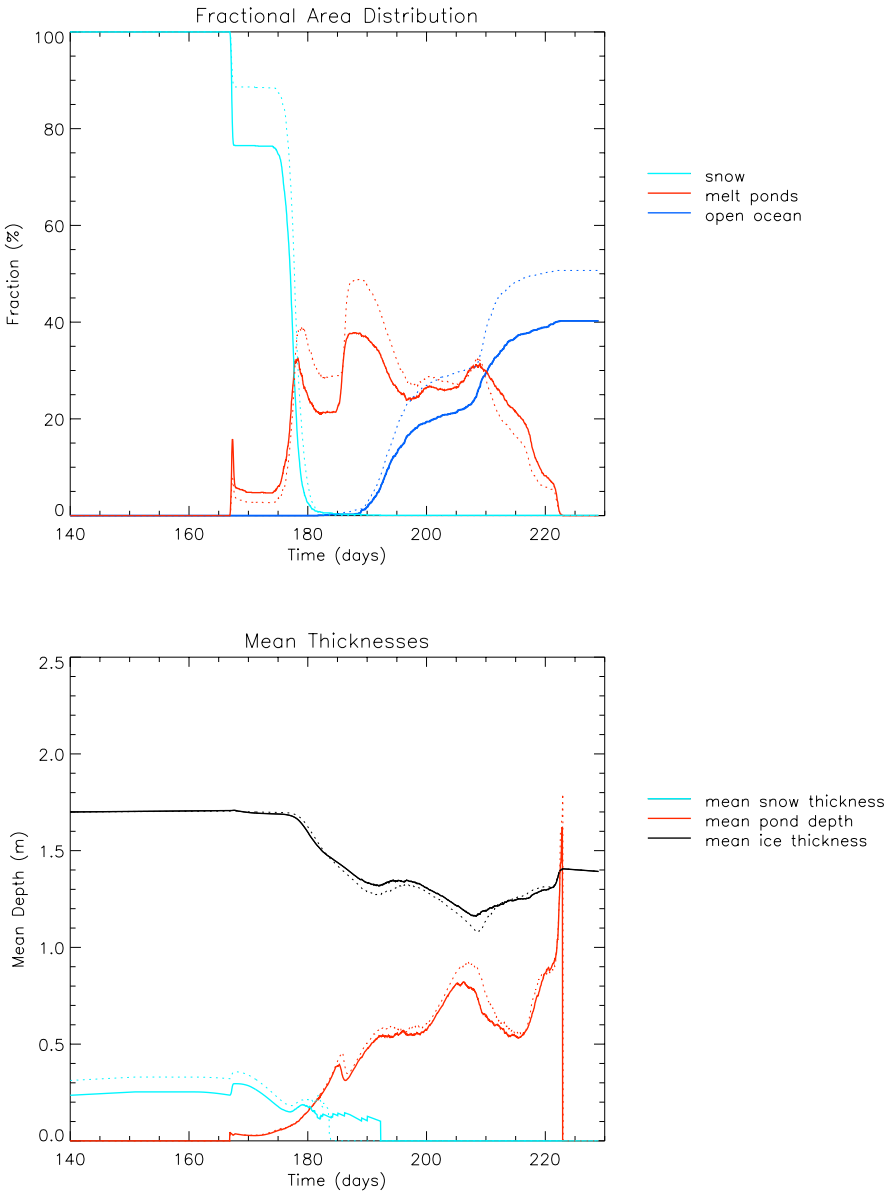

Figure 5.11: Top: Variation in the fractional distribution of surface area with time for the thin snow case, where mean ice thickness is 1.7 m, standard deviation in ice thickness of 0.2 m, mean snow thickness is 0.20 m and standard deviation in snow thickness is 0.15 m. Fraction of the surface with a snow cover (light blue), fraction of the surface covered with melt ponds (red), fraction of the surface with no ice cover (open ocean) is dark blue. The dashed lines represent the corresponding values for the standard first-year ice case shown in figure 5.3. Bottom: Change in mean snow depth (light blue), mean pond depth (red) and mean ice thickness (black) with time for the thin snow case. The dashed lines represent the corresponding values for the standard first-year ice case shown in figure 5.3.

in both cases, is 37.9% in the thin snow case compared to 48.8% in the standard case. The volume of ice melt per unit area is 0.87 m, which is 15 cm less than the standard case value of 1.01 m. Mean pond area, shown in figure 5.7, is smaller in the thin snow case than the standard case throughout the season. There is also much less variability in mean pond area in the thin snow case compared to the standard snow case, probably because the initial volume of water available was smaller. The maximum mean pond area in the thin snow case is 98.9 m^2 compared to 219.1 m^2 in the standard case. At the end of the melt season the ocean fraction in the thin snow case is approximately 10% less than in the standard case at 40.3%. Evolution of mean pond depth in the thin snow case closely follows the standard case since ponds form in the same areas in both cases, driven by topography. Maxima occur at the same times but with mean depths being lower in this case. The maximum pond depth is the same in both cases and occurs at the same location.

Due to the smaller pond fraction and ocean fraction the albedo, figure 5.8, is consistently higher than the standard case after snow melts. The minimum albedo here is 0.37.

5.2.5 Summary

In the cases above pond fraction, total ablation and average surface albedo were found to be most sensitive to an increase in snow thickness. In the thick snow case the snow thickness was 20 cm greater than in the standard case, which is still a possible mean snow thickness for Arctic first year ice. Increasing the initial combined mass of ice and snow by 4% compared to the standard case caused a reduction of 95.8% in mass over the 90 day season. Most of the ice cells melt through, meaning that from an initial grid of 1600 cells only 88 cells contained ice at the end of the season.

Reducing the initial mean snow thickness caused a small reduction in the volume of

ice and snow lost over the season but had very little impact on the average albedo.

Pond fraction and surface ablation were least sensitive to changes in surface roughness. Increasing the roughness of the snow caused an increase in mass removal but there was very little difference in average albedo when the roughness was increased. Reducing the roughness of the snow produced results very similar to the standard case. This is probably because the standard deviation in the smooth snow case was close to that of the standard case.

Excluding the thick snow cover case, which caused an impact on pond fraction and total ablation throughout the season, the impact of changing snow cover on evolution of pond coverage was mainly evident at the start of the season, creating a larger or smaller pond fraction than in the standard case. The evolution of pond coverage, however was very similar in all cases, with all maxima and minima occurring at roughly the same time suggest that the melt rate and ice surface topography were more of an influence than snow cover in ponds coverage.

5.3 Sensitivity to Ice Topography

To test sensitivity to ice topography two initial ice topographies were created: one which represents an ice surface more rough than the standard case and one which represents an ice surface topography more smooth than the standard case. In both simulations the snow topography is the snow topography used in the standard case simulation.

5.3.1 Rough Ice

The initial mean ice thickness in this case is 1.7 m, the same as in the standard case. The standard deviation has increased from 0.2 m in the standard case to 0.5 m, this is the standard deviation in ice thickness observed on smooth multi-year ice during the SHEBA

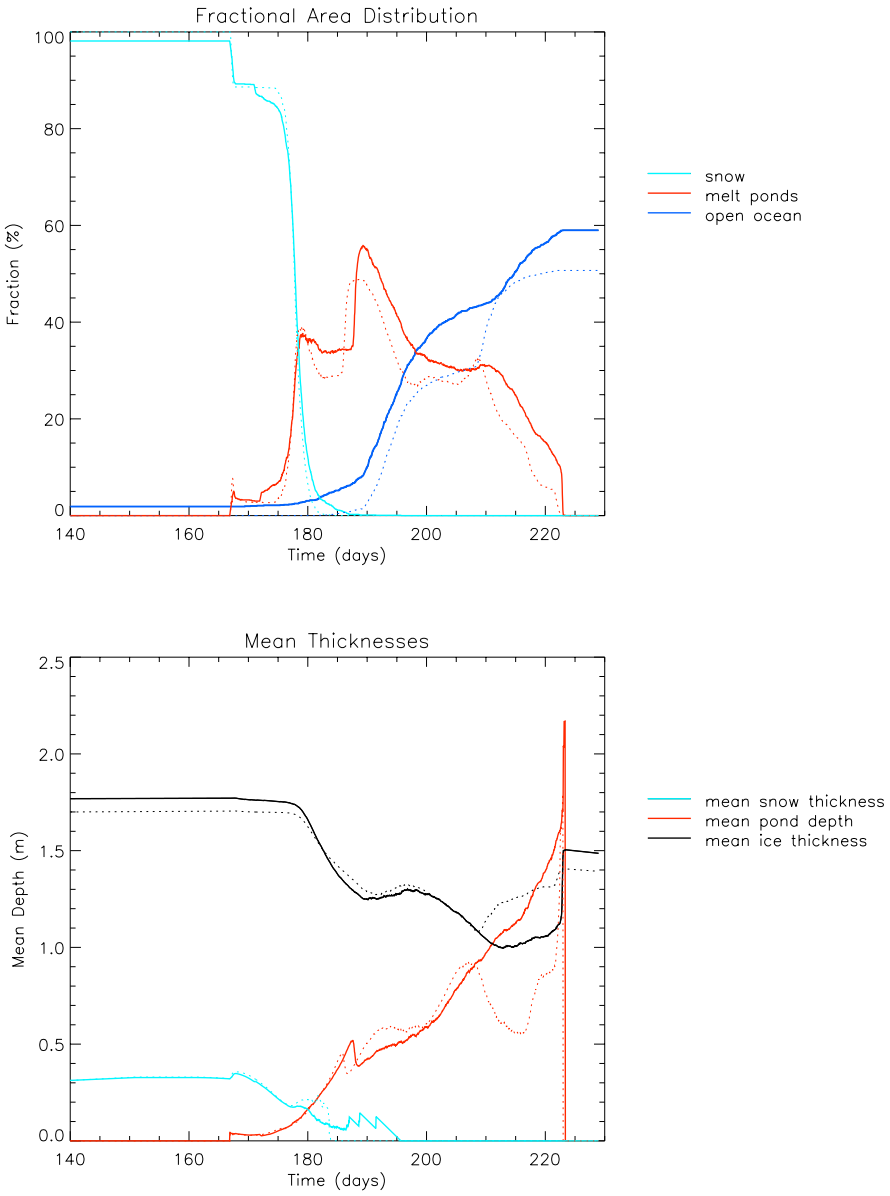

Figure 5.12: Top: Variation in the fractional distribution of surface area with time for the rough ice case, where mean ice thickness is 1.7 m, standard deviation in ice thickness of 0.2 m, mean snow thickness is 0.31 m and standard deviation in snow thickness is 0.15 m. Fraction of the surface with a snow cover (light blue), fraction of the surface covered with melt ponds (red), fraction of the surface with no ice cover (open ocean) is dark blue. The dashed lines represent the corresponding values for the standard first-year ice case shown in figure 5.3. Bottom: Change in mean snow depth (light blue), mean pond depth (red) and mean ice thickness (black) with time for the rough ice case. The dashed lines represent the corresponding values for the standard first-year ice case shown in figure 5.3.

experiments, this simulation is also compared to the multi-year ice smooth ice sensitivity study in Chapter 6. The rough ice topography has some more variability in ice thickness than the standard case and also has more cells with a surface ice height below sea level. Fractional distribution of pond area, ocean area, snow area and ice area and mean depths are shown in figure 5.12.

Compared with the standard case, snow cover is removed from cells at a different rate despite the snow topography being identical in both cases. This is because the snow melt rate depends on the temperature at the snow–ice interface, and this varies with ice thickness. Despite this the thinnest snow is removed entirely from cells at the same time as the standard case causing initial ponds to form in the rough ice case on day 167 as in the standard case. The initial pond fraction in the rough ice case which is governed by both snow topography and ice topography is identical to the standard case despite the difference in ice topography. After this the rough ice case has a greater pond fraction than the standard case for much of the season with a maximum pond fraction of 55.8%. The greater pond fraction is due to there being more cells with an ice surface height below sea level; melt water that drains into these cells will remain on the ice surface at that location since there is no vertical drainage of ponds with surfaces at or below sea level. This could also be the reason for the larger mean pond areas in the rough snow case compared to the standard case, shown in figure 5.13, from day 190 onwards. The maximum mean pond area occurs at roughly the same time in the rough snow case and the standard case but the maximum mean pond area in the rough snow case is 314.7 m^2 in the standard case.

The final ocean fraction in the rough snow case is 59% which is higher than the standard case 50%, probably due to there being more thin ice cells which melt through entirely in the rough ice case. The decrease in ice volume is 64.8% which is almost 6% greater than the decrease in ice volume in the standard case. In this case ice volume is lost by the

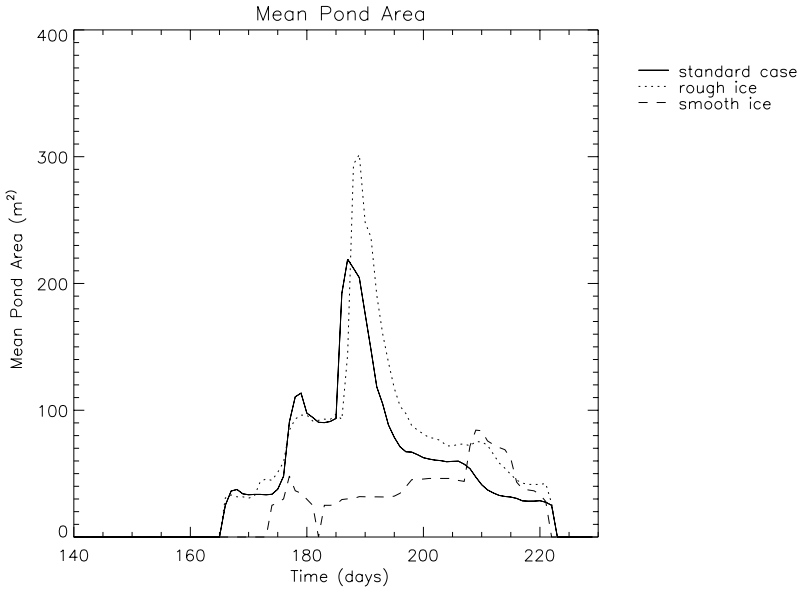

Figure 5.13: Mean individual pond area for the standard case and snow sensitivity studies.

thinner cells melting through, there is then an additional loss of melt water as melt water transported to these cells will be lost immediately to the ocean. Mean pond depth in the rough ice case exceeds mean pond depth in the standard case towards the end of the season. This is due to ponds that have formed in the lowest depressions. Due to the increased variability in ice thickness in the rough ice case the cells with lowest surface height may be further below sea level than cells with a low surface height in the standard case. Due to enhanced melting the deepest ponds increase in depth more quickly than shallower ponds. This is illustrated by a maximum pond depth of 2.26 m in the rough ice case which is much greater than the maximum pond depth of 1.87 m in the standard case.

The larger pond fraction and ocean fraction in the rough ice case compared to the standard case cause the albedo, shown in figure 5.14, to be substantially lower in the rough ice case than the standard case and the lowest average albedo is 0.24.

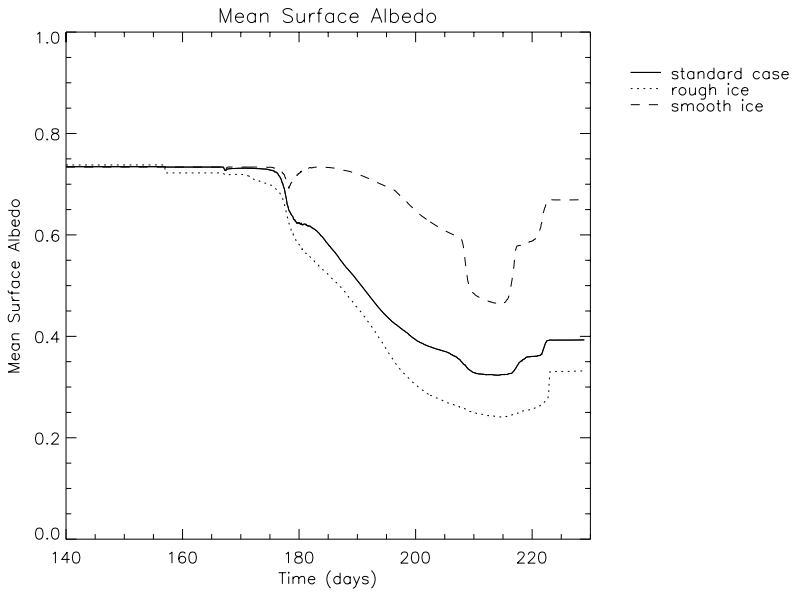

Figure 5.14: Change of aerially averaged surface albedo with time for the standard case (solid line) and ice sensitivity studies.

5.3.2 Smooth Ice

The standard deviation of the ice in this case is 0.02 m which is the standard deviation in ice thickness calculated from SHEBA measurements of ice thickness on smooth, young ice. This simulation differs considerably from the standard case. Fractional area distribution and mean depths are shown in figure 5.15.

Ponds form on day 167 when the thinnest cells melts through which is the same as the standard case, however within a day these ponds have drained away completely. Ponds form again as the remaining snow cover is removed but these ponds drain away within 5 days. As there is so little variability in ice thickness most cells have a positive freeboard and the drainage rate is large enough that ponds with positive hydraulic head cannot be sustained at this stage of the season.

A consistent pond cover forms around day 185 due to the melt rate increasing. The enhanced melt rate beneath ponds now causes sufficient melting that mean pond depth increases rapidly to 0.57 m by day 207. The mean pond depth in the standard case at

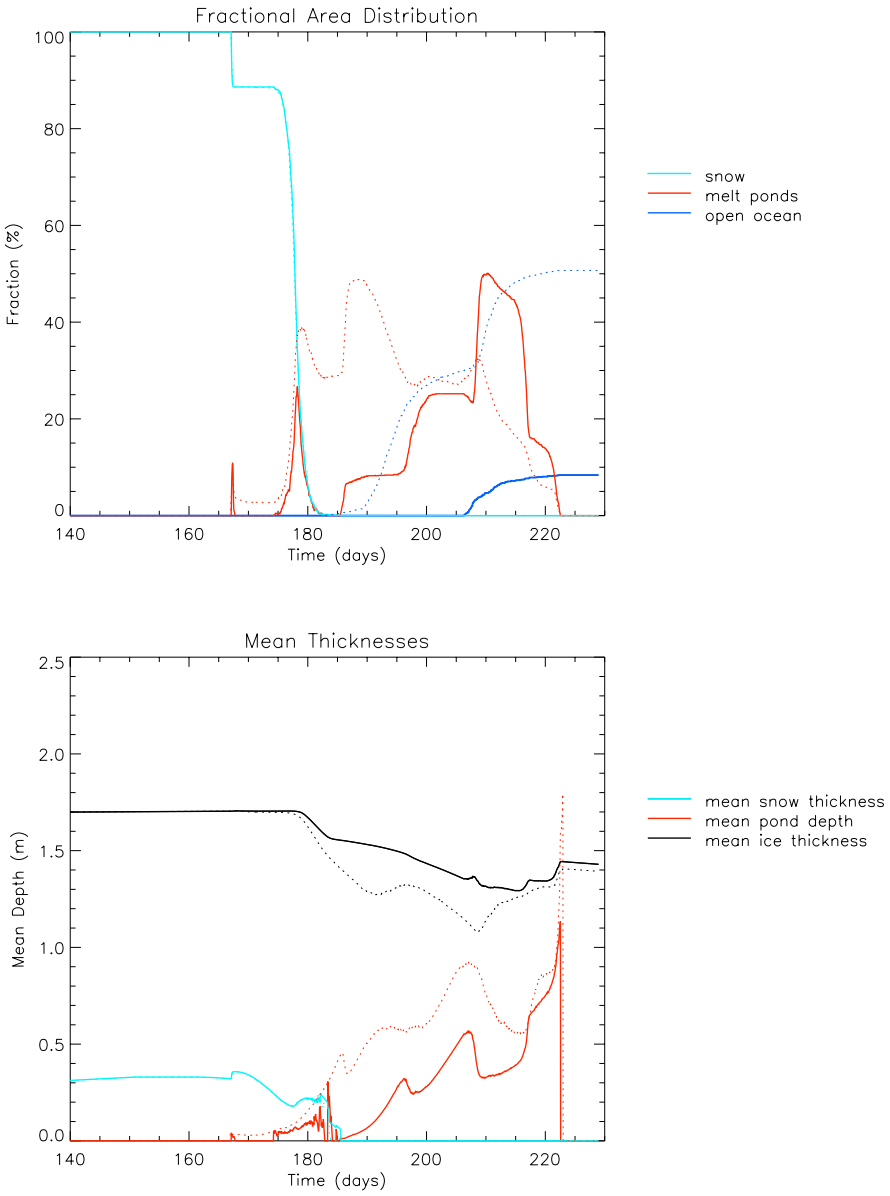

Figure 5.15: Top: Variation in the fractional distribution of surface area with time for the smooth ice case, where mean ice thickness is 1.7 m, standard deviation in ice thickness of 0.2 m, mean snow thickness is 0.31 m and standard deviation in snow thickness is 0.15 m. Fraction of the surface with a snow cover (light blue), fraction of the surface covered with melt ponds (red), fraction of the surface with no ice cover (open ocean) is dark blue. The dashed lines represent the corresponding values for the standard first-year ice case shown in figure 5.3. Bottom: Change in mean snow depth (light blue), mean pond depth (red) and mean ice thickness (black) with time for the smooth ice case. The dashed lines represent the corresponding values for the standard first-year ice case shown in figure 5.3.

this time is 0.91 m, so ponds are less deep in the smooth ice case. Mean pond area, figure 5.13, in the smooth snow case is much smaller than in the standard case and there is very little variability in pond area. The maximum mean pond area occurs late in the season compared to the standard case, on day 210, when melting has deepened ponds sufficiently that there are more regions below sea level. Maximum mean pond area reached 98.9 m^2 compared to 219.1 m^2 in the standard case. The maximum pond fraction of 50% is reached towards the end of the season on day 210, this is 22 days after the maximum pond fraction in the standard case.

As ponds form much later in the season in the smooth ice case than in the standard case and, due to smaller variability in ice thickness, cells melt through much later in the season in the smooth ice case (day 207 compared with day 188 in the standard case).

As the period of time that the ice surface is covered with ponds is shorter in the smooth ice case than in the standard case, the total ablation is 0.39 m which is much lower than the 1.01 m in the standard case. There is also therefore a reduction in the total mass lost, here the mass decreases by 27.8% compared with a decrease in mass of 62.2% in the standard case.

The average surface albedo, figure 5.14, is much greater than in all other cases. Even after ponds form the average albedo stays above 0.6 until the end of day 206 when there is a sudden drop in albedo, this coincides with the increase in pond fraction and some cells melting through to the ocean. The albedo at the end of the season has increased again to 0.69.

5.3.3 Summary

There was more variation in the evolution of pond coverage in the smooth ice case than in the rough ice case. There was also more variation in pond coverage in both the ice sensitivity studies than in the snow sensitivity studies. This highlights the importance of

ice topography in determining pond fraction. Altering the roughness of the surface varies the number of locations where the ice surface height is below sea level. Ponds persist in these locations, since ponds with their base above sea level drain vertically. Therefore pond fraction, surface ablation and albedo are sensitive to changes in ice surface topography. Rough ice caused an increase in ablation and pond fraction compared to the standard case and smooth ice caused a reduction in both. There is a limit to the increase in pond fraction due to increasing roughness since eventually, as roughness is increased, horizontal water transport will become more limited and pond fraction will diminish again (see Chapter 6).

5.4 Sensitivity to Vertical Permeability

For these two simulations standard first-year ice and snow topographies were used and the vertical permeability was reduced from 2.4 $\times 10^{-12}$ m^2 by one order of magnitude to 2.4 $\times 10^{-13}$ m^2 for the low permeability case and increased by one order of magnitude to 2.4 $\times 10^{-11}$ m^2 for the high permeability case. As permeability is difficult to measure there is much uncertainty about this parameter, Eicken *et al.* (2004), so the permeabilities chosen are simply to examine the differences compared to the standard case.

5.4.1 Low Permeability

In this case the vertical ice permeability has been reduced by one order of magnitude to 2.4 $\times 10^{-13}$ m^2, this reduces the vertical drainage rate through the ice. Fractional area distribution and mean depths are shown in figure 5.16.

Once the initial snow cover has melted away the pond fraction rapidly increases to 90%, this value is reached by day 180, the high pond fraction remains for 10 days and then decreases gradually as ice cells melt through, exposing the open ocean. The ocean

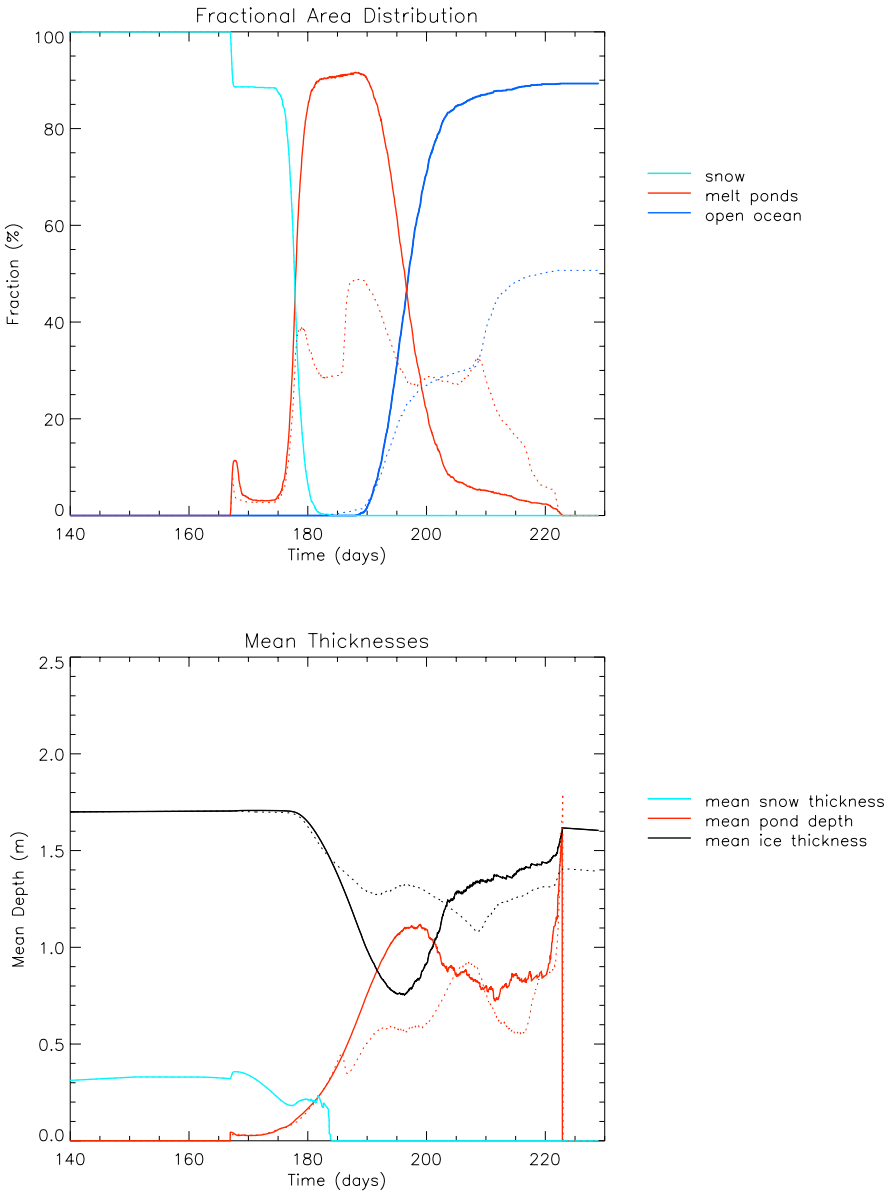

Figure 5.16: Top: Variation in the fractional distribution of surface area with time for the alternative low permeability case, where mean ice thickness is 1.70 m, standard deviation in ice thickness of 0.20 m, mean snow thickness is 0.31 m and standard deviation in snow thickness is 0.15 m. Fraction of the surface with a snow cover (light blue), fraction of the surface covered with melt ponds (red), fraction of the surface with no ice cover (open ocean) is dark blue. The dashed lines represent the corresponding values for the standard first-year ice case shown in figure 5.3. Bottom: Change in mean snow depth (light blue), mean pond depth (red) and mean ice thickness (black) with time for the low permeability case. The dashed lines represent the corresponding values for the standard first-year ice case shown in figure 5.3.

fraction increases rapidly from day 190 as surface flooding causes enhanced melting across much of the ice surface. The ocean fraction reaches 89% by the end of the 90 day run, this is almost double the surface area of 50% that is exposed as open ocean in the standard case by the end of the season. The total volume is reduced by 89.9% which is 30% greater than in the standard case. Total ablation is 1.53 m which exceeds the value in the standard case by more than 50 cm and is close to the value of the total ablation in the thick snow sensitivity study.

The mean ice thickness decreases much earlier in the season than in the standard case, this is due to surface water enhancing the melt rate in ice beneath ponds. As less water is able to drain away ponds are deeper than the standard case. The mid-season maximum pond depth occurs on day 198, which is after the maximum pond fraction has been reached. The maximum pond depth is reached earlier in the season than in the standard case, this is because of the enhanced rate of melting below ponds causes ponds to be deeper. The increase mean pond depth corresponds to a drop in mean ice thickness.

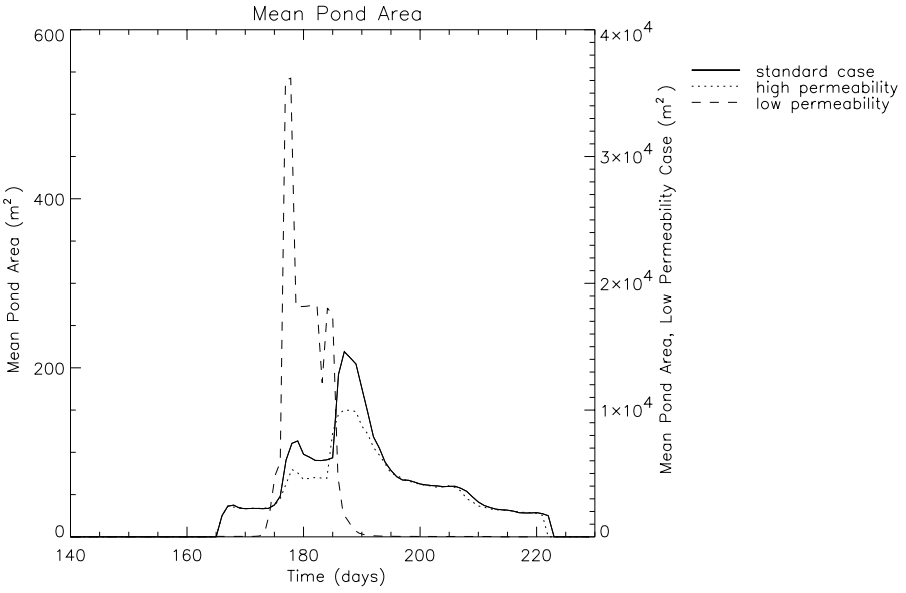

Figure 5.17: Mean individual pond area for the standard case and snow sensitivity studies. Scale for the low permeability case (dashed line) is on the right-hand side.

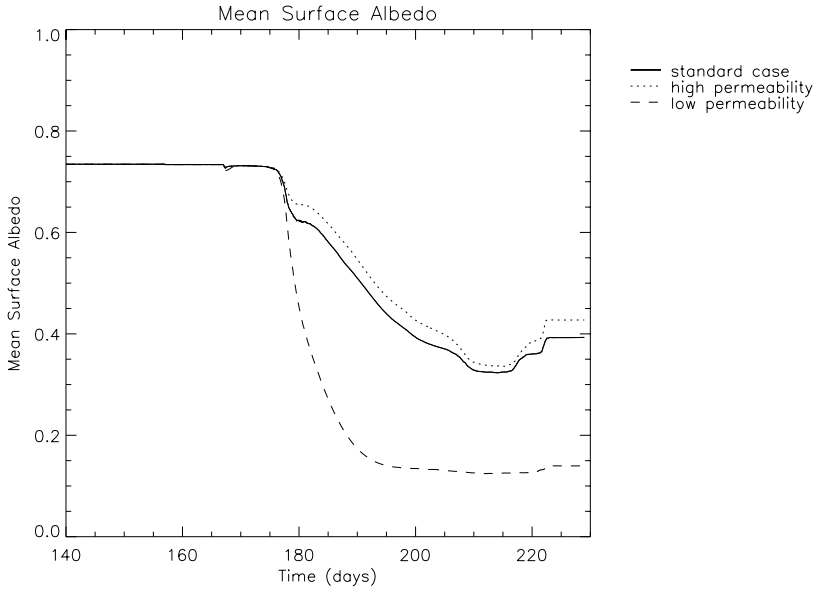

Figure 5.18: Change of aerially averaged surface albedo with time for the standard case and permeability sensitivity studies.

The maximum mean pond area of 36175 m^2, shown in figure 5.17, is several orders of magnitude larger than the maximum mean pond area of 219 m^2 in the standard case. The large mean pond area in the low permeability case is due to most of the surface being flooded with one large pond. The mean pond area remains several orders of magnitude larger than the standard case even as ocean cells melt through, demonstrating that the surface is continually flooded with water. The mean surface albedo, shown in figure 5.18, is also therefore much lower than the standard case, throughout the season, as soon as snow has melted. This is due to the combination of a large pond fraction and a large ocean fraction.

5.4.2 High Permeability

In this case the vertical ice permeability is 2.4 $\times 10^{-11}$ m^2 compared to 2.4 $\times 10^{-12}$ m^2 in the standard case. Fractional area distribution and mean depths are shown in figure 5.19. The increase in ice permeability causes a small decrease in the maximum pond fraction compared to the standard case, otherwise pond evolution is very similar to the standard

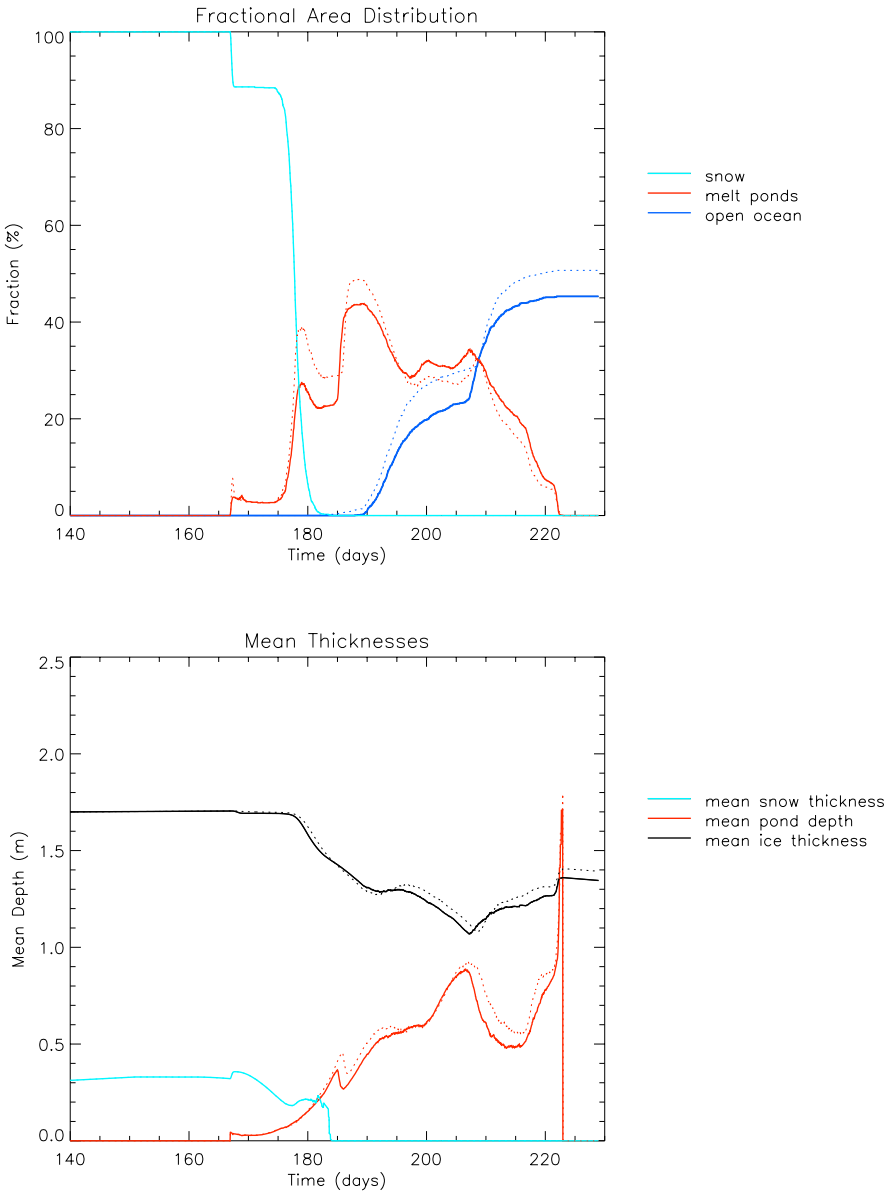

Figure 5.19: Top: Variation in the fractional distribution of surface area with time for the high permeability case, where mean ice thickness is 1.7 m, standard deviation in ice thickness of 0.2 m, mean snow thickness is 0.31 m and standard deviation in snow thickness is 0.15 m. Fraction of the surface with a snow cover (light blue), fraction of the surface covered with melt ponds (red), fraction of the surface with no ice cover (open ocean) is dark blue. The dashed lines represent the corresponding values for the standard first-year ice case shown in figure 5.3. Bottom: Change in mean snow depth (light blue), mean pond depth (red) and mean ice thickness (black) with time for the high permeability case. The dashed lines represent the corresponding values for the standard first-year ice case shown in figure 5.3.

case. Peaks and troughs occur at the same time, but for most of the season pond fraction is lower than the pond fraction in the standard case. The maximum pond fraction here is 56.7% compared to 59.7% in the standard case. The final ocean fraction in the high permeability case is 45%, this is lower than 50% in the standard case; this is due to the increase in drainage rate which removes water from the surface and therefore enhanced melting beneath ponds is reduced. Despite this, mean pond depth is almost the same as the standard case throughout the season.

5.4.3 Summary

Reducing the vertical permeability by one order of magnitude has a much larger impact on ablation, pond fraction and albedo than increasing permeability by one order of magnitude. This is because reducing permeability causes the surface to be flooded which causes melting over a greater surface area, the increased area of water then absorbs more radiation causing even more melting. When permeability is increased surface water drains more quickly from areas with positive hydraulic head but since most of the ponds have surfaces below or at sea level the impact of this is limited.

5.5 Summary

In this chapter the results of simulations of the evolution of melt ponds on first-year sea ice were presented. The main results are summarised in table 5.1. The standard case was initialised with ice and snow topographies that represent the conditions found on level first-year ice, in the standard case just more than half of the ice surface area melts away entirely during the melt season. To examine the sensitivity of pond fraction, pond depth and surface ablation to sea-ice topography, snow topography and permeability these parameters were varied. All snow and ice topographies used in the sensitivity studies

represent topographies typical of first-year ice.

Variations in the roughness of snow had the least impact on pond fraction, surface ablation and albedo. Increased snow thickness caused the largest increase in ice and snow ablation and the lowest albedos for most of the melt season, initially due to the surface being flooded with ponds and later because much of the domain was open ocean. Decreased snow thickness caused surface ablation to be smaller than the standard case, minimum albedo to be greater and maximum pond fraction to be smaller. This was because there was a smaller initial volume of melt water due to a smaller volume of snow.

Rough ice caused a greater maximum surface area covered in ponds more ablation and a lower minimum albedo than the standard case.Smooth ice caused a reduction in pond fraction and ice and snow ablation due to there being very few regions below sea level where ponds could form, the smooth ice surface had the highest minimum albedo of all the sensitivity studies.

Increasing vertical ice permeability, which is constant with time caused a decrease in pond fraction, ablation and caused minimum albedo to be higher because ponds were able to drain from the ice surface more rapidly. Decreasing vertical ice permeability caused the surface to be flooded with ponds and hence pond fraction was greater and total albedo lower than the standard case, but still less than the thick snow case. The minimum albedo was much lower than the standard case due to the surface being flooded with ponds.

The results summarised here are compared to other model and observational data in chapter 7 and conclusions about the model results are made in chapter 8. In the next chapter, I present a corresponding set of simulations for multi-year ice. The initial snow and ice topographies in chapter 6 are chosen to represent conditions in multi-year ice just as the initial topographies chosen in this chapter represent conditions on first-year ice. The sensitivity studies are the same as those described in this chapter. The rough first-year

ice case (section 5.3.1) in this chapter is of comparable roughness (standard deviation in ice thickness is 0.5 m) to the smooth multi-year ice case described in the next chapter, section 6.3.1.

Model Run	Mean Ice Thickness (Standard Deviation) (m)	Mean Snow Thickness (Standard Deviation) (m)	Ice Ablation (m)	Ice and Snow Ablation (m)	Max. Pond Depth (m)	Max. Pond Fraction -	Min. Area Averaged Albedo -	Change in Ocean Fraction -
Standard Case	1.70 (0.20)	0.30 (0.15)	1.01	1.33	1.87	0.49	0.32	0.51
Rough Snow	1.70 (0.20)	0.30 (0.25)	1.07	1.45	1.88	0.54	0.3	0.56
Smooth Snow	1.70 (0.20)	0.10 (0.25)	1.00	1.31	1.87	0.48	0.32	0.49
Thick Snow	1.70 (0.20)	0.50 (0.10)	1.62	2.15	2.20	0.94	0.09	0.95
Thin Snow	1.70 (0.20)	0.20 (0.15)	0.87	1.10	1.86	0.38	0.37	0.40
Smooth Ice	1.70 (0.02)	0.30 (0.15)	0.39	0.70	1.37	0.50	0.46	0.08
Rough Ice	1.70 (0.50)	0.30 (0.15)	1.12	1.44	2.46	0.56	0.24	0.59
Low Permeability	1.70 (0.20)	0.30 (0.15)	1.53	1.84	2.11	0.91	0.12	0.89
High Permeability	1.70 (0.20)	0.30 (0.15)	0.96	1.28	1.88	0.44	0.34	0.45

Table 5.1: Summary of important results from the standard first-year ice case and sensitivity studies.

Chapter 6

Simulations of Sea-Ice Melt Ponds on Snow-Covered Multi-Year Ice

In this section nine simulations of the sea-ice–melt-pond model are described. As in the first-year ice simulations described in the previous chapter the purpose of these simulations is to examine the sensitivity of aerial pond fraction, pond depth and surface ablation to snow topography, ice topography and vertical ice permeability using initial conditions that represent multi-year ice. The model is run for one melt season from day 140 to day 230 using forcing data for incoming shortwave radiation, air temperature 10 m above the ice surface, specific humidity, air pressure, wind speed and ocean heat flux all derived from SHEBA data following Taylor (2003). The ice and snow topographies represent conditions found in multi-year ice, although due to the method used to create the ice surface topographies (described in chapter 4) ridging is not modelled. The standard case results are described first, followed by simulations that use the standard case ice topography and vary snow topographies, next are cases where the standard snow cover is used and the ice topography is altered, and finally cases where the standard case snow and ice topography is used and the vertical ice permeability is varied.

As with the first-year ice results described in chapter 5, melt pond coverage showed very little sensitivity to changes in the roughness of the initial snow cover compared to the standard case. Unlike the first-year ice simulations thick snow caused very little increase in pond coverage. In the ice sensitivity studies I found that reducing the roughness of the ice surface caused an increase in pond coverage, the smooth multi-year ice case can be compared to rough first-year ice case and there are some similarities between them. Increasing the roughness of the ice from the standard case caused very little change in pond coverage. Increasing permeability caused a reduction in pond coverage and reducing permeability caused an increase in pond coverage. Compared to the first-year ice sensitivity studies multi-year ice was found to be less sensitive to all parameters.

6.1 Standard Case

The generated standard multi-year ice topography uses a mean thickness of 2.5 m, this mean thickness was taken from the SHEBA field experiment data. The standard deviation in ice thickness is 1.1 m; this value was chosen to fit in with the first-year ice standard deviations so is larger than the standard deviation of 0.53 m calculated from the SHEBA observations on multi-year ice but it is within the overall range of observations (Lüthje *et al.* (2006) uses a standard deviation of 1.5 m). Due to the extra variability in ice thickness compared to the standard first-year ice case 6% of the cells have an initial ice thickness of zero, hence the initial positive ocean fraction in figure 6.1. Having a low initial open ocean fraction is a limitation of the method of generating the topography but since it does not affect the evolution of the ice-covered fraction in any way (and, in any case, is within the range of observations) it is considered acceptable here. Whilst the mean ice thickness across the grid is 2.5 m this includes the initial open ocean cells, the mean ice thickness plotted in figure 6.1 is the mean thickness taken over all the cells with a positive

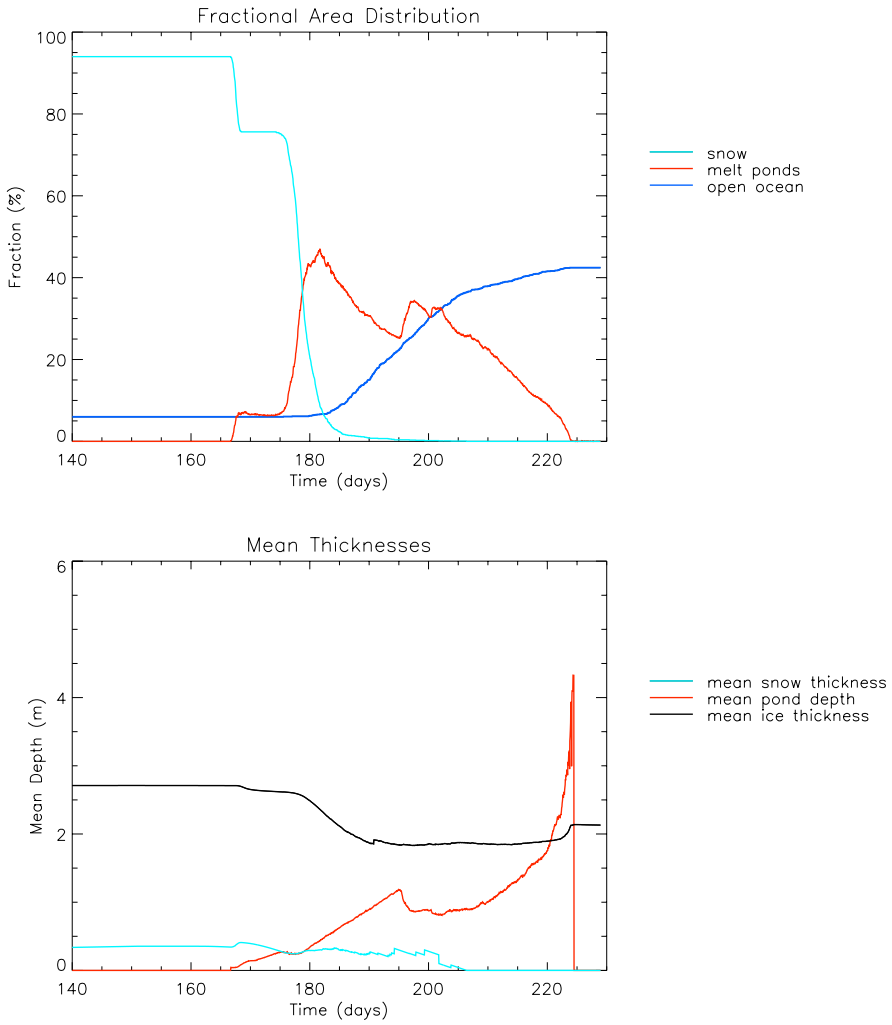

Figure 6.1: Top: Variation in the fractional distribution of surface area with time for the standard multi-year ice case, where mean ice thickness is 2.5 m, standard deviation in ice thickness of 1.1 m, mean snow thickness is 0.3 m and standard deviation in snow thickness is 0.25 m. Fraction of the surface with a snow cover (light blue), fraction of the surface covered with melt ponds (red), fraction of the surface with no ice cover (open ocean) is dark blue. Bottom: Change in mean snow depth (light blue), mean pond depth (red) and mean ice thickness (black) with time for the standard multi-year ice case.

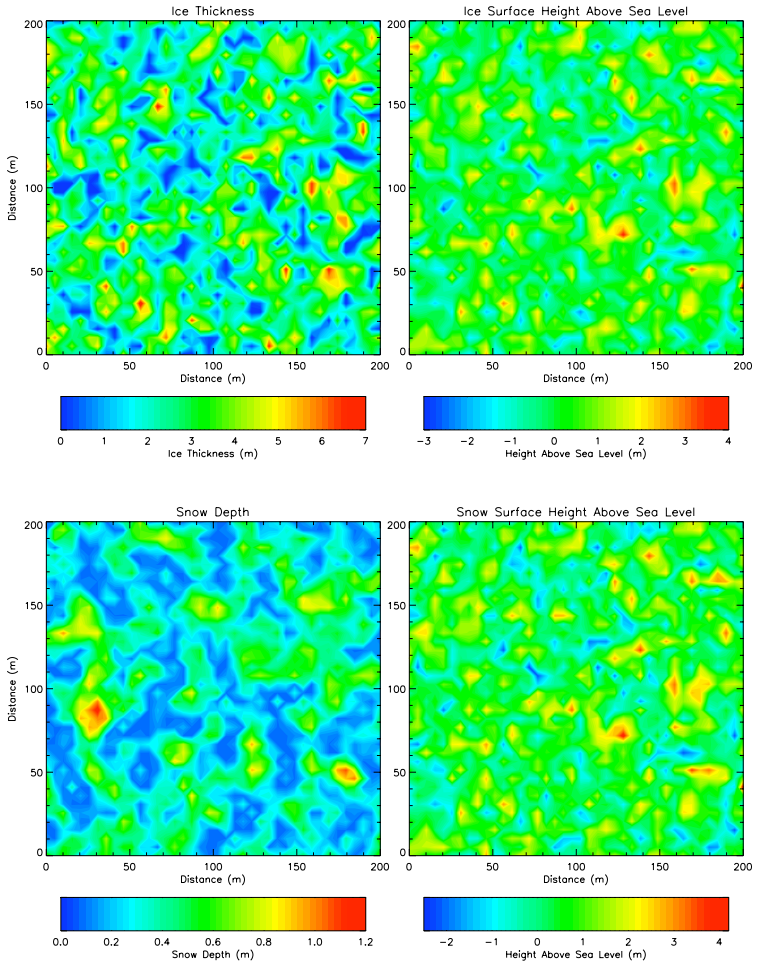

Figure 6.2: Contour plots of the initial mean ice thickness and snow depth in each cell, in the left hand column. The right hand column shows the height of the ice surface above sea level and the height of the snow surface above sea level. Surface heights above sea level can be negative.

ice thickness and therefore the initial mean ice thickness plotted is greater than 2.5 m at 2.7 m (this is also true in the sensitivity studies). Initial mean snow depth is 0.3 m with a standard deviation of 0.25 m; this is the same mean depth as the first-year ice standard mean snow depth, the standard deviation corresponds to the mean snow depth that has been observed on "hummocky" multi-year ice, Sturm *et al.* (2002). The initial ice and snow topographies and initial ice and surface snow heights above sea level are shown in figure 6.2.

The fractional area distribution and mean depths for the standard case is shown in figure 6.1 . The majority of snow cover has melted through by day 181, only 9.4% of cells have a snow cover after this time; initial ponds form 15 days before this on day 166 when the thinnest snow cover is removed. Pond fraction increases to 47.1%, its maximum value, by day 181, when most of the snow has melted away. After day 181 the pond fraction steadily decreases. Ponds persist in the locations in which they initially form, these are the lowest regions of the surface, where the ice surface is below sea level. Due to the roughness of the surface in the multi-year ice standard case melt water cannot travel far horizontally across the surface due to the prevalence of deep depressions in the ice cells. Pond surface height at these locations may start with surface height below sea level and as pond depth increases pond surface height will eventually reach sea level. These ponds are able to drain as the ocean fraction increases. As thin ice melts through the average thickness of the floe increases and so the freeboard increases (the sea level lowers with respect to the floe), creating a positive hydraulic head. This process allows some ponds to drain completely, reducing the pond fraction. As the ocean fraction increases pond fraction is decreased from melt water draining into cells with zero ice thickness. There is a 36% increase in ocean fraction between the start and end of the simulation. Between day 195 and 197 pond fraction increases, probably due to an increase in melt rate and large

ice surface area remaining.

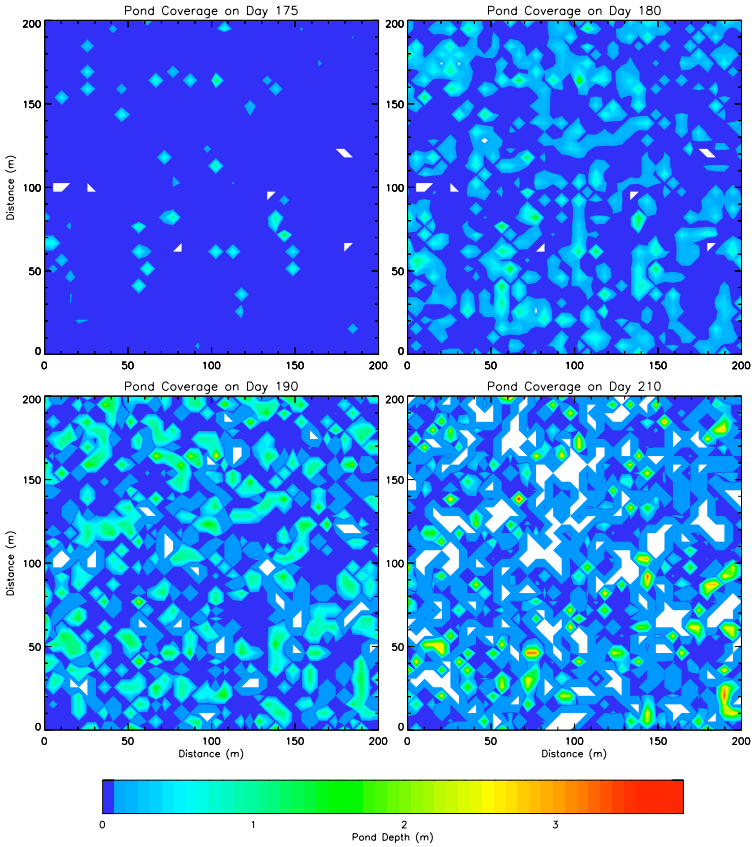

Figure 6.3: Contour plots showing simulated pond depth during the melt season. The top left panel shows pond depth on the day that ponds initially form and the bottom right panel shows pond coverage before freeze up. Dark blue represents bare ice and pond depth scale is illustrated in the colour bar with red for the deepest ponds. White regions are areas where sea ice has melted through entirely.

The decrease in mean ice thickness is less rapid than in the standard first-year ice case because thicker ice takes longer to reach its melting temperature: the temperature of the ocean is constant and temperature gradient in the thicker sea ice is smaller than the temperature gradient in thinner ice. The increase in mean ice thickness at the end of the season is due to pond surfaces freezing over and being reclassified as ice. The increase in mean ice thickness is small, 20 cm, meaning that most ponds drain away completely. Figure 6.3 shows the evolution of pond area and depth with time as a series of contour plots. Initially small ponds form at the lowest available locations of the ice surface. By

day 190 ponds have become larger and many of the smaller ponds have joined together, whilst other of the small ponds have drained away completely. By day 210 ponds have become deeper and their surface area is smaller.

Mean pond depth is deeper in the standard multi-year ice case than in the standard first-year ice case; mean pond depth exceeds 1 m by day 191 and a maximum pond depth of 4.35 m is attained. Deeper ponds are due to increased surface roughness and thicker ice.

The decrease in mass over the 90 day season is 53.9% made up of 1.32 m of ice ablation and 0.31 m snow ablation.

The mean pond area, shown in figure 6.4, is greatest earlier in the season when the surface is flooded with water due to snow melting. The maximum mean pond area reached is 147.3 m^2. Mean pond area decreases after this for most of the season, except between days 195 and 197 when there is a small increase in pond mean area which corresponds to an increase in pond fraction.

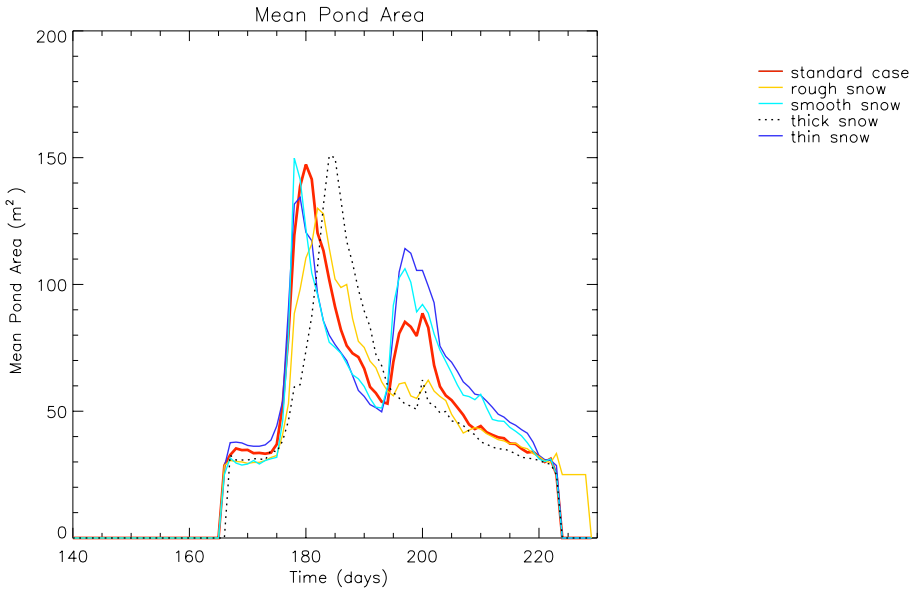

Figure 6.4: Mean individual pond area for the standard case and snow sensitivity studies.

Figure 6.5 shows the evolution of pond fraction and mean depths with the ice thickness

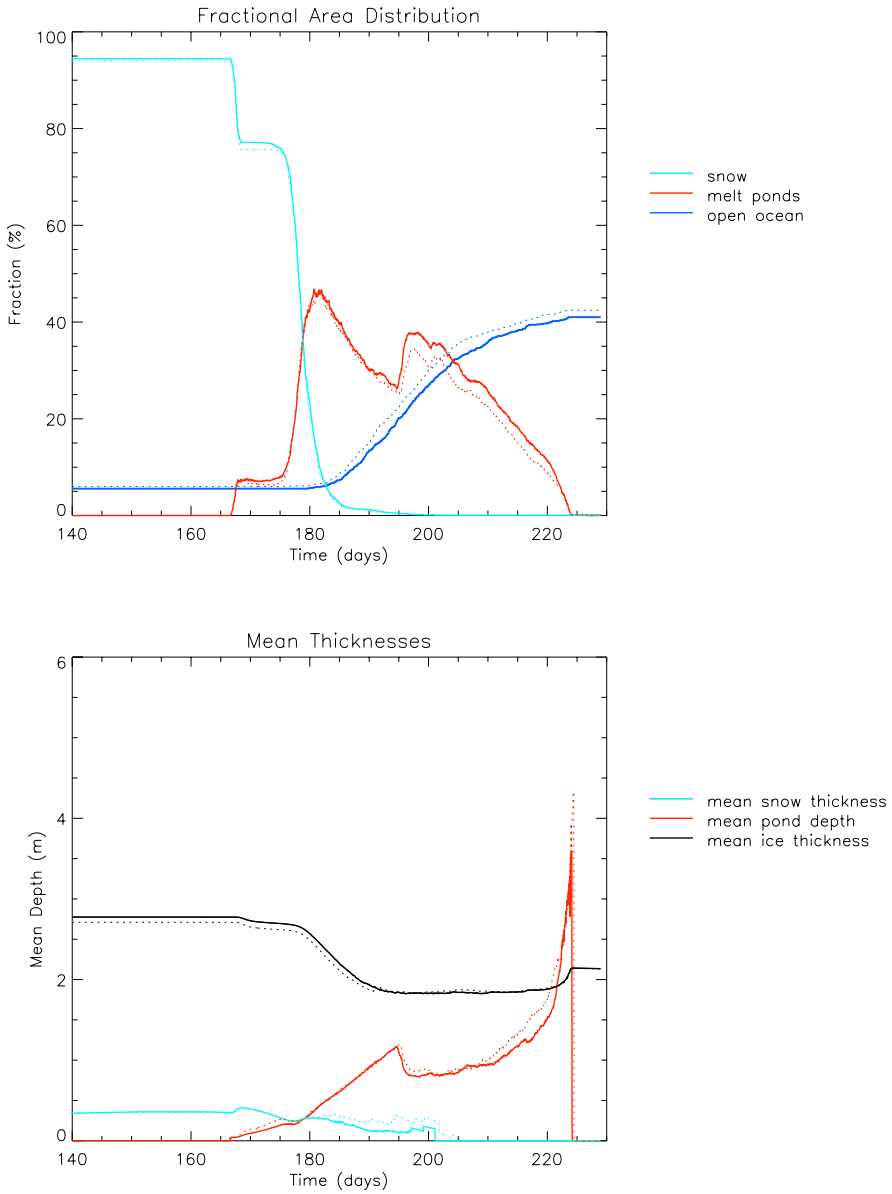

Figure 6.5: Top: Variation in the fractional distribution of surface area with time for the alternative standard multi-year ice case, where mean ice thickness is 2.5 m, standard deviation in ice thickness if 1.1 m, mean snow thickness is 0.3 m and standard deviation in snow thickness is 0.25 m. Fraction of the surface with a snow cover (light blue), fraction of the surface covered with melt ponds (red), fraction of the surface with no ice cover (open ocean) is dark blue. The dashed lines represent the corresponding values for the standard first-year ice case shown in figure 6.1. Bottom: Change in mean snow depth (light blue), mean pond depth (red) and mean ice thickness (black) with time for the standard multi-year ice case. The dashed lines represent the corresponding values for the standard multi-year ice case shown in figure 6.1.

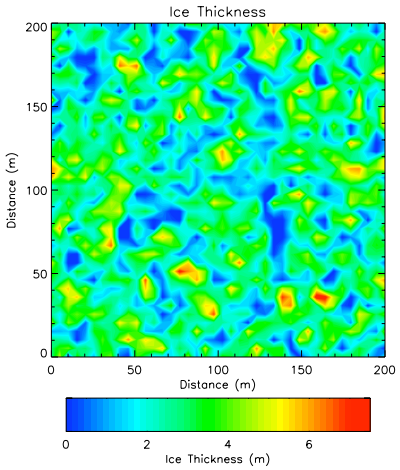

Figure 6.6: Contour plot of the initial mean ice thickness for an alternative multi-year ice standard case. Mean ice thickness is 2.5 m and standard deviation is 1.1 m. Despite the spatial differences between this topography and the standard case topography shown n figure 6.3 evolution of pond depth and pond fraction is very similar in both this and the standard case described above. The similarity in evolution in fractional area distribution and change in mean depth of ice, snow and pond is shown in figure 6.5.

distribution shown in figure 6.6. Due to the similarity in results the standard case results described in this section will be used to compare with the sensitivity studies.

6.2 Sensitivity to Snow Topography

Snow sensitivity studies were carried out to investigate the importance of snow cover in the evolution of pond fraction, in particular whether snow cover has an impact at the start of the season, in establishing pond initial position, and whether the differences in snow cover cause changes in pond cover over the entire season. The mean snow depths and standard deviations were chosen to be in the range of values that have been observed on multi-year ice. As in the first-year ice studies four scenarios are simulated, these are rough snow, smooth snow, thick snow and thin snow. The standard multi-year ice topography is used in all simulations.

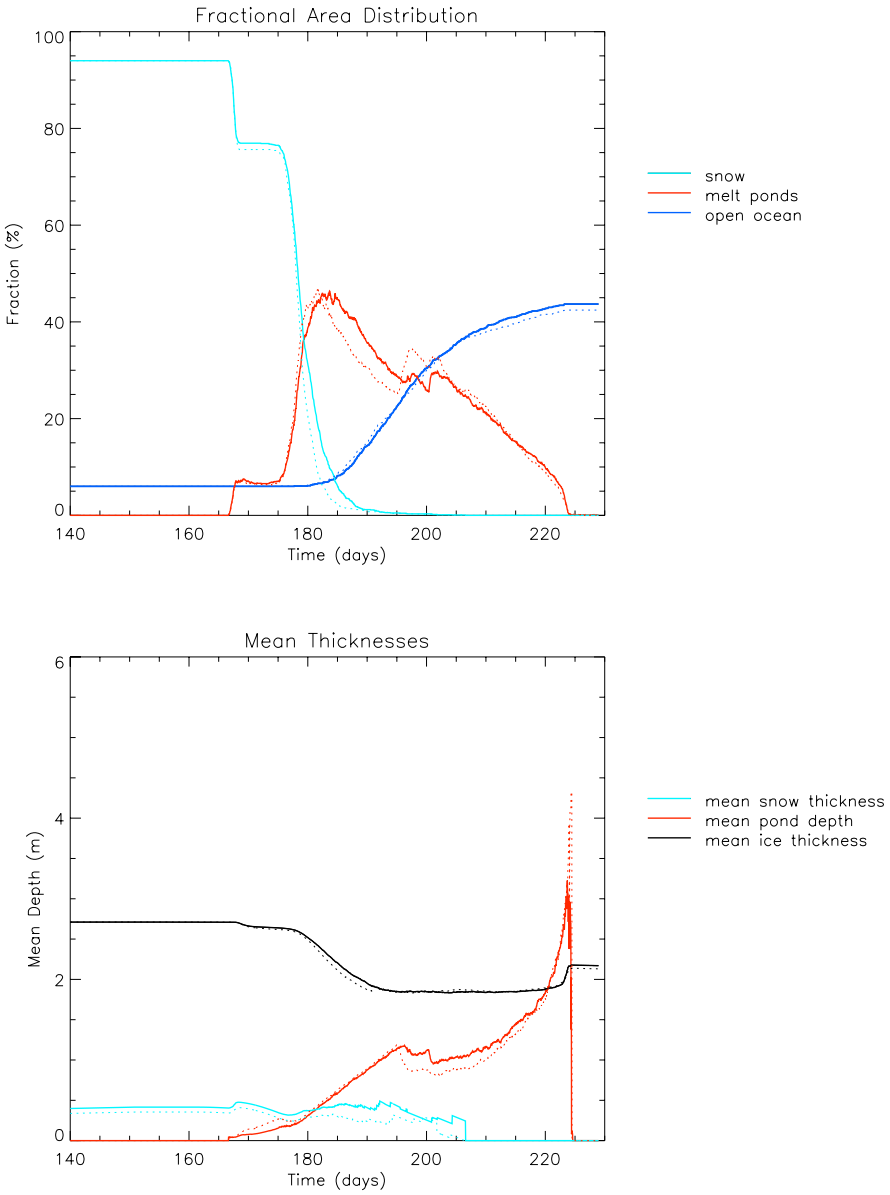

Figure 6.7: Top: Variation in the fractional distribution of surface area with time for the rough snow case, where mean ice thickness is 2.5 m, standard deviation in ice thickness of 1.1 m, mean snow thickness is 0.30 m and standard deviation in snow thickness is 0.40 m. Fraction of the surface with a snow cover (light blue), fraction of the surface covered with melt ponds (red), fraction of the surface with no ice cover (open ocean) is dark blue. The dashed lines represent the corresponding values for the standard multi-year ice case shown in figure 6.1. Bottom: Change in mean snow depth (light blue), mean pond depth (red) and mean ice thickness (black) with time for the rough snow case. The dashed lines represent the corresponding values for the standard multi-year ice case shown in figure 6.1.

6.2.1 Rough Snow

The mean snow thickness is this case is 0.3 m, the same as the snow thickness in the standard case. The standard deviation in snow thickness is 0.40 m compared to 0.25 m in the standard case, this is at the upper end of observed standard deviation values and is the variation that would be expected on deformed multi-year ice, Sturm *et al.* (2002). The fractional area distribution and change in mean depths are shown in figure 6.7.

Fractional area distribution and mean depths are very similar in the rough snow case to those in the standard case. Initial pond formation occurs in the same time step and pond fraction increases as snow cover is removed. Due to the increased variability in snow depth in the rough snow case, snow cover is entirely removed from all cells 3 days later than in the standard case on day 170; this delays the increase in pond fraction to its maximum value by 3 days. Maximum pond fraction occurs near the start of the season as in the standard case, due to surface flooding from melted snow. The maximum pond fraction is 46.4% compared to 47.1% in the standard case indicating that melt water is filling all the available locations and hydraulic head is too great to sustain ponds elsewhere. In the rough snow case pond fraction has a decreasing overall trend for the rest of the season. For much of the season pond fraction is a few percent greater in the rough snow case than in the standard case but pond fraction in the standard case becomes slightly greater than in the rough snow case towards the end of season. The greater pond fraction in the rough snow case for most of the season is probably due to the differences in the initial distribution of thick and thin snow, a few extra ponded cells are created by melting the ice surface to sea level.

The change in ocean fraction in the rough snow case is identical to the change in ocean fraction in the standard case until the last few days when the ocean fraction in the rough snow case increases more rapidly but then flattens out to a lower final ocean fraction. Final

ocean fraction in the rough snow case is 46.4%, which is 0.5% less than in the standard case.

Mean pond depth and mean ice thickness in the rough snow case are identical to mean pond depth and mean ice thickness in the standard case throughout the season. Total ablation is the same in the rough snow case as in the standard case.

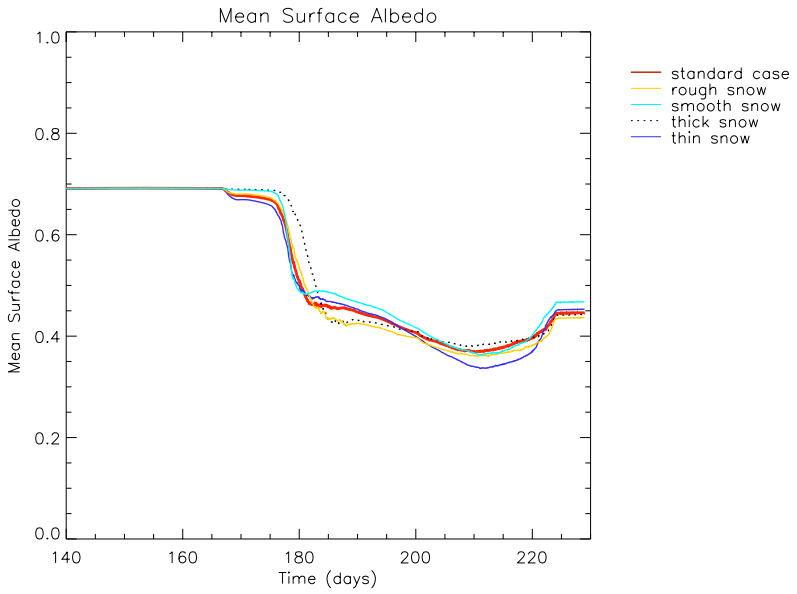

Figure 6.8: Change of aerially averaged surface albedo with time for the standard case and snow sensitivity studies.

Mean pond area, shown in figure 6.4 is largest at the start of the season when initial ponds form from snow melt. The maximum mean pond area is 130.3 m^2 which is smaller than the maximum mean pond area of 147.3 m^2 in the standard case. Pond shrink in area after the maximum mean pond area early in the season, unlike the standard case where some ponds grow again late in the season.

Due to the similarity in evolution of pond fraction and ocean fraction the surface albedo in the rough snow case closely matches the surface albedo in the standard case, shown in figure 6.8. Altering the snow surface roughness has very little impact on the evolution of pond fraction and no effect on ice ablation or pond depth.

6.2.2 Smooth Snow

The mean snow depth in the smooth snow case is 0.3 m which is the same as the mean snow thickness in the standard case, the standard deviation here is 0.10 m, compared to 0.25 m in the standard case. The standard deviation has been observed on thin ice, Sturm *et al.* (2002), and was the standard deviation in snow thickness used in the first-year ice smooth snow case. Fractional area distribution and change in mean depths are shown in figure 6.9.

The smooth snow topography means that there is little variation in snow thickness so snow cover is removed over just a few days, the thinnest snow melts through entirely causing a few initial ponds on day 167 which the same as in the standard case. The majority of the snow melts through between day 175 and 180 causing pond fraction to increase rapidly to its maximum of 48.5%. In the standard case the pond fraction reached at this time is 47.1%, the slightly increased pond fraction in the smooth snow case is due to there being a slightly greater volume of surface water due to all the snow cover being removed. The pattern of pond fraction for the rest of the simulation is very similar to the standard case. Over the season the decrease in ice volume is 51.2% in the smooth snow case compared to 51.9% in the standard case. Total ice ablation is 1.31 m in this case compared to 1.32 m in the standard case.

The main difference between the smooth snow case and the standard case is that the mean pond depth in the smooth snow case is consistently several centimetres lower than in the standard case despite there being a slightly larger area covered in ponds. This could be because melt is more gradual in the standard case, so some ponds deepen (due to enhanced melt) and are then filled with subsequent snow melt, making ponds deeper than in the smooth snow case. The average surface albedo, shown in figure 6.8, is very similar to the average albedo in the standard case due to the similarity in pond fraction,

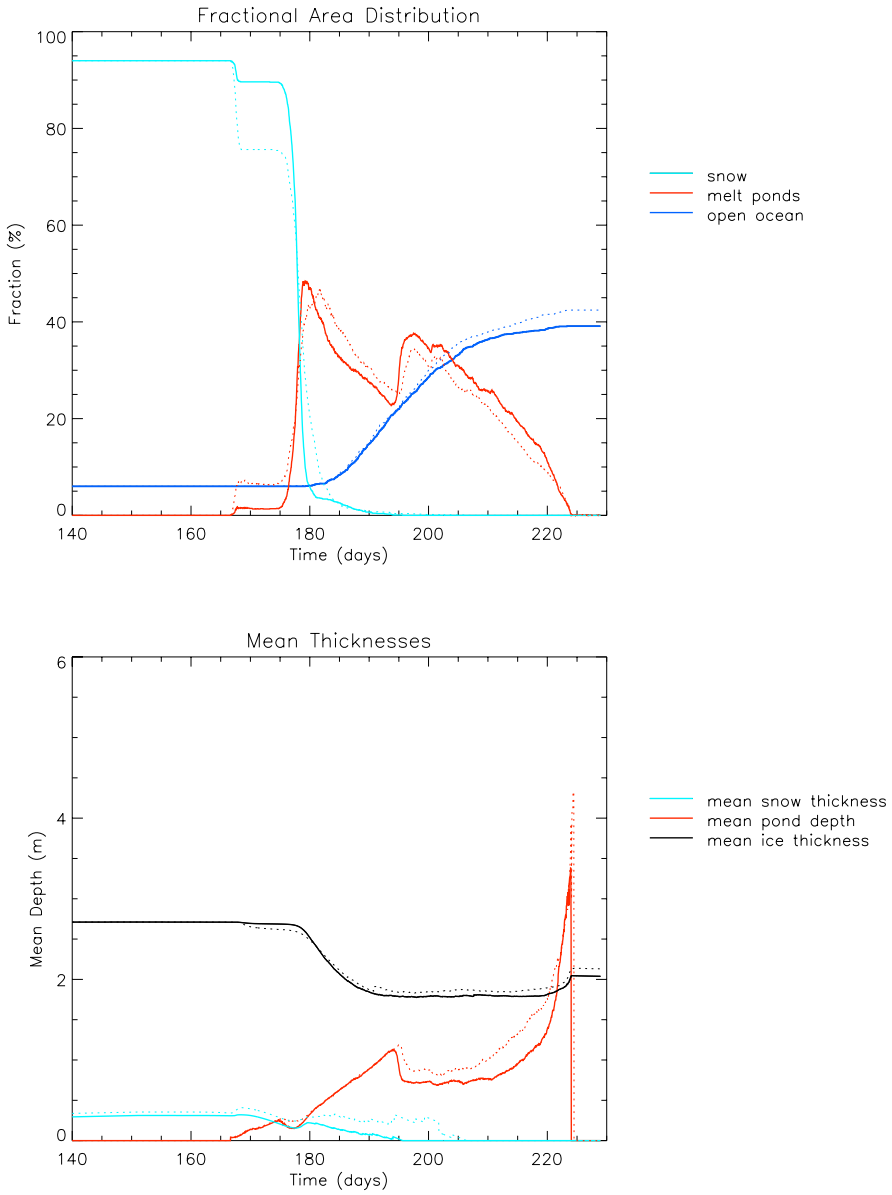

Figure 6.9: Top: Variation in the fractional distribution of surface area with time for the smooth snow case, where mean ice thickness is 2.5 m, standard deviation in ice thickness of 1.1 m, mean snow thickness is 0.30 m and standard deviation in snow thickness is 0.10 m. Fraction of the surface with a snow cover (light blue), fraction of the surface covered with melt ponds (red), fraction of the surface with no ice cover (open ocean) is dark blue. The dashed lines represent the corresponding values for the standard multi-year ice case shown in figure 6.1. Bottom: Change in mean snow depth (light blue), mean pond depth (red) and mean ice thickness (black) with time for the smooth snow case. The dashed lines represent the corresponding values for the standard multi-year ice case shown in figure 6.1.

although albedo in the standard case is slightly higher than in the smooth snow case when the pond fraction is lower and vice versa.

Mean pond area in the smooth snow case, shown in figure 6.4, exceeds the standard case at the start of the season due to more surface water being available because snow cover is removed in the smooth snow case in a short period compared to the standard case. The maximum mean pond area is 149.8 m^2. Increase in pond fraction corresponds to an increase in pond area, because ponds spread horizontally as pond surface levels rise and melt rate increases. Mean pond area is larger in the smooth snow case than the standard case for the second half of the season because there are smaller hydraulic gradients between cells (as there is less enhanced melting beneath ponds at the start of the season) so horizontal water transport is less rapid. The evolution of pond area is similar.

6.2.3 Thick Snow

The mean snow thickness here is 0.6 m, which is double the mean snow thickness in the standard case, the standard deviation is 0.25 m which is the same as in the standard case. These snow characteristics are observed on snow that forms on deformed ice, Sturm *et al.* (2002). Fractional area distribution and mean depths are shown in figure 6.10.

Although the first few ponds appear on day 167, the day of initial pond formation in the standard case, there are very few ponds in the thick snow case, only 1% of the surface is covered with ponds due to the mean snow thickness being greater than the standard case. Because the mean snow thickness is greater, snow takes 3 days longer to be completely removed from the ice surface than in the standard case. Most snow has finally melted by day 184 compared to day 181 in the standard case. Despite the extra volume of water available to form ponds the maximum pond fraction is 47.9% which is close to the standard case where pond fraction is 47.1%. There are several reasons for this, firstly melt that forms on cells with a positive surface height are likely to be high above sea level,

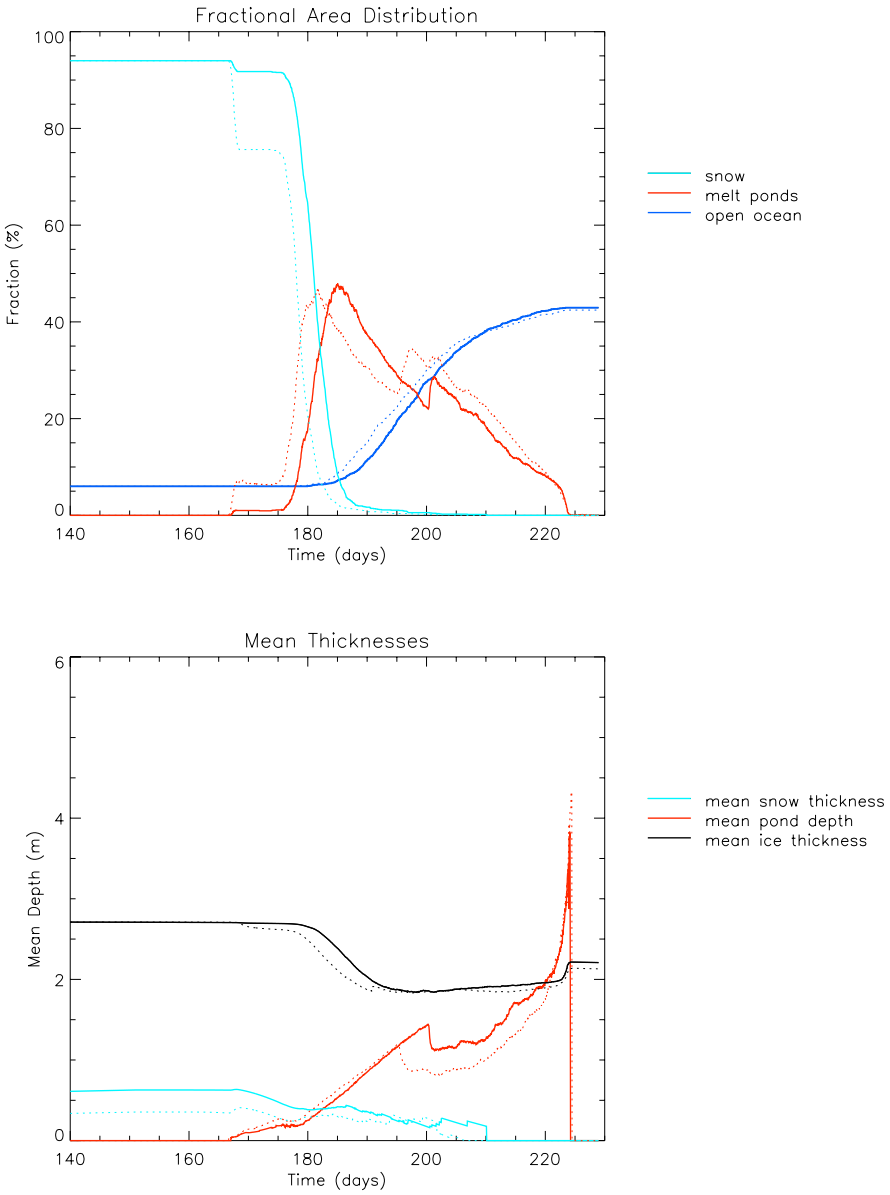

Figure 6.10: Top: Variation in the fractional distribution of surface area with time for the thick snow case, where mean ice thickness is 2.5 m, standard deviation in ice thickness of 1.1 m, mean snow thickness is 0.6 m and standard deviation in snow thickness is 0.25 m. Fraction of the surface with a snow cover (light blue), fraction of the surface covered with melt ponds (red), fraction of the surface with no ice cover (open ocean) is dark blue. The dashed lines represent the corresponding values for the standard multi-year ice case shown in figure 5.3. Bottom: Change in mean snow depth (light blue), mean pond depth (red) and mean ice thickness (black) with time for the thick snow case. The dashed lines represent the corresponding values for the standard multi-year ice case shown in figure 6.1.

and therefore have a large hydraulic head and water will drain vertically through the ice rapidly from these cells; secondly there was an initial open ocean fraction in this surface topography which will allow the extra surface melt to drain to the ocean; and finally mean pond area is small indicating that ponds are not connected together, so water fills a limited number of locations with negative surface heights, these cells can have a large negative surface height and provide a sink for the extra surface water, this is shown by the slightly greater pond depth in the thick snow case, (once sea level is reached in these ponds any excess water drains from the surface). The maximum mean pond area is 150.8 m^2 which is very close the maximum mean pond area of 147.3 m^2 in the standard case. The extra melt available at the start of the season is not significant here since throughout the season the mean pond area drops below the mean pond area in the standard case. Due to the similar pond and ocean fractions the average surface albedo is similar in the thick snow case to the standard case.

The increase in snow volume causes a decrease in total ice ablation in the thick snow case, 1.29 m compared to 1.32 m the standard case and the final ocean fraction is similar in both the thick snow case and the standard case; 42.9% in the thick snow case compared to 42.4% in the standard case. The change in ice volume is 50.5% in the thick snow case compared to 51.9% in the standard case. This means that the initial increase in snow volume had little impact on ice melting, in stark contrast to the effect of a thick snow cover on first-year ice (section 5.2.3).

6.2.4 Thin Snow

The mean snow thickness for the thin snow sensitivity study is 0.2 m, a snow thickness that would be expected on thin ice, Sturm *et al.* (2002), and is the mean snow thickness in the first-year ice standard case. The standard deviation is 0.25 m, which is the same standard deviation as in the standard multi-year ice case. The fractional area distribution

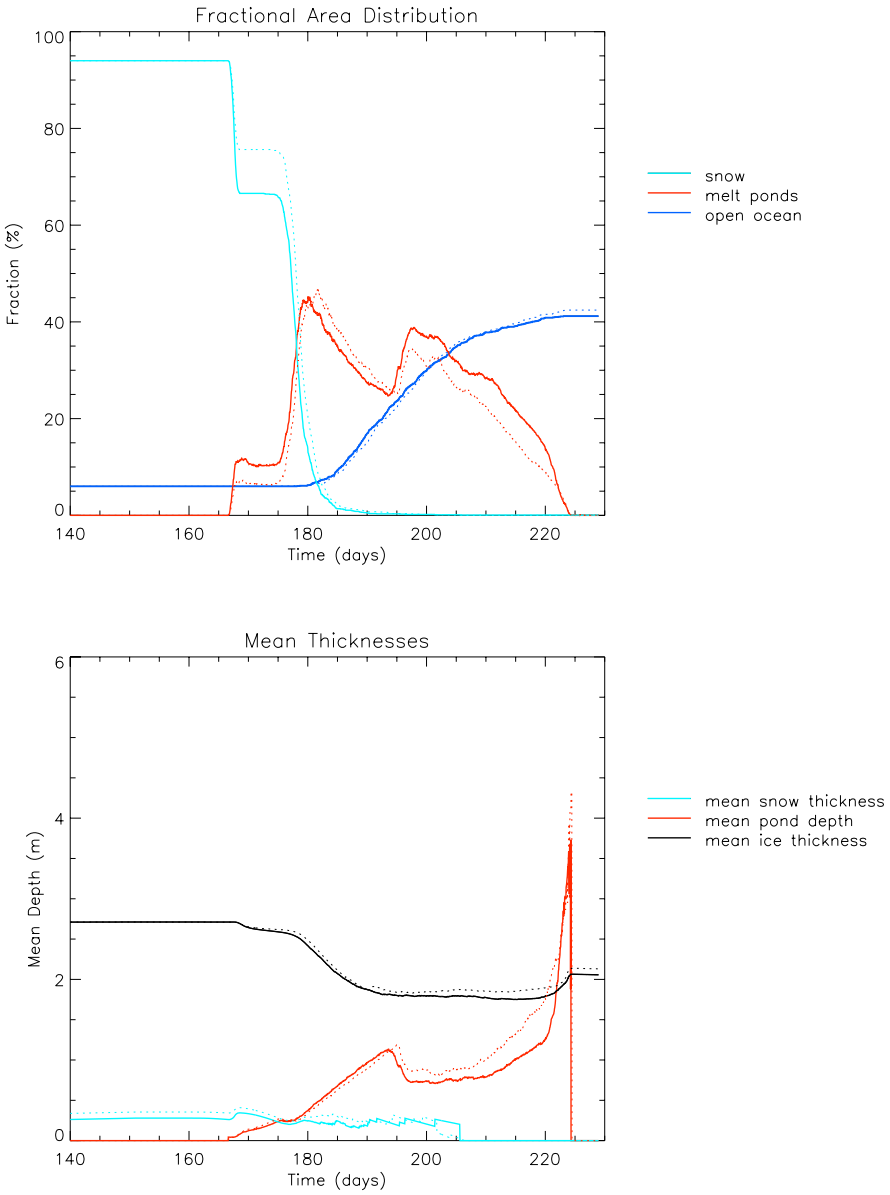

Figure 6.11: Top: Variation in the fractional distribution of surface area with time for the thin snow case, where mean ice thickness is 1.7 m, standard deviation in ice thickness of 0.2 m, mean snow thickness is 0.20 m and standard deviation in snow thickness is 0.25 m. Fraction of the surface with a snow cover (light blue), fraction of the surface covered with melt ponds (red), fraction of the surface with no ice cover (open ocean) is dark blue. The dashed lines represent the corresponding values for the standard multi-year ice case shown in figure 6.1. Bottom: Change in mean snow depth (light blue), mean pond depth (red) and mean ice thickness (black) with time for the thin snow case. The dashed lines represent the corresponding values for the standard multi-year ice case shown in figure 6.1.

and mean depths are shown in figure 6.11.

Initial pond formation in the thin snow case occurs in the same time step as initial pond formation in the standard case, on day 167. As there are more cells covered with the thinner snow in the thin snow case than in the standard case the initial pond fraction of 11.4% in the thin snow case is greater than the initial pond fraction of 6.7% in the standard case. Thin snow melts away entirely a few time steps earlier than in the standard case, which causes maximum pond fraction to occur a few time steps earlier than in the standard case. Other than this, the pattern of evolution of fractional area distribution is very similar to the standard case, although pond fraction is consistently several percent lower in the thin snow case than in the standard case throughout the season. The maximum pond fraction in the thin snow case is 45.3%, compared to 47.1% in the standard case. There are fewer ponds in the thin snow case than in the standard case, which is due to there being a smaller initial volume of snow.

The increase in ocean fraction in the thin snow case is identical to the increase in ocean fraction in the standard case until the end of the season. Over the last two weeks the ocean fraction in the standard case increases to slightly above the ocean fraction in the thin snow case. The final ocean fraction in the standard case is 42.4% compared to 41.2% in the thin snow case. The ocean faction is marginally lower in the thin snow case because there is less enhanced melting beneath ponds because on average pond depths are lower in the thin snow case, which decreases the number of ice cells that melt through.

Mean ice thickness decreases earlier in the season in the thin snow case than in the standard case because there is a greater volume of melt water available early in the season due to the thinner snow melting more quickly, the available water causes an increase in radiation absorbed causing enhanced melting. The mean ice thickness in the thin snow case remains thinner than the standard case throughout the season. This result causes a

greater mean pond depth in the thin snow case during the first half of pond development.

Maximum mean pond area in the thin snow case, shown in figure 6.4, is 134.4 m^2 which is smaller than the mean pond area in the standard case.

6.2.5 Summary

The standard multi-year ice topography used in all the simulations in the snow sensitivity studies has a surface that is rough enough to impede the horizontal flow of melt water across the ice surface. Ponds form and deepen in the cells with an ice surface height below sea level due to water flow from adjacent cells. Pond depth depends on the location of snow melt, this caused some variation in pond depth across the simulations. The evolution of pond fraction, mean pond area and average surface albedo were all very similar demonstrating that ice topography had a more dominant and lasting effect on pond coverage than snow topography.

6.3 Sensitivity to Ice Topography

The roughness of the ice surface may govern the area of melt ponds. If the surface is very rough melt ponds cannot spread over a large area. The purpose of this sensitivity study is to examine the effect that altering the surface topography has on the fraction of the surface covered in ponds, the average surface albedo and ice ablation. The ice topographies created represent rough multi-year ice and smooth multi-year ice. Rough multi-year ice is ice that has been deformed by melt ponds in previous melt seasons and by ridging. Long ridges have not been modelled but the standard deviation has been increased to the standard deviation expected in ridged ice. The smooth multi-year ice topography represents an ice surface that is less deformed than the standard case, and has a standard deviation close to rough first-year ice; this topography could also be considered

to represent thick rough first-year ice.

6.3.1 Rough Ice

The rough ice topography grid has the same mean ice thickness as the standard case, 2.5 m, but due to the increase in variability not every cell has a non-zero ice thickness initially. The initial ocean fraction in this case is 13.8%, hence the mean thickness of the non-zero ice cells increases to 3.4 m. The standard deviation in the rough ice study is 1.5 m which is the standard deviation expected on deformed ice taken from Lüthje *et al.* (2006). Fractional area distribution and mean depths are shown in figure 6.12.

Initial pond formation occurs in the same time step, on day 167, as in the standard case and snow melts through entirely at the same time in the rough ice case and in the standard case. Maximum pond fraction occurs immediately after the snow cover is totally removed, at which point the maximum pond fraction is 47.1% which is the same as the maximum pond fraction in the standard case and occurs in the same time step as in the standard case. After this the rough ice case has a pond fraction 2% to 7% higher than the standard case as shown in figure 6.12.

Whilst the initial ocean fraction is higher, 13.9% in the rough ice case compared to 6% in the standard case, the increases in ocean fraction occur at the same time in the rough ice case as in the standard case. The ocean fraction increases by 36.0% at the end of the simulation period in the rough ice case compared to 33.4% in the standard case. The larger initial ocean fraction causes the domain area averaged surface albedo in the rough ice case to be consistently lower than the standard case, as the pond fraction is similar in both cases.

The decrease in ice thickness follows the same pattern in both the rough ice case and the standard case. At the end of the season, as ponds freeze over, the ice thickness in the rough snow case increases by more than the ice thickness in the standard case which is

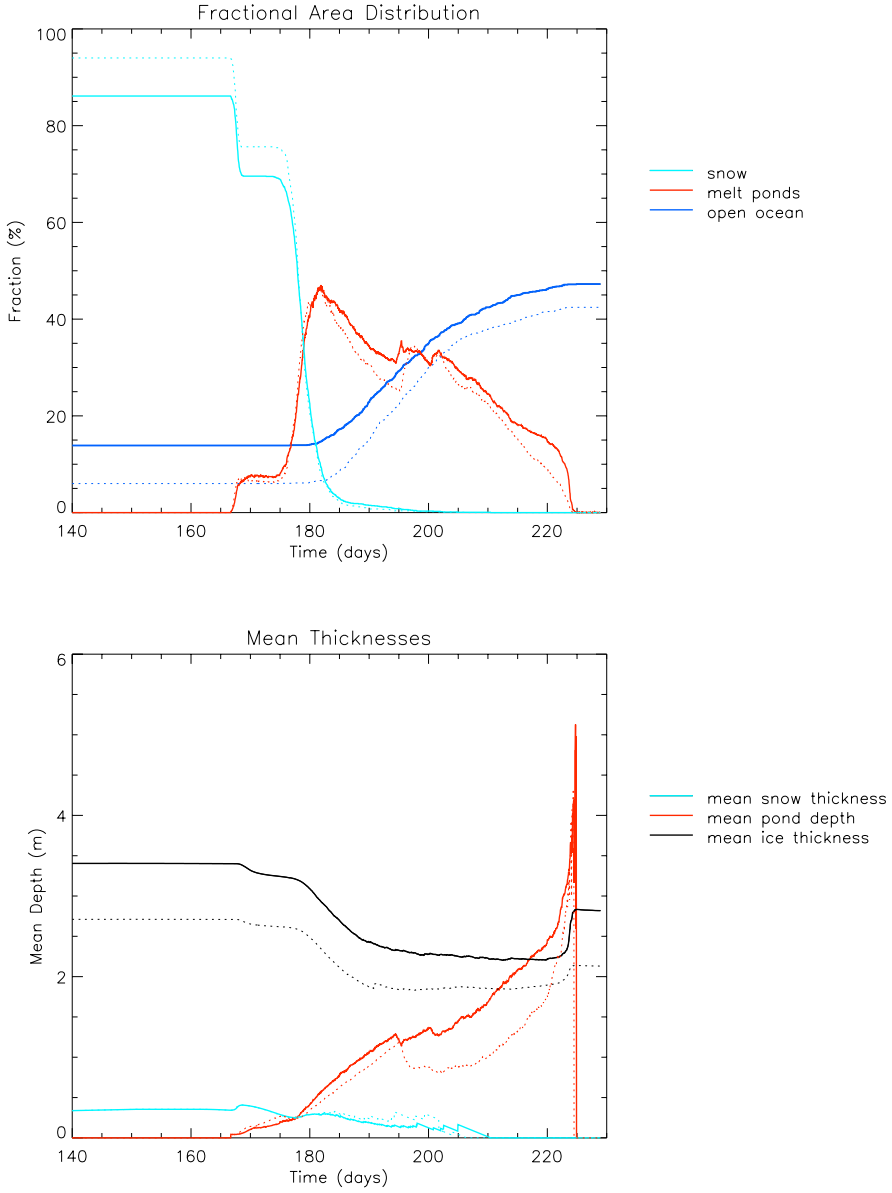

Figure 6.12: Top: Variation in the fractional distribution of surface area with time for the rough ice case, where mean ice thickness is 2.5 m, standard deviation in ice thickness of 1.50 m, mean snow thickness is 0.31 m and standard deviation in snow thickness is 0.25 m. Fraction of the surface with a snow cover (light blue), fraction of the surface covered with melt ponds (red), fraction of the surface with no ice cover (open ocean) is dark blue. The dashed lines represent the corresponding values for the standard multi-year ice case shown in figure 6.1. Bottom: Change in mean snow depth (light blue), mean pond depth (red) and mean ice thickness (black) with time for the rough ice case. The dashed lines represent the corresponding values for the standard multi-year ice case shown in figure 6.1.

because more water is retained on the surface in the rough ice case.

Mean pond depth in the rough ice case is deeper than pond depth in the standard case. This is because the lowest points in the rough ice case are further below sea level than the lowest points in the standard case. This can be seen in the difference in maximum pond depth, which is 4.35 m in the standard case and 5.70 m in the rough ice case.

Decrease in mass is 50.9% in the rough ice case compared to 54.0% in the standard case. This is because fewer cells melt through entirely because ice that is present is thicker than ice in the standard case and more water is retained at the surface at the end of the season.

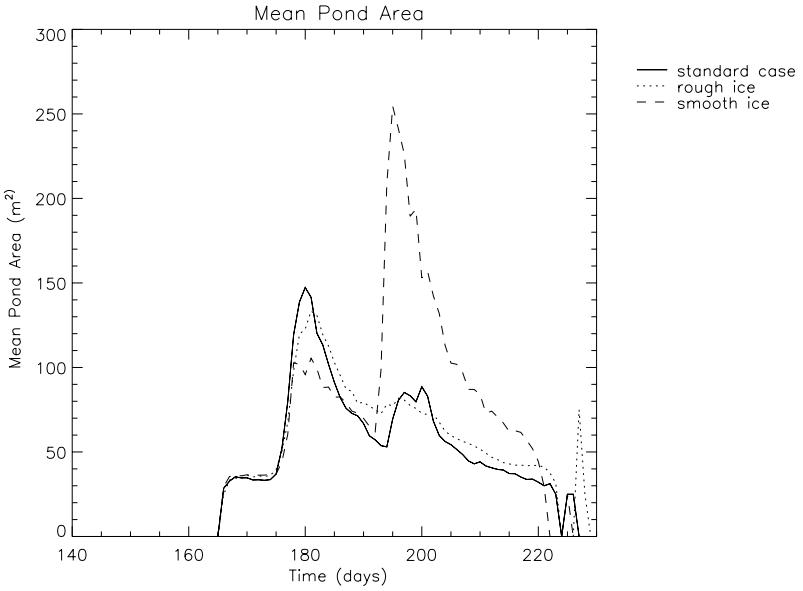

Figure 6.13: Mean individual pond area for the standard case and ice sensitivity studies.

Mean pond area in the rough ice case, shown in figure 6.13, reaches a maximum of 133.3 m^2 which is smaller than the maximum mean pond area of 147.3 m^2 reached in the standard case. Pond mean area is slightly smaller in the rough ice case than the standard case for much of the season.

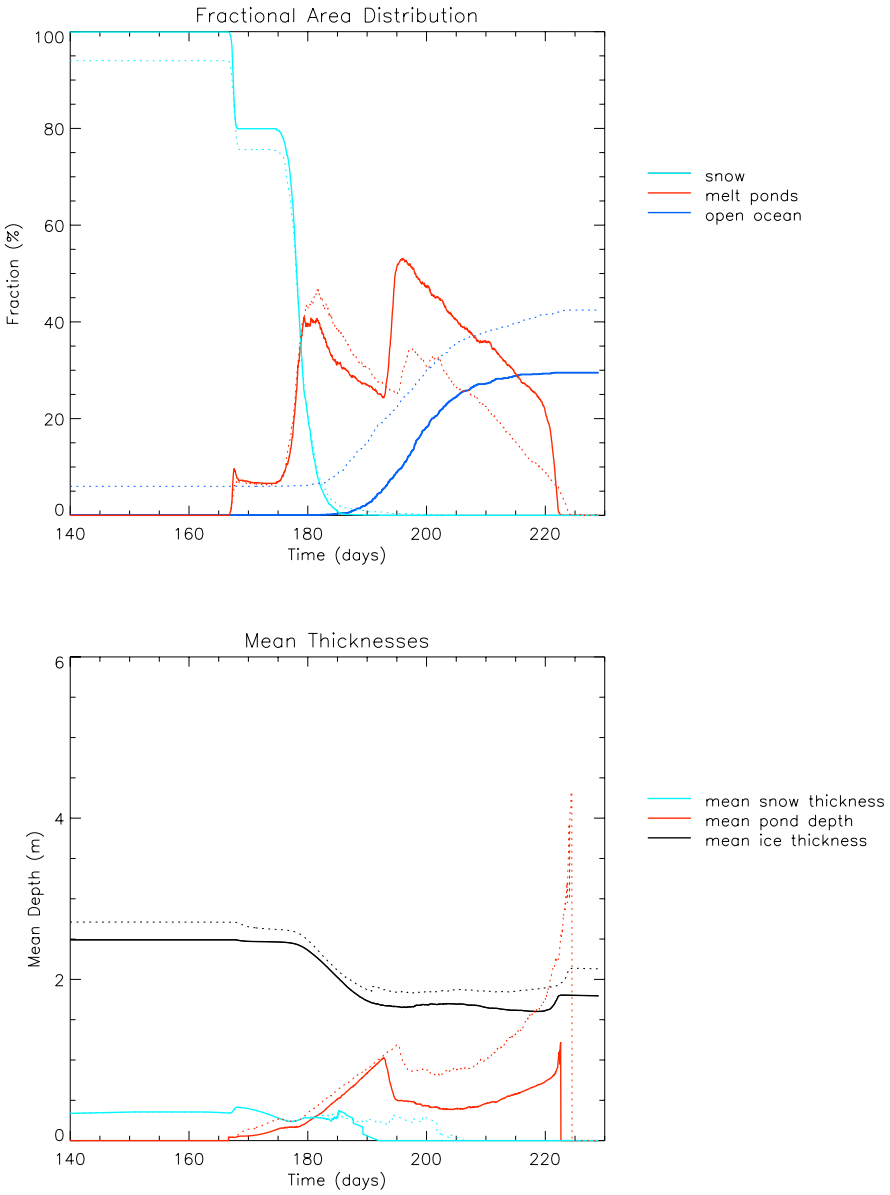

Figure 6.14: Top: Variation in the fractional distribution of surface area with time for the smooth ice case, where mean ice thickness is 2.5 m, standard deviation in ice thickness of 0.5 m, mean snow thickness is 0.30 m and standard deviation in snow thickness is 0.25 m. Fraction of the surface with a snow cover (light blue), fraction of the surface covered with melt ponds (red), fraction of the surface with no ice cover (open ocean) is dark blue. The dashed lines represent the corresponding values for the standard multi-year ice case shown in figure 6.1. Bottom: Change in mean snow depth (light blue), mean pond depth (red) and mean ice thickness (black) with time for the smooth ice case. The dashed lines represent the corresponding values for the standard multi-year ice case shown in figure 5.3.

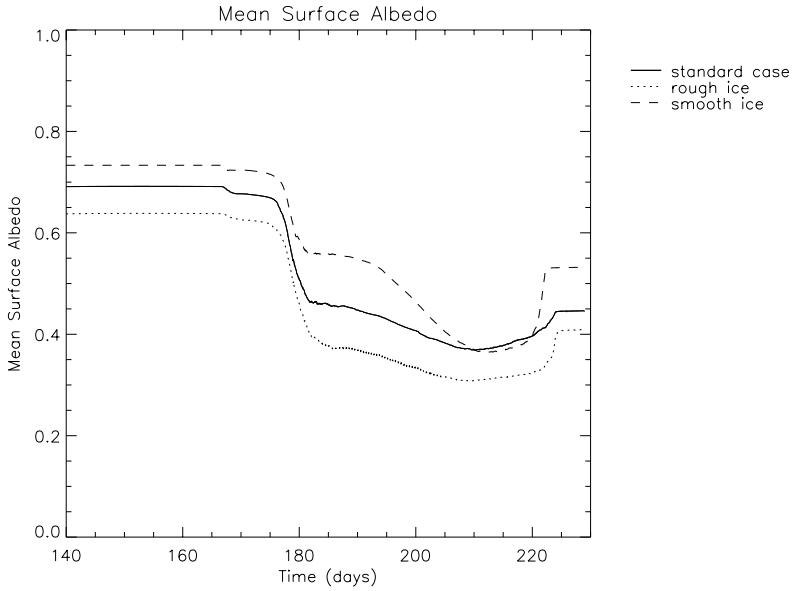

Figure 6.15: Change of aerially averaged surface albedo with time for the standard case and ice sensitivity studies.

6.3.2 Smooth Ice

The mean ice thickness is this case is 2.5 m and the standard deviation is 0.5 m which is the same as the standard deviation in the rough first-year ice case. This ice topography could represent both rough first-year ice and smooth multi-year ice. Fractional area distribution and mean depths are shown in figure 6.14.

Initial ponds form at the same time and pnd fraction is very similar in both the standard case and the smooth ice case. There is a smaller pond fraction after snow has melted in the smooth ice case than in the standard case. This is probably because earlier in the season there are fewer areas below sea level in the smooth ice case. Unlike the standard case where maximum pond fraction occurs after snow cover is removed, in the smooth ice case maximum pond fraction is reached later in the season, on day 196, when pond fraction increases rapidly to its maximum value of 53.1%; this is the same pattern of evolution of pond fraction as in the first-year rough ice case (section 5.3.1).

Mean pond depth is roughly the same in the standard case and in the smooth ice case

until day 192; mean pond depth in the smooth ice case drops and remains below 0.5 m for the much of the rest of the season.

There is a smaller change in mass in the smooth ice case than in the standard case, 51.7% compared to 54.0%, despite mean pond fraction being greater over the season than in the standard case. This is because ponds are shallower on average in the smooth ice case and radiation absorbed depends on pond depth so fewer cells melt through entirely.

Despite the higher pond fraction the surface albedo in the smooth ice case is greater than the standard case for most of the season due to the smaller ocean fraction. Albedo, shown in figure 6.15, is only less than the standard case at the end of the season when the ice surface in the smooth ice case has more ponds than the standard case and the ocean fraction is increasing.

Mean pond area in the smooth ice case, shown in figure 6.13, varies significantly from mean pond area in the standard case. The maximum mean pond area is 254.5 m^2 which is much larger than the maximum mean pond area in the standard case, which is 147.3 m^2. The maximum mean pond area is closer to the first-year ice standard case (219.1 m^2). Evolution of pond area is similar to the first-year ice standard and first-year rough ice cases; mean pond area increases slowly and peaks in the middle of the season before gradually decreasing. In the multi-year ice standard case the pond coverage reaches its maximum earlier in the season.

6.3.3 Summary

Increasing the roughness of the ice caused very little change in pond fraction, although mean pond area was slightly smaller. Reducing the roughness of the surface allowed ponds to spread further across the surface causing larger ponds and a larger pond fraction.

Ponds always form on ice below sea level. Relatively rough ice has a greater surface area below sea level leading to a larger fractional pond area that relatively flat ice. However,

individual ponds tend to be of smaller area on rough ice than on relatively smooth ice. There is some similarity with the multi-year ice smooth case and the first-year ice rough case, which suggests some pattern of pond coverage with surface roughness.

6.4 Sensitivity to Vertical Permeability

For these two simulations standard multi-year ice and snow topographies were used. As in section 5.4, the vertical permeability was reduced from 2.4 $\times 10^{-12}$ m^2 by one order of magnitude to 2.4 $\times 10^{-13}$ m^2 for the low permeability case and increased by one order of magnitude to 2.4 $\times 10^{-11}$ m^2 for the high permeability case. Permeability is difficult to measure and there is much uncertainty about this parameter, Eicken *et al.* (2004). The permeabilities we consider here span the range of observational uncertainty and serve to illustrate the impact of variation in permeability on ice and pond evolution.

6.4.1 Low Permeability

The vertical ice permeability considered here is 2.4 $\times$ 10^{-13} m^2, compared to 2.4 $\times$ 10^{-12} m^2 in the standard case. Fractional area distribution are mean depths are given in figure 6.16.

Pond fraction in the low permeability case increases to its maximum value of 69.1% by day 184, this pond fraction exceeds the standard case value maximum pond fraction. Low permeability reduces the volume of water that drains away and causes increased melting in the ice beneath ponds. Pond fraction remains much larger than the standard case but decreases through the season as the ocean fraction increases. The ocean fraction increases by 57.2% over the season in the low permeability case compared to 42.4% in the standard case. This is due to more ice melting through due to enhanced melt rates beneath ponds.

Mean pond depth in the low permeability case increases through the season and far

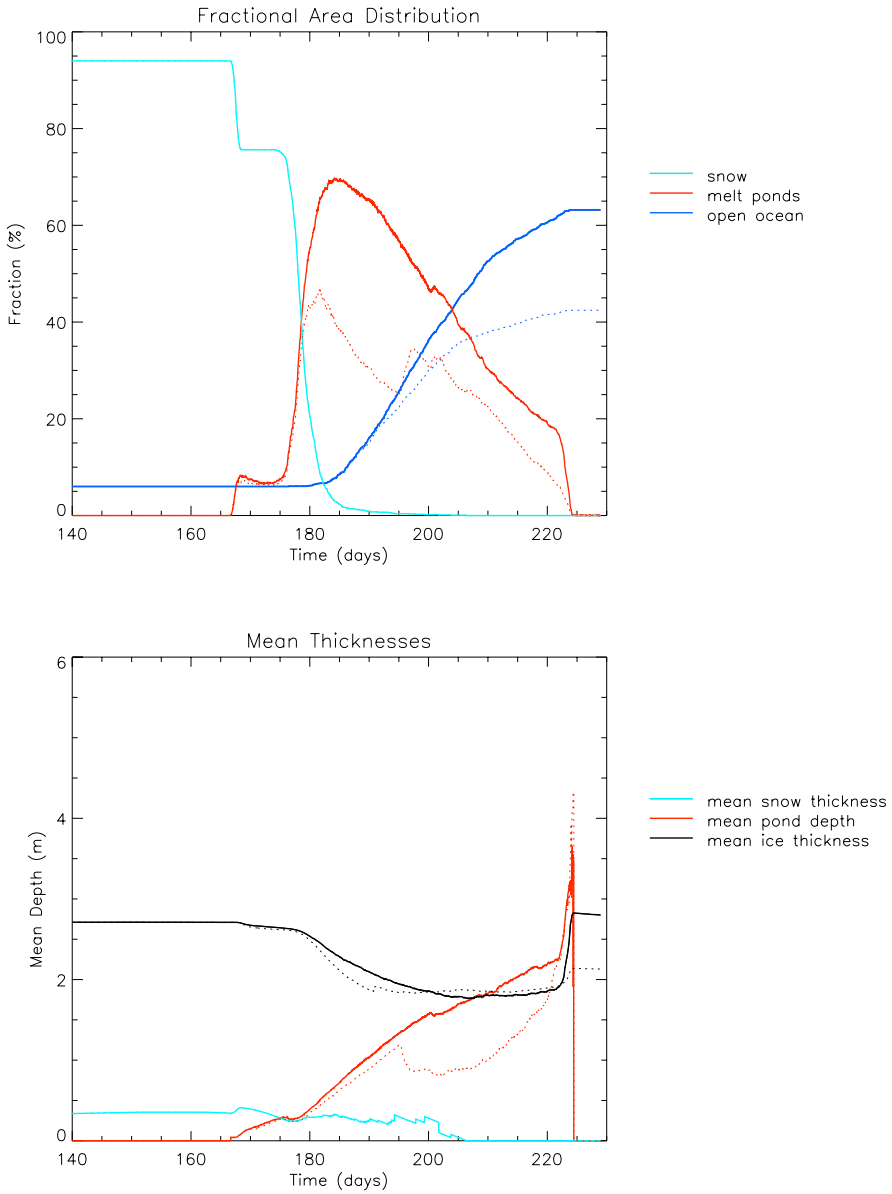

Figure 6.16: Top: Variation in the fractional distribution of surface area with time for the low permeability case, where mean ice thickness is 2.5 m, standard deviation in ice thickness of 1.1 m, mean snow thickness is 0.3 m and standard deviation in snow thickness is 0.25 m. Fraction of the surface with a snow cover (light blue), fraction of the surface covered with melt ponds (red), fraction of the surface with no ice cover (open ocean) is dark blue. The dashed lines represent the corresponding values for the standard multi-year ice case shown in figure 6.1. Bottom: Change in mean snow depth (light blue), mean pond depth (red) and mean ice thickness (black) with time for the low permeability case. The dashed lines represent the corresponding values for the standard multi-year ice case shown in figure 6.1.

exceeds mean pond depth in the standard case. The extra surface water caused a decrease in mass of 61.3% compared to 54.0% in the standard case. This is despite the fact that more water is retained at the surface as ice during freeze up in the low permeability case.

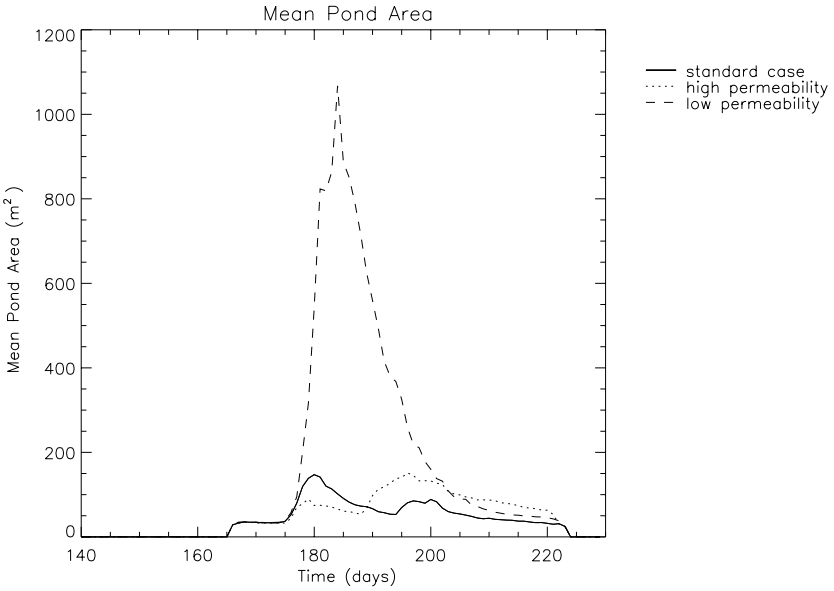

Figure 6.17: Mean individual pond area for the standard case and vertical permeability sensitivity studies.

The low permeability causes the surface to be flooded with water which creates large mean pond area through much of the season. The maximum mean pond area in the low permeability case, shown in figure 6.17, is 1067.3 m^2. The larger pond and ocean fractions cause the average albedo shown in figure 6.18 to be lower during the melt period than in the standard case.

6.4.2 High Permeability

The vertical ice permeability considered here is 2.4×10^{-11} m^2 compared to 2.4×10^{-12} m^2 in the standard case. Fractional area distribution and change in mean depths are shown in figure 6.19.

Ponds drain more rapidly in the high permeability case than in the standard case and the maximum pond fraction reached in the high permeability case is only 31.4% compared

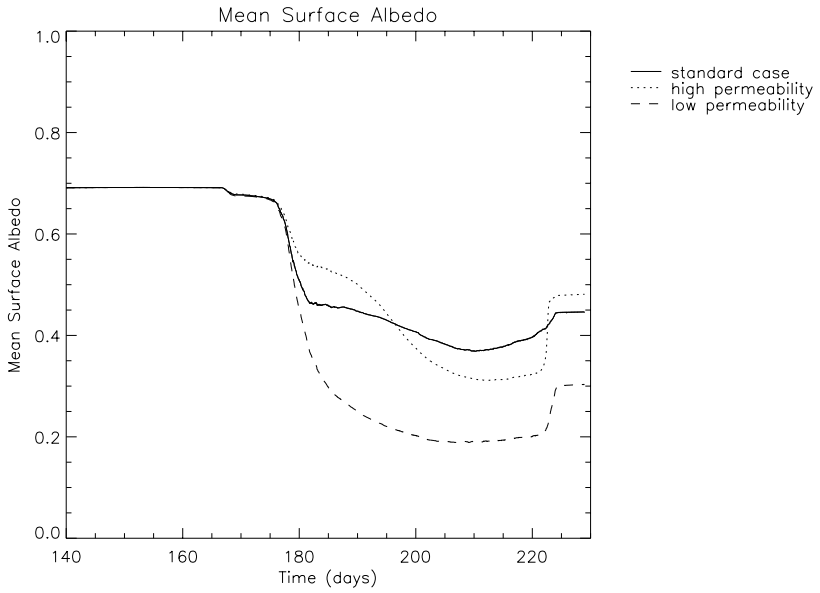

Figure 6.18: Change of aerially averaged surface albedo with time for the standard case and vertical permeability sensitivity studies.

to 47% in the standard case. Pond fraction increases again to a maximum of 42.6% in the high permeability case between day 188 and 192 because melt rates exceed drainage rates. Pond fraction then remains higher than the standard case for the rest of the season.

Despite the higher pond fraction in the second half of the season in the high permeability case, ocean fraction is greater in the standard case. Total increase in ocean fraction over the season is 30.3% compared to 36.4% in the standard case. In fact the higher permeability case has a larger pond covered area than the standard case because more ice melts through completely in the standard case, both decreasing the mean pond area on the remaining ice and providing a sink of surface water. Total ablation, however, is very similar, 1.34 m in the high permeability case compared to 1.32 m in the standard case.

Mean pond depth is the same as the standard case until day 189, after that pond depth in the high permeability case is reduced and remains below 1 m until day 212.

Mean pond area, shown in figure 6.17 reaches a maximum of 151.4 m^2, which is larger than the maximum mean pond area in the standard case. This is due to ponds forming

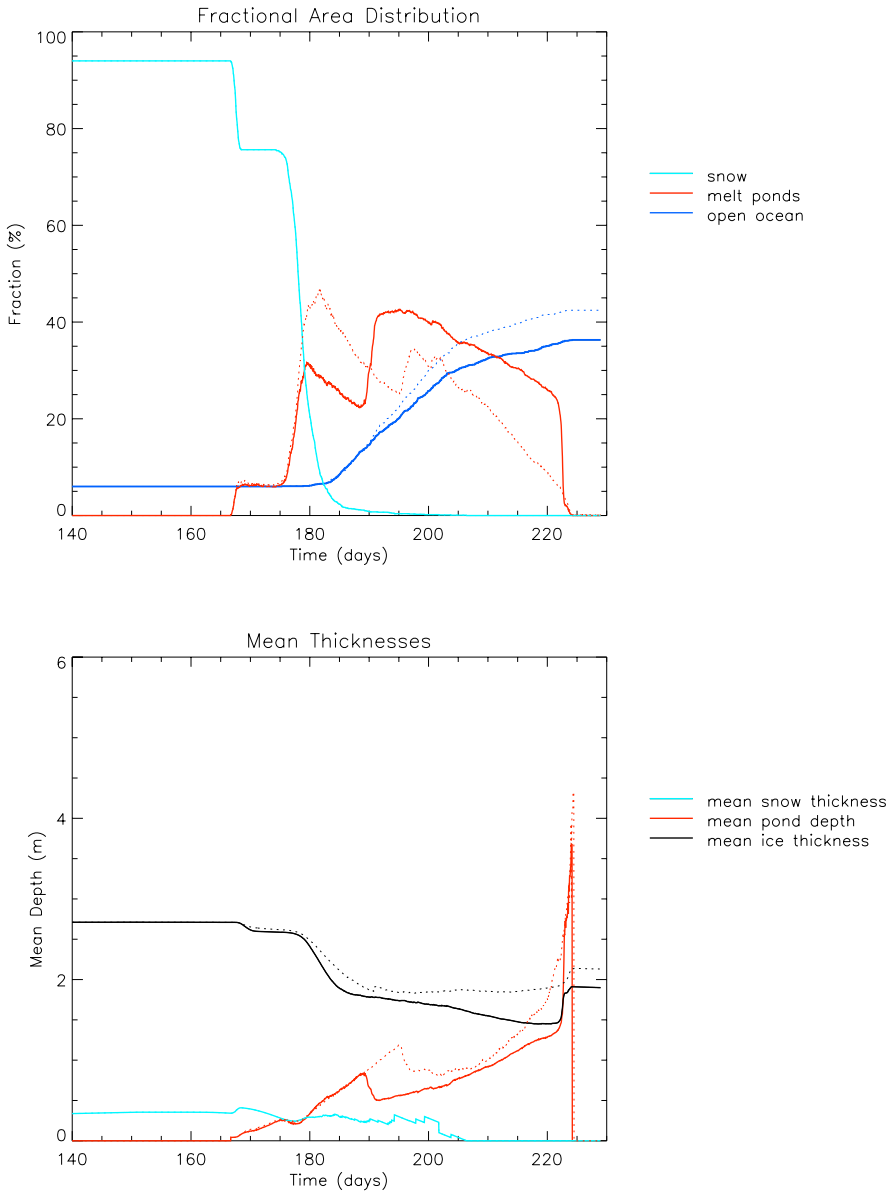

Figure 6.19: Top: Variation in the fractional distribution of surface area with time for the high permeability case, where mean ice thickness is 2.5 m, standard deviation in ice thickness of 1.1 m, mean snow thickness is 0.31 m and standard deviation in snow thickness is 0.25 m. Fraction of the surface with a snow cover (light blue), fraction of the surface covered with melt ponds (red), fraction of the surface with no ice cover (open ocean) is dark blue. The dashed lines represent the corresponding values for the standard multi-year ice case shown in figure 5.3. Bottom: Change in mean snow depth (light blue), mean pond depth (red) and mean ice thickness (black) with time for the high permeability case. The dashed lines represent the corresponding values for the standard multi-year ice case shown in figure 6.1.

in the high permeability case on ice cells that have melted through in the standard case. Early in the season mean pond area is less than mean pond area in the standard case, after day 188 mean pond area is greater than mean pond area in the standard case. Most of the ponds have a surface height at or below sea level and therefore permeability has no effect.

6.4.3 Summary

Reducing the vertical permeability reduces the vertical drainage through the ice and increases the fraction of the surface covered in ponds. Ponds can have a positive hydraulic head in this case. Increasing the permeability causes more drainage through the ice, the reduction in pond fraction is limited, however, by the roughness of the ice surface. Most of the ponds form in regions well below sea level and, as these ponds do not drain below sea level, the higher permeability has no effect.

6.5 Summary

In this chapter the results of simulations of melt ponds on multi-year ice were presented. The main results are summarised in table 6.1 The standard case was initialised with ice and snow topography models that represent conditions found in multi-year ice. In comparison with the first-year ice standard case, mean pond depth in the multi-year ice case was greater, snow cover took longer to be removed completely, ocean fraction at the end of the simulation was smaller, and mean pond area was consistently smaller.

The results of the sensitivity studies showed that multi-year ice evolution was less sensitive to changes in ice and snow topography than first-year ice. As with the first-year ice sensitivity studies changing the roughness of the snow had the least impact on pond fraction and ice ablation. Thick snow cover increased the combined snow and ice

ablation but reduced the total ice ablation, maximum pond fraction and minimum albedo were virtually unchanged. Thin snow resulted in a small reduction in the maximum pond fraction and also a small reduction is the minimum albedo. Reducing the roughness of the ice produced an increase in maximum pond fraction and a reduction in ice and snow ablation. The conditions here could also be considered to represent rough first-year ice. Increasing ice roughness from the standard case caused an increase in ice ablation and an increase in pond depth and also a lower minimum ice albedo although maximum pond fraction was the same.

Maximum pond fraction and minimum albedo were found to be most sensitive to a reduction in vertical ice permeability. Reducing vertical ice permeability by one order of magnitude caused maximum pond fraction to increase to 70%, compared to 47% in the standard case and minimum albedo to decrease to 0.19 compared to 0.37 in the standard case and ablation increases compared to the standard case. Increasing the vertical ice permeability by one order of magnitude caused maximum pond fraction to be reduced from 47% in the standard case to 43% , however ice and snow ablation remained similar in the high permeability and standard cases.

In conclusion, although multi-year ice evolution was found to be relatively insensitive to changes in snow roughness and snow thickness, there was some sensitivity to changes in ice thickness. Multi-year ice evolution was found to be most sensitive to changes in vertical ice permeability.

In the following chapter the standard case multi-year ice simulation and the standard case first-year ice simulation, described in the previous chapter, will be compared with observational data and other model results.

Model Run	Mean Ice Thickness (Standard Deviation) (m)	Mean Snow Thickness (Standard Deviation) (m)	Ice Ablation (m)	Ice and Snow Ablation (m)	Max. Pond Depth (m)	Max. Pond Fraction -	Min. Area Averaged Albedo -	Change in Ocean Fraction -
Standard Case	2.50 (1.10)	0.30 (0.25)	1.41	1.74	4.35	0.47	0.37	0.36
Rough Snow	2.50 (1.10)	0.30 (0.40)	1.41	1.81	4.35	0.46	0.36	0.38
Smooth Snow	2.50 (1.10)	0.30 (0.10)	1.39	1.68	3.93	0.49	0.36	0.33
Thick Snow	2.50 (1.10)	0.60 (0.25)	1.37	1.98	4.26	0.48	0.38	0.37
Thin Snow	2.50 (1.10)	0.20 (0.25)	1.42	1.68	4.37	0.45	0.34	0.35
Smooth Ice	2.50 (0.50)	0.30 (0.25)	1.23	1.82	2.87	0.53	0.36	0.30
Rough Ice	2.50 (1.50)	0.30 (0.25)	1.67	1.73	5.79	0.47	0.31	0.33
Low Permeability	2.50 (1.10)	0.30 (0.25)	1.61	1.95	4.59	0.70	0.19	0.57
High Permeability	2.50 (1.10)	0.30 (0.25)	1.42	1.76	4.14	0.43	0.31	0.30

Table 6.1: Summary of important results from the standard multi-year ice case and sensitivity studies.

Chapter 7

Comparison of Simulations with Other Models and Observations

This chapter compares the standard case first-year ice and multi-year ice model results described in chapter 5 and chapter 6 with the results of some of the melt-pond–sea-ice models introduced in chapter 2 and with melt pond observations. The melt-pond–sea-ice model developed in this thesis combines the one-dimensional thermodynamic model of Taylor & Feltham (2004) with the cellular automaton design of Lüthje *et al.* (2006), but with a more realistic treatment of hydraulic processes. The Taylor & Feltham (2004) model is used in its original form to model the vertical evolution of ice and snow depth in the melt-pond–sea-ice model described in this thesis and therefore performs in the same manner as described in Taylor & Feltham (2004). The Ebert *et al.* (1995) model prescribes pond fraction and therefore does not model the evolution of pond fraction, hence there is no benefit in comparison of the model described in this thesis with the Ebert *et al.* (1995) model. Since the model described in this thesis uses the same cellular automaton design as the Lüthje *et al.* (2006) model comparisons will be made between the Lüthje *et al.* (2006) model and the model presented in this thesis. The model described in this thesis will also

be compared to the Flocco & Feltham (2007) model, which, although it represents a much larger scale of sea ice still models the fraction of the ice surface covered in melt ponds.

Comparisons with the Lüthje *et al.* (2006) model and the Flocco & Feltham (2007) model are made in sections 7.1 and 7.2. Whilst there were some similarities in the model results of the Lüthje *et al.* (2006) model and the model described in this thesis, such as first-year ice in both cases having larger, shallower ponds than multi-year ice the mean pond area, pond depth and pond fraction differed, despite the models using similar initial conditions. Total ablation in both the Lüthje *et al.* (2006) and Flocco & Feltham (2007) models, which use a simple scheme to model melting, was smaller than total ablation in the model described in this thesis. The differences between the Lüthje *et al.* (2006) and Flocco & Feltham (2007) model results compared with the model presented in this thesis and the summary in section 7.3 demonstrate the impact of the more sophisticated physical descriptions included here.

Comparison with observations are made in section 7.4. Model results show good agreement with observations with duration of pond coverage, pond area and ice ablation comparing well for both the first-year ice and multi-year ice cases. Modelled pond fraction in the multi-year ice case was higher than some observed pond fractions but compared well with level multi-year ice observations made by Eicken *et al.* (2002).

7.1 Comparison with Lüthje *et al.* (2006) Model

The Lüthje *et al.* (2006) model which is summarised in section 2.4 is a cellular automaton model that represents a 125 m $\times$ 125 m section of a sea ice floe, the model simulates the horizontal evolution of melt ponds across the sea ice surface. Ice and snow melt rates are fixed and no differentiation is made between them. Vertical drainage rate is constant. The model described in this thesis uses the same cellular automaton design as Lüthje *et al.*

(2006) but a number of improvements and additions have been to model the evolution of the melt pond cover more realistically (see Chapter 3 and Chapter 4). The major improvements of the model described in this thesis compared to the Lüthje *et al.* (2006) model are the initial surface topographies, the representation of sea level and vertical drainage, and the method for calculating ice melt.

The initial ice and snow surface topographies in the model described in this thesis are stochastically generated based on observed statistical characteristics of sea ice. Ice surface and base heights are generated separately leading to a surface topography with some ice surface heights below sea level initially. The initial surface topography in the Lüthje *et al.* (2006) model is based on ice freeboard measurements, ice thickness is calculated assuming cell-wise hydrostatic equilibrium, and therefore all cells have positive initial freeboard.

In the model described in this thesis the entire floe is in hydrostatic equilibrium, but not necessarily every cell, and sea level with respect to the floe is recalculated every time step. This allows vertical drainage to be realistically modelled using Darcy's Law in the model described in this thesis, rather than take place at a fixed rate as in the Lüthje *et al.* (2006) model. Horizontal water transport rates in the model described in this thesis vary from cell to cell depending on the solid fraction in the ice. Therefore in the model described in this thesis there is spatial as well as temporal variation in drainage rate.

In the model described in this thesis ice and snow melt rates are dependent on the temperature of the ice which is determined from external modelled atmospheric conditions. In the Lüthje *et al.* (2006) model bare ice melts at a fixed rate and melting beneath ponds take place at an enhanced rate using an ad hoc algorithm motivated by observations. There is no basal melting in the Lüthje *et al.* (2006) model and there is no separate representation of snow cover.

The Lüthje *et al.* (2006) model simulates a 50 day melt season which begins when ponds

initially form, supposedly in early June. The model described in this thesis simulates a 90 day season that begins before melting starts on day 140 (May 20), this date was chosen so that mean ice and snow thicknesses before melting begins, for which more data exists, could be used to initialise the model. Ponds form initially 27 days after this date, the model is run for a for longer period at the end of the melt season so that freeze up is also simulated, this is not possible in the Lüthje *et al.* (2006) model. However the duration of melting in both models is very similar. Whereas in the Lüthje *et al.* (2006) model melting takes place continually at a fixed rate, the improvements to the model described in this thesis mean that melting takes place at a rate which is determined by the surface heat budget temperature profile in the ice and pond temperature (when present).

The mean values of three simulations with different initial first-year ice or multi-year ice surface topographies described in Lüthje *et al.* (2006) are here compared to the standard case first-year ice and multi-year ice runs that have been described in chapters 5 and 6.

7.1.1 First-Year Ice

The standard deviation in ice thickness in first-year ice simulations in the Lüthje *et al.* (2006) model is 0.2 m which is the same as the standard deviation of ice topography in the standard first-year ice case described in this thesis. The mean ice thickness of 1.05 m in the Lüthje *et al.* (2006) first-year ice case is smaller than the mean ice thickness of 1.7 m in the first-year ice standard case described in this thesis. The initial topographies therefore have similar characteristics although there are likely to be bigger hydraulic gradients between cells in the first-year ice model described in this thesis due to the greater mean thickness and the initial positioning of ice surface height with respect to sea level.

In the Lüthje *et al.* (2006) model melt rates and drainage rates have been chosen through sensitivity studies rather than being established from ice temperature and hydraulic head as in the model described in this thesis. The result of this is that the

maximum pond fraction of 81% in the Lüthje *et al.* (2006) model is almost double the maximum pond fraction of 48% in the first-year ice case of the model described in this thesis. The mean fraction of ponded ice over the entire season is more similar: 41% in the Lüthje *et al.* (2006) model compared to 32% in the first-year ice case described in this thesis.

In the Lüthje *et al.* (2006) model pond fraction increases to its maximum value shortly after initial pond formation. Pond fraction then decreases continually to approximately 14% by 30 days into the season. There is much less variability in pond fraction over the season in the first-year ice standard case described in this thesis, see figure 5.3. There is a local maxima due to snow cover being removed and a later maximum pond fraction as melt rate increases. Pond fraction across the entire domain does not drop below 27% and ponded ice fraction does not drop below 35% until ponds begin to freeze over. The smaller variability in the first-year ice standard case described in this thesis is the reason for the similar mean pond fractions between the Lüthje *et al.* (2006) model and the model described in this thesis.

Figure 7.1 shows contour plots of the surface covered in ponds in the Lüthje *et al.* (2006) model. Melt water floods the surface by day 20 and after this ponds are all roughly the same depth throughout, ponds disappear as ice melts through and the ocean fraction increases. This can be compared to figure 5.2 which shows contour plots of the surface covered in ponds in the first-year ice case described in this thesis. There are differences in pond area and pond depth that are described below.

Mean pond area in the Lüthje *et al.* (2006) first-year ice standard case (shown in figure 7.2) is much larger than the mean pond area in the first-year ice standard case described in this thesis. Mean pond area increases to a maximum over the first 20 days of the melt season and remains between 2500 m^2 and 3500 m^2 for the rest of the 50 day season. The

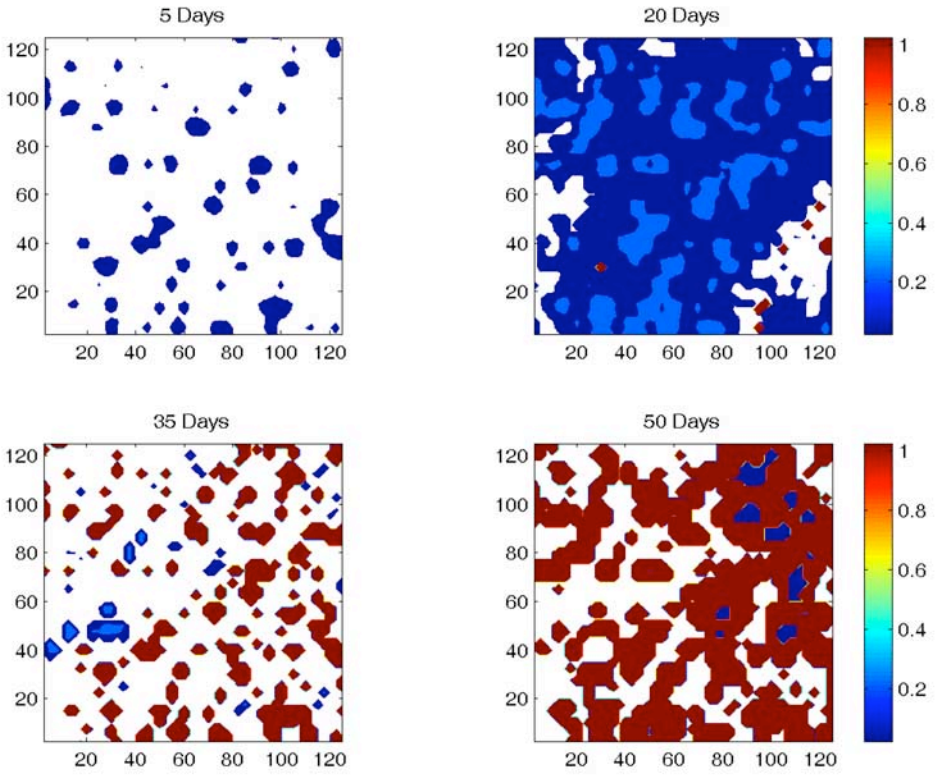

Figure 7.1: Contour plots of the evolution of pond area and depth on first-year ice after 5 days, 20 days, 35 days and 50 days, taken from Lüthje *et al.* (2006). Axis labels are in metres. The scale on the right represents pond depth, shallow ponds are blue and deep ponds are red. White represents bare ice and dark red represents regions where ice has melted through and bare ice is exposed.

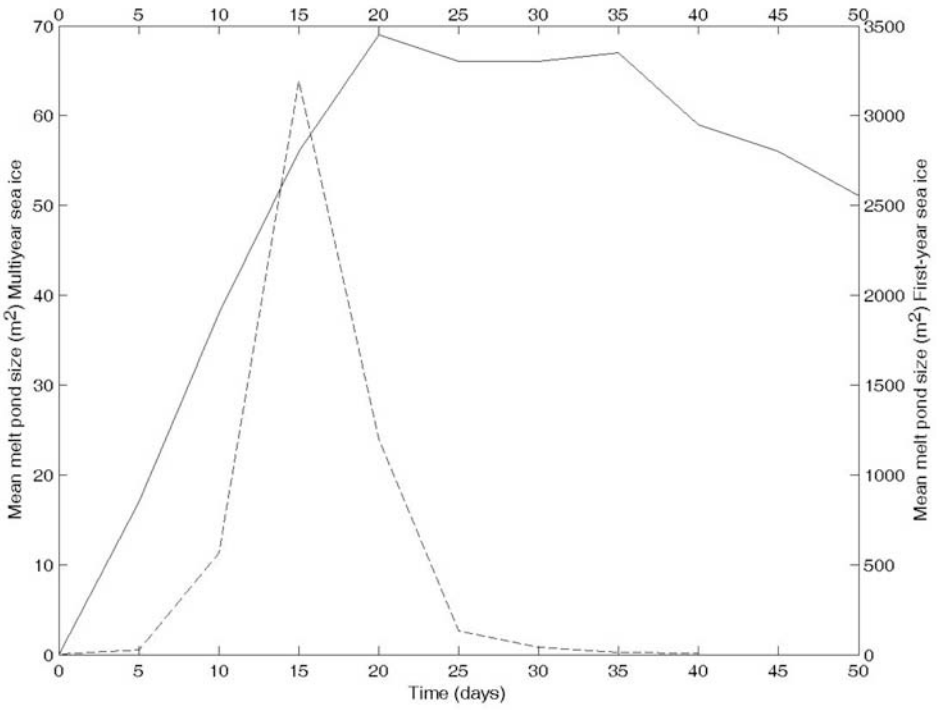

Figure 7.2: Evolution of mean melt pond area from the Lüthje *et al.* (2006) model for first-year ice, dashed line (scale on the right-hand side) and multi-year ice, solid line (scale on the left-hand side). Taken from Lüthje *et al.* (2006)

large mean pond area is due to the surface being flooded with one large pond when the pond fraction is at its maximum which gradually drains away. This pattern of evolution is not observed in pond area in the first-year ice standard case described in this thesis. In the first-year ice standard case described in this thesis mean pond area increases to its maximum of 219 m^2 in the middle of the season and decreases over the second half of the season. Initial flooding, due to snow melting covers a much smaller area of the surface. Ponds form in the lowest cells and depth and area increases with time.

The mean pond depth (average mean pond depth over the period when more than one pond was present) in the first-year ice case described in this thesis is 0.6 m compared to 0.17 m in the Lüthje *et al.* (2006) model, both these mean pond depths are reasonable and within the range of observed values. There is more variation in pond depth in the model described in this thesis. Pond depth in the first-year ice case described in this thesis

appears to be more driven by topography than the Lüthje *et al.* (2006) model.

There is no basal melting in the Lüthje *et al.* (2006) and since there is no separate snow cover the total ablation value includes ice and snow. The total ablation in the Lüthje *et al.* (2006) model is 0.75 m which is much lower than the mean ice ablation of 1.26 m measured by Perovich *et al.* (2003). The combined ice and snow ablation in the first-year ice case described in this thesis is 1.33 m which is closer to the values measured by Perovich *et al.* (2003). The low ablation of Lüthje *et al.* (2006) is probably due to the simple algorithm used to calculate the volume of melting, and the small, 1.05 m, initial average ice thickness which, since the majority of cells to melted through entirely, limited the total ablation by reducing the total volume of ice. In the model described in this thesis the initial ice thickness was greater and the final ocean fraction was smaller.

7.1.2 Multi-Year Ice

The multi-year ice standard cases in the Lüthje *et al.* (2006) model and the multi-year ice standard case described in this thesis again had similarities in the initial ice topography. Standard deviation in ice thickness is 1.2 m in the multi-year ice standard case described in this thesis and 1.5 m in the Lüthje *et al.* (2006) mean multi-year ice standard case. The case described in this thesis has an additional snow layer which has a mean thickness of 0.3 m and standard deviation of 0.25 m. Mean ice thickness is much greater than in the Lüthje *et al.* (2006) standard case, 3.67 m compared to 2.5 m in the case described in this thesis. The maximum pond fraction of 45% in the Lüthje *et al.* (2006) model compared closely to 47% in the multi-year ice case described in this thesis. The mean pond fraction over the season is 34% in the Lüthje *et al.* (2006) model, which is similar to the 32% in the multi-year ice standard case described in this thesis.

Figure 7.3, which compares a multi-year ice standard case from the model described in this thesis and the Lüthje *et al.* (2006) model runs to observations of melt pond fraction,

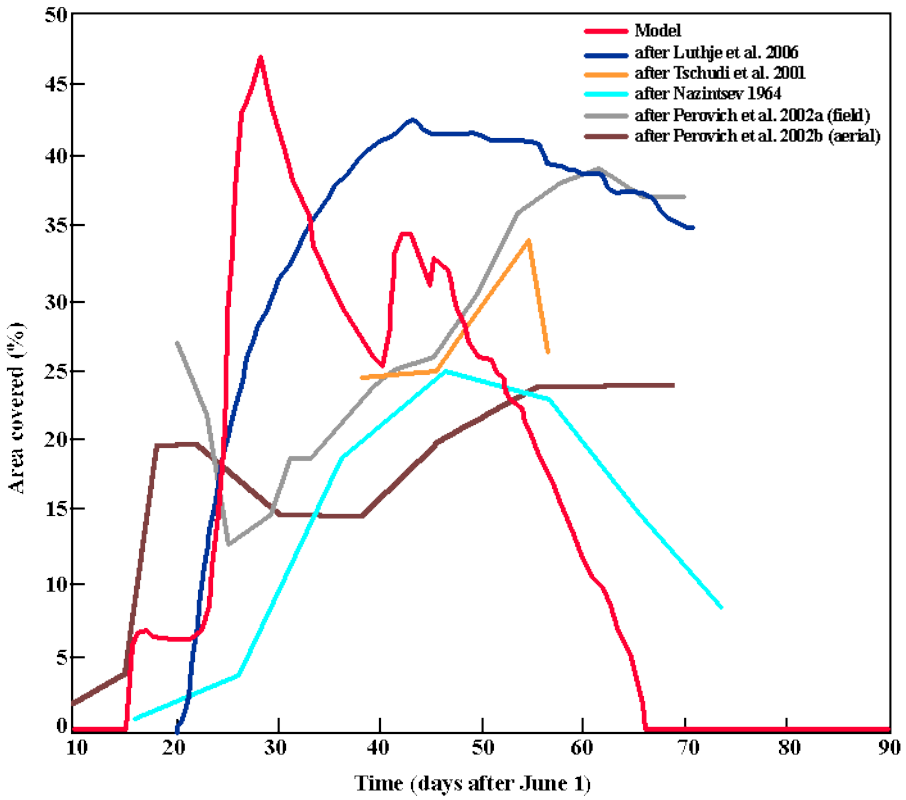

Figure 7.3: Area covered with melt ponds from the the multi-year ice standard case described in this thesis, Lüthje *et al.* (2006) multi-year ice model and field studies.

shows that there is a great deal of variability in pond fraction over time and location where measurements are taken, particularly at the start and end of the season. The model results shown in the figure 7.3 by Lüthje *et al.* (2006) overestimates observed results in the central part of the season, whereas the multi-year ice standard case presented in this thesis overestimated pond fraction at the start of the season but compares better to the field studies than the Lüthje *et al.* (2006) model in the latter half of the season.

Pond formation occurs on approximately the same date in both models, pond fraction increases rapidly to a similar maximum value in both cases. In the case described in this thesis the increase in pond fraction is due to melting snow, whereas in the Lüthje *et al.* (2006) model the increase is due to the fixed melting rate. Pond fraction decreases slowly for the rest of the season in the Lüthje *et al.* (2006) model, in the case described in this thesis pond fraction decreases more rapidly. Due to the increased variation in ice thickness compared to the first-year ice cases, in both the Lüthje *et al.* (2006) model and the model described in this thesis there is more variation in pond depth in the multi-year ice cases than the first year ice cases. Ponds form in the lowest cells and widen and deepen as the season progresses, for the Lüthje *et al.* (2006) model this is shown in figure 7.4, this can be compared to figure 6.3 for the standard multi-year ice case described in this thesis. Due to the thicker ice in both multi-year ice cases compared to first-year ice cases fewer ice cells melt through.

The combined ice and snow ablation in the multi-year ice standard case described in this thesis is 1.74 m, in the Lüthje *et al.* (2006) the total ablation is 0.91 m, which is too low for multi-year ice total ablation, given that the SHEBA study measured a combined first-year and multi-year ice ablation of 1.26 m, Perovich *et al.* (2003). The low total ablation value is probably due to a combination of the fixed drainage rate and fixed melt rate used in the Lüthje *et al.* (2006) model. The large surface areas covered with ponds

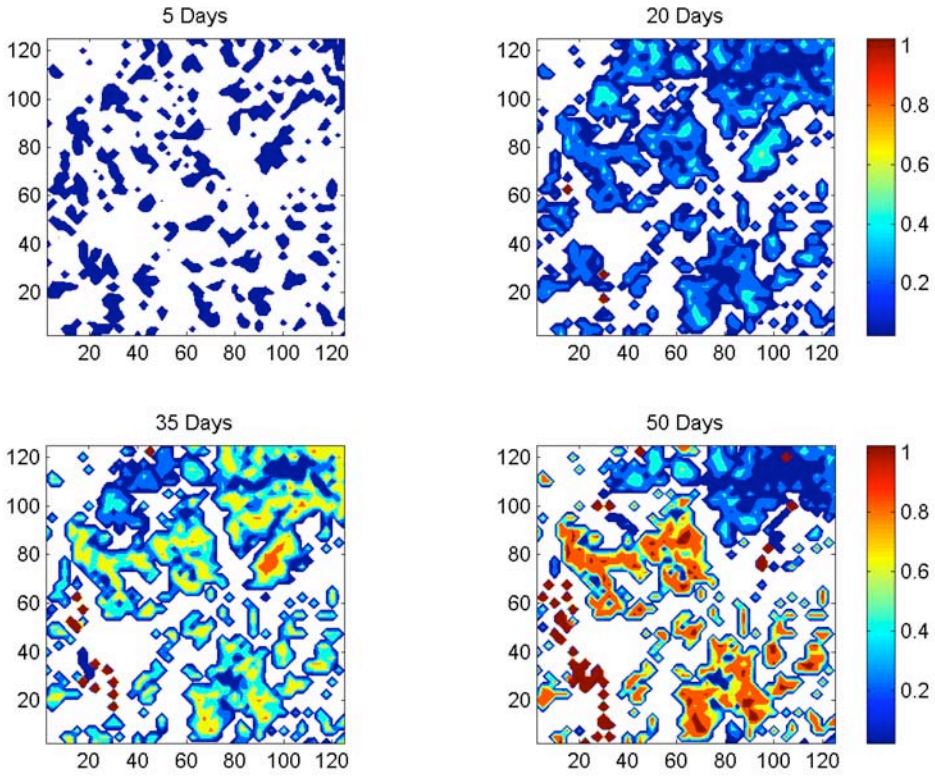

Figure 7.4: Contour plots of the evolution of pond area and depth on multi-year ice after 5 days, 20 days, 35 days and 50 days, taken from Lüthje *et al.* (2006). Axis labels are in metres. The scale on the right represents pond depth, shallow ponds are blue and deep ponds are red. White represents bare ice and dark red represents regions where ice has melted through and bare ice is exposed.

suggest that the drainage rate is too low, but the low total ablation despite this suggests that the melt rate is low, this is also seen in the Flocco & Feltham (2007) results which are described in the next section. Total ablation has been improved in the model described in this thesis by calculating heat flux through the ice. Mean pond depth in the Lüthje *et al.* (2006) multi-year ice case is 0.57 m compared to 0.85 m in the multi-year ice case described in this thesis. The initial mean ice thickness in the Lüthje *et al.* (2006) model was greater than in the model described in this thesis, therefore it is expected that there are larger gradients between freeboard heights than in the model described in this thesis. However the topography model used in this thesis (chapter 4) allows ice cells to have a surface below sea level which could have enabled deeper mean pond depth when combined with the enhanced melt rate beneath ponds.

Maximum mean pond area is 147 m^2 in the multi-year ice case described in this thesis and 70 m^2 in the Lüthje *et al.* (2006) model, shown in figure 7.2. There is more variability in mean pond size in the model described in this thesis, although in both models mean pond size varies with time more than in the first-year ice cases. The large maximum mean pond size in the multi-year ice model described in this thesis corresponds to snow melting, which is not modelled separately by Lüthje *et al.* (2006). Mean pond area then decreases to below 90 m^2. Both models produce mean pond sizes that are reasonable; mean pond size is again driven by ice topography and snow cover.

7.2 Comparison with Flocco & Feltham (2007) Model

The model described in Flocco & Feltham (2007) is intended to be included in a global climate model, therefore a major difference between the Flocco & Feltham (2007) model and the model described in this thesis is the horizontal scale represented. The Flocco & Feltham (2007) model represents a grid cell in a global climate model, this represents a

surface area of approximately 40 $\times 10^9$ m^2 compared to 4 $\times 10^4$ m^2 in the model described in this thesis. In the Flocco & Feltham (2007) model, ice types are modelled by altering the ice thickness distribution, so first-year ice is represented by having the majority of the ice in thinner ice thickness categories. Surface topography, such as the ice surface topography described in this thesis, is not modelled. As topography cannot be modelled in the Flocco & Feltham (2007) model horizontal water transport is modelled by distributing the volume of melt water such that the lower surface height categories are covered first. Melting is modelled using the same algorithm as the Lüthje *et al.* (2006) model, whereas the model described in this thesis uses the distribution of temperature within the ice to establish melt rate. There are some similarities between the Flocco & Feltham (2007) model and the model described in this thesis: both include a separate snow cover topography, vertical drainage is governed by Darcy's Law, sea level with respect to the sea ice cover is modelled and both surface and basal melting are modelled. As explained in section 7.1 for the Lüthje *et al.* (2006) model, since the Flocco & Feltham (2007) model uses fixed melt rates whereas the model described in this thesis is initialised with pre melting conditions, the models can be compared over the period when melt begins until freeze up which is approximately the same duration in both models.

7.2.1 First-Year Ice

Flocco & Feltham (2007) present a sensitivity study in which the ice thickness distribution is altered from the standard case to represent first-year ice. This first-year ice sensitivity study gives a maximum pond fraction of 66% compared to 49% in the standard first-year ice case described in this thesis. Evolution of pond fraction, shown for the Flocco & Feltham (2007) first-year ice case in figure 7.5, does not compare well to the evolution of pond fraction in the first-year ice standard case described in this thesis. Despite initial ponds forming from snow melt the initial pond fraction is low and the maximum pond

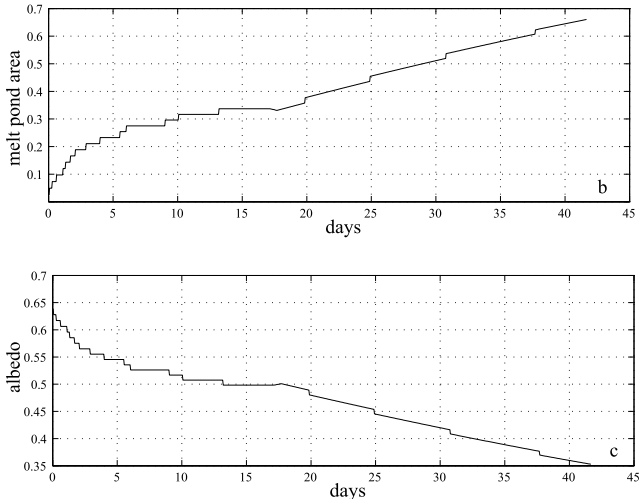

Figure 7.5: Results from the Flocco & Feltham (2007) first-year ice simulation. Area covered in melt ponds (top) and area-averaged albedo (bottom). Taken from Flocco & Feltham (2007).

fraction is not reached until the end of the season. In the first-year ice case described in this thesis maximum pond fraction is reached in the middle of the season and then decreases.

Maximum mean pond depth is 0.91 m in the standard first-year ice case described in this thesis when calculated before the ocean fraction increases rapidly at the end of the season and most ponds drain, this compares well with the Flocco & Feltham (2007) model where maximum pond depth is 0.90 m. The similarity in mean pond depth is probably due to a similar range in ice thickness in the model and the same vertical drainage scheme in both models allowing ponds to drain to sea level. The ice ablation in the first-year ice standard case is 1.01 m compared to 0.55 m in the Flocco & Feltham (2007) first-year ice study, the difference in ablation is expected because the bare ice melt rate is fixed in the Flocco & Feltham (2007) model.

The minimum average ice albedo for the first-year ice standard case described in this thesis of 0.46 is greater than the minimum average albedo of 0.35 in the Flocco & Feltham (2007) first-year ice case, shown in figure 7.5. This is due to the greater maximum pond

fraction in the Flocco & Feltham (2007) first-year ice case. The standard case Flocco & Feltham (2007) results are more similar to the first-year ice standard case described in this thesis. The minimum albedo in the Flocco & Feltham (2007) standard cases is 0.44 and maximum surface coverage of 46% which is close to 49% in the first-year ice case described in this thesis. The pattern of change of albedo compares well to the change in albedo during the period of melting in the first-year ice standard case described in this thesis.

7.2.2 Multi-Year Ice

In the multi-year ice sensitivity study the maximum pond covered area is 43% in the Flocco & Feltham (2007) model compared to a slightly greater maximum pond covered area of 47.1% in the standard multi-year ice case described in this thesis. The model described in this thesis had a maximum pond fraction early in the season due to snow melting, pond fraction then decreased with time. The Flocco & Feltham (2007) model pond fraction, shown in figure 7.6, had the opposite trend: pond fraction increases with time and reaches its maximum value at the end of the season. The generally observed surface flooding at the start of the season is not recreated by the Flocco & Feltham (2007) model. As surface albedo is directly linked to pond fraction in the Flocco & Feltham (2007) model it is possible that these differences could cause surface albedo and melt rates to be inaccurate for much of the season. Both the Flocco & Feltham (2007) model and the model described in this thesis give maximum pond fractions at the upper end of the range of observations (discussed in the following section).

The total ice ablation is 1.41 m in the model described in this thesis which is much greater than the total ablation of 0.56 m in the Flocco & Feltham (2007) model multi-year ice case. The difference in ablation, despite a similar maximum pond fraction, could be due to the maximum pond fraction occurring at the start of the season in the model

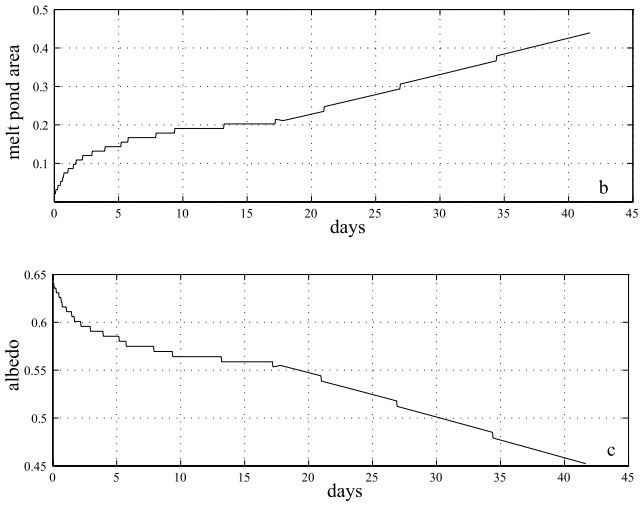

Figure 7.6: Results from the Flocco & Feltham (2007) multi-year ice simulation. Area covered in melt ponds (top) and area-averaged albedo (bottom). Taken from Flocco & Feltham (2007).

described in this thesis, leading to more enhanced melting with time. However the fixed melt rate algorithm also resulted in low ablation rates in the Lüthje *et al.* (2006) model as well, where evolution of pond fraction with time was similar to the case described in this thesis.

The minimum ice albedo of the multi-year standard case described in this thesis is 0.49 which is greater than the albedo of 0.46 in the multi-year ice results from Flocco & Feltham (2007), despite the maximum pond fraction being greater in the multi-year ice case described in this thesis. The minimum albedo in the multi-year ice case described in this thesis occurs early in the season on day 183, when pond fraction is at its maximum. Minimum surface albedo in the Flocco & Feltham (2007) model appears at the end of the season also when pond fraction is at its maximum. In the Flocco & Feltham (2007) model surface albedo is calculated directly from pond fraction using a linear weighted sum $\alpha = \alpha_{bareice}(1 - A_{pond}) + A_{pond}\alpha_{pond}$ whereas in the model described in this thesis surface albedo is calculated in every cell and then averaged over all the ice cells to give the average ice surface albedo. The albedo in each cell is dependent on the optical properties of the ice

which vary with pond depth, the difference in calculation could account for the difference in albedo.

7.3 Summary

There were some similarities in the pattern of pond coverage between the Lüthje *et al.* (2006) model and the model described in this thesis: in both models first-year ice had larger, shallower ponds than multi-year ice and there was more ablation on multi-year ice. However the differences between the model results highlight the importance of modelling both drainage and ice topography as accurately as possible. Despite having similar initial ice surface roughness in the Lüthje *et al.* (2006) model and the model described in this thesis, pond fraction, mean pond area and pond depth were often very different, particularly in the first-year ice comparison. The inclusion of a sea level calculation and modelling vertical drainage by Darcy's law made a substantial difference to pond fraction, particularly in the first-year ice case. The total ablation in the Lüthje *et al.* (2006) model and the Flocco & Feltham (2007) model was much less than the total ablation in the model described in this thesis which demonstrates the improvement made by modelling the thermodynamic processes within the ice using the Taylor & Feltham (2004) model.

7.4 Comparison of Model Results to Observations

In this section the first-year ice and multi-year ice standard cases are compared to observations. In the model described in this thesis both the first-year ice standard case and the multi-year ice standard case initial ponds form on day 167 and, within a few days, much of the ice surface is covered in ponds. There is typically substantial variation between observations of melt ponds since observations are typically made at different points in the melt season and at different locations. However, El Naggar *et al.* (1998) also observed

initial pond formation at this time and Perovich *et al.* (2002) observed 2% of the surface covered in ponds on day 162 and widespread pond coverage by day 174. These observations compare well to both the multi-year and first-year ice cases described in this thesis. The model is initialised with air temperature data from the SHEBA field study so the similarity in the pattern of pond coverage at the start of the season is evidence that the model is performing well. The Perovich *et al.* (2002) aerial observations and surface measurements are shown in figure 7.3. The maximum pond fraction observed by Perovich *et al.* (2002) was around day 174, early in the season, after this pond fraction decreased, this compares well with both the first-year ice and multi-year ice standard cases where there is a peak in pond coverage after snow cover is removed. El Naggar *et al.* (1998) observed a maximum pond fraction of approximately 31% on first-year ice and 19% on multi-year ice at the start of the season, the model results give local maxima of 38% and 47% in the first-year ice and multi-year ice cases respectively at this time. Whilst the multi-year ice value is high, the first-year ice value is closer, exceeding the observed value by only 7%. This observed maximum pond fraction was followed by a decrease in pond fraction before an increase again between day 200 and day 205, a pattern of pond coverage that was also seen in the first-year ice case, although not in the multi-year ice case. Eicken *et al.* (2002) also observed an increase in pond fraction towards mid July and another increase in mid August, the multi-year ice standard case shows the same increase a few days earlier on day 195. Perovich *et al.* (2002) observe ponds melting through to the ocean around day 182; this compares well with the model results, where at approximately this time the ocean fraction begins to increase in both the first-year ice and multi-year ice standard cases. The initial increase in ocean fraction in both the first-year ice and multi-year ice standard cases is close to the values observed in aerial photographs by Tschudi *et al.* (2001). On day 190, Tschudi *et al.* (2001) observed open ocean of approximately 5%, however the ocean

fraction increases far more rapidly in both the first-year ice and multi-year ice standard cases than in the observations made by Tschudi *et al.* (2001) towards the end of the season. This could be due to convergence of the ice pack in reality, which is not modelled in this thesis.

Whilst the general evolution of pond fraction compares well to observations there is much variability in observed pond fraction even in close locations, Yackel *et al.* (2000). There is most variability in pond fractions on first-year ice. In the first-year ice standard case the maximum fraction of the ice surface covered with ponds is 49% and mean pond fraction was 32% over the period when ponds were present. El Naggar *et al.* (1998) found the mean pond fraction on first-year ice to be between 20% and 48%, Fetterer & Untersteiner (1998) observe pond fraction of smooth ice to be between 30% and 50% and Eicken *et al.* (2004) observe pond fraction to vary between 10% and 60% on first-year ice. The pond fraction in the first-year ice standard case falls within these observations. Hanesiak *et al.* (2001) however observes a higher pond fraction of 75%, in the model only the thick snow sensitivity study and low permeability study have pond fractions this large. Comparing with the model results it is possible that the higher observed mean pond fractions on first-year ice could be due to lower ice permeability or a thick snow cover on that ice.

The maximum pond fraction in the multi-year ice standard case run is 47.1% with a mean pond fraction across the ice surface, calculated over the period when ponds were present, of 31.9% and a mean pond fraction of 24.8% when measured across the entire grid area. There is much variability in observations of pond fraction on multi-year ice, for example Hanesiak *et al.* (2001) observed low multi-year ice pond fractions of between 5% and 10% whereas Fetterer & Untersteiner (1998) and El Naggar *et al.* (1998) observed minimum and maximum pond fractions of double this, with pond fraction ranging from

12% to 26%. These values are all much lower than the mean and maximum pond fractions in the multi-year ice standard case, however, Eicken *et al.* (2004) observed a maximum pond fraction on level multi-year ice to be between 29% and 46% and the multi-year ice model results which were intended to model level multi-year ice compare well with these observations. A lower pond fraction of 9% to 21% was observed by Eicken *et al.* (2004) on rough multi-year ice, these values are much lower than the pond fractions on any of the multi-year ice simulations including rough multi-year ice simulations which suggests that the topography model does not adequately represent rough ice.

Fetterer & Untersteiner (1998) and Yackel *et al.* (2000) found that ponds on first-year ice had a larger surface area than ponds on multi-year ice and that there were more ponds on multi-year ice than on first-year ice because they are constrained by the ice surface topography often forming in depressions made by previously drained ponds. This observation was reproduced in the standard case runs, maximum mean pond area was 1.5 times greater on first-year ice than on multi-year ice. In both the first-year ice and multi-year ice standard cases ponds persist where they form initially, maximum mean pond size in the first-year ice case is 219 m^2 and maximum mean pond area in the multi-year ice case is 147 m^2. Tucker III *et al.* (1999) calculated a mean pond size of 63 m^2 on sea ice in the Eurasian Arctic, this is less than half the size of the maximum mean pond size in the multi-year case. However minimum pond size was 2 m^2 in the Tucker III *et al.* (1999) observations and maximum pond size was 8000 m^2, so there is clearly much variability and pond size is dependent on individual floe topography. Eicken *et al.* (2004) noticed mean pond area decreasing in the second half of the season, this is similar to both the first-year ice and multi-year ice standard cases.

Total ice ablation is 1.01 m in the first-year ice standard case and 1.41 m in the multi-year ice standard case. The SHEBA study measured total ice ablation to be 1.26 m

(Perovich *et al.* (2003)), which is a mean value for combined first-year ice and multi-year ice measurements although the ratio of first-year ice to multi-year ice is unknown. The observed ice ablation is between the first-year and multi-year total ice ablation and so seems to compare well to ice ablation in both modelled cases.

The mean albedo of the ice surface over the melt season in the first-year ice case is 0.64 and over the entire domain (which includes open ocean) is 0.56. In the multi-year ice case the mean albedo over the ice surface is 0.64 and over the entire domain is 0.53. Hanesiak *et al.* (2001) and Yackel *et al.* (2000) calculated the total surface albedo over first-year ice across photographed transects of an ice floe and found the average albedo to be 0.55, which is much less than the modelled fist-year ice albedo of 0.64. Eicken *et al.* (2004) compared mean pond fraction with total albedo and found that on a region of first-year ice where the mean pond fraction was 26% the mean albedo was 0.45, which can be compared with a mean area of the total grid covered with ponds in the first-year ice standard case of 25.4% and mean albedo of 0.56. In all comparisons with observations the modelled mean albedo is greater than the observed mean albedo which suggests that the model is underestimating albedo values. This could be improved by simulating variation of the optical properties, the properties about which there is most uncertainty, in the model.

7.5 Summary

The results of the standard simulations compare well with general trends of pond evolution observed in the field. The duration of pond coverage, pond area and ice ablation compare well in both first-year ice and multi-year ice cases. Whilst pond fraction in the modelled multi-year ice case appears higher than many of the multi-year ice observed values, it compares well with the level multi-year ice values of Eicken *et al.* (2002) which is the ice topography that we aimed to simulate. Observed mean albedo values are consistently

lower than modelled mean albedo values which suggests that calculation of albedo in individual cells in the model needs to be modified. However, the comparison with observations demonstrates that the melt-pond–sea-ice model described in this thesis is able to reasonably simulate melt pond evolution. Areas requiring model refinement will be discussed in the final chapter.

Chapter 8

Conclusions and Further Work

The sea-ice–melt-pond model presented in this thesis used a cellular automaton to model the physical processes that are thought to govern pond formation and evolution on a section of a sea ice floe. The processes modelled were horizontal and vertical water transport governed by Darcy's Law for flow through a porous medium and heat transport governed by the mushy-layer equations. Sea level with respect to the floe was calculated which allowed hydraulic head to be established. A permeability model related permeability to the sea-ice solid ice fraction. In addition, a stochastic topography model was used to generate topographies that represented ice and snow of various thicknesses and roughnesses.

The sensitivity of pond fraction, pond depth and total ablation to changes in permeability, and ice and snow topography was investigated. The sensitivity studies showed that pond fraction was very sensitive to reductions in vertical permeability in both first-year ice and multi-year ice cases. In the first-year ice case pond fraction was most sensitive to an increase in mean snow thickness, an equivalent sensitivity in multi-year ice was not observed.

When vertical permeability was reduced by one order of magnitude from the permeability in the standard first-year ice and multi-year ice cases deeper mean pond depth and

a larger area covered in ponds resulted. This is because ponds were unable to drain so rapidly so the ice surface was flooded with water, the extra surface water caused enhanced melting on a larger surface area of ice, which caused ponds to deepen. Doubling the mean snow thickness in the first-year ice case resulted in a 96% reduction in mass over the course of the melt season, This was surprising as there was a larger snow volume to be melted and therefore ice was exposed for a shorter period. However, the extra volume of melt water from the snow caused an increase in pond fraction, this caused more melting beneath ponds. When permeability was increased the effect on pond fraction was smaller since the ponds cannot drain below sea level and in the standard case the ponds were at sea level for most of the melt season.

There were definite differences between the first-year ice and multi-year ice standard cases, that were also observed by, for example, Fetterer & Untersteiner (1998) and Eicken *et al.* (2002). First-year ice had larger mean pond sizes and there were fewer ponds, mean pond depths were lower and, due to the smaller ice thickness, more ice cells melted through in the first-year ice case although the total ablation was less. In the multi-year ice case ponds were smaller and deeper but there were more of them. These trends appear as a result of the differences in topography. Since despite these differences the maximum pond coverage and the mean pond coverage were approximately the same in both cases. A possible reason for this is that ponds form only in the regions below sea level and there are similar surface areas below sea level in both cases. However, the cells with negative ice surface height have greater negative surface height with respect to sea level in the multi-year ice case than in the first-year ice case, the ponds tend to be deeper on multi-year ice.

It was found that a significant improvement in the model described in this thesis over that of Lüthje *et al.* (2006) was the calculation of sea level. The model described in

this thesis clearly demonstrates how quickly ponds drain to sea level and the impact this has on pond coverage. This is particularly evident on first-year ice where pond fraction is greatly reduced when the snow cover is thin. This is because the melt water drains rapidly vertically through the ice and the only ponded cells are those with pond surface height at or below sea level. The rapid drainage rate appears to be the cause for the reduction in pond fraction when snow cover was thin. This result offers an explanation for the lack of ponds observed when snow cover was manually removed from first-year ice, Eicken *et al.* (2002).

Altering the surface roughness had two interesting results, firstly topographies with the same standard deviation, range and initial mean thickness produced almost identical evolution of pond fractions and mean pond depths when run under the same initial conditions. Secondly the impact of increasing surface roughness was limited. Whilst there was a difference in pond fraction when varying the ice roughness from smooth first-year ice to rough first-year ice there was very little difference in pond fraction when the surface roughness was increased from standard multi-year ice to rough multi-year ice. This appears to be because once the roughness of the surface is great enough for cells to have negative surface height any further increase in roughness will only cause the difference in height between cells to increase and the proportion of cells with surfaces below sea level will remain approximately the same. The regions where ponds can form is also therefore unchanged.

Snow topography in general only had an impact at the start of the season in determining the surface area covered in ponds from snow melt. With the exception of the thick snow case in the first-year ice sensitivity studies, different initial snow topographies had little impact later in the season. There were two studies where snow cover had a large impact on pond coverage: on first-year ice, thinner snow cover caused a reduction in pond

fraction; and a thicker snow cover on first-year ice caused an increase in pond coverage and surface ablation, this was because the gradients between cells was small and surface water could flood the whole surface. Altering the roughness of snow cover caused very little change in pond fraction.

Simulation of the formation and evolution of melt ponds on first-year ice and level multi-year sea ice compared well with observations (Chapter 7). Whilst this model enhances our understanding of the physics that underlies pond formation and evolution and confirmed the importance, in particular, of ice topography in governing the fraction of the surface covered in ponds, there are areas where this model could be improved.

The two aspects of the sea-ice model where improvements are most warranted are the aspects of the model about which there is most uncertainty. These are the vertical permeability of the ice and the optical properties of sea ice. Model results could also be enhanced by modelling the ice surface topography more realistically.

The vertical permeability varies with the solid fraction at the base of the ice, in this model the solid fraction at the base of ice is fixed because the temperature of the ocean is constant, so the vertical permeability is constant with time. However, since permeability was shown to have a large effect on the surface area covered with ponds, and is known to change by several orders of magnitude during the melt season, this needs to be modelled. In conjunction with this, the model for vertical and horizontal drainage could be enhanced. Currently this model makes no attempt to model the changes in relative importance of the vertical or horizontal drainage throughout the season. Eicken *et al.* (2004) observe horizontal drainage dominates in the first half of the season but vertical drainage dominates in the rest of the season. Improving the vertical permeability calculation would cause a greater surface area of ponds early in the melt season when permeability is low. Later in the season vertical permeability would increase which would probably cause a decrease in

pond fraction and pond depth.

There are differences in the optical properties of first-year ice and multi-year ice. Multi-year ice contains more air bubbles than first-year ice, in general the surface layer of multi-year ice is drained and bubbly before the onset of melting, Perovich (1996). First-year ice has more brine pockets at the surface and these are less scattering than air bubbles. The increased scattering in multi-year ice allows less radiation to be absorbed into the ice, therefore there is less surface melting on multi-year ice. Improving the optical parameters would probably have the result of reducing the pond fraction on multi-year ice by causing less melting and increasing pond fraction on first-year ice by causing more melting.

Finally it was assumed in this model that the ice surface topography was isotropic, this meant that features with long length scales could not be modelled, this includes features such as ridges, which would affect the freeboard of the ice floe and therefore the pond fraction. There is also currently no correlation between snow thickness and ice surface topography, an improvement would be model thick snow in the surface depressions in the ice, or beside ridges to simulate wind blown snow. The changes to topography would give a more realistic idea of pond fraction, pond depth an pond shape and further highlight the differences between first-year ice and multi-year ice.

The automaton design has some limitations, in that a three-dimensional space is represented but equations are solved separately in the vertical and horizontal directions. Lateral melting is observed at the edges of floes, cracks and pond edges and this is not represented at all by the model in this thesis. It would be possible to solve three-dimensional heat flux equations, however the computation time for this is large even at low resoution.

Despite the limitations of the model described in this thesis it has improved our understanding of the physics that governs the formation and evolution of melt ponds on Arctic sea ice.

Bibliography

Bamber, J. L. & Payne, A. J. 2004 *Mass Balance of the Cryosphere*. Cambridge University Press.

Batchelor, G. K. & Moffatt, H. K. 2000 *Convection in the Environment*, chap. 6, p. 289. Cambridge University Press.

Bear, J. 1988 *Dynamics of Fluids in Porous Media*. Dover.

Chiles, J.-P. & Delfiner, P. 1999 *Geostatistics: Modeling Spatial Uncertainty*. Wiley.

Cox & Weeks 1974 Salinity variations in sea ice. *Journal of Glaciology* **13(67)**, 109–120.

Curry, J. A. & Ebert, E. E. 1992 Annual cycle of radiative fluxes over the Arctic Ocean: Sensitivity to cloud optical properties. *Journal of Climate* **5**, 1267–1280.

Curry, J. A. & Webster, P. J. 1999 *Thermodynamics of Oceans and Atmospheres*. Academic Press.

Ebert, E. E. & Curry, J. A. 1993 An intermediate one-dimensional thermodynamic sea ice model for investigating ice-atmosphere interactions. *Journal of Geophysical Research* **98**, 10085–10109.

Ebert, E. E., Schramm, J. L. & Curry, J. A. 1995 Disposition of solar radiation in sea ice and the upper ocean. *Journal of Geophysical Research* **100**, 15965–15975.

Eicken, H., Grenfell, T. C., Perovich, D. K., Richter-Menge, J. A. & Frey, K. 2004 Hydraulic controls of summer Arctic pack ice albedo. *Journal of Geophysical Research* **109**, C08007, doi: 10.1029/2003JC001989.

Eicken, H., Krouse, H. R., Kadko, D. & Perovich, D. K. 2002 Tracer studies of pathways and rates of meltwater transport through Arctic summer sea ice. *Journal of Geophysical Research* **107**, C10, 8046, doi: 10.1029/2000JC000583.

El Naggar, S., Garrity, C. & Rameseier, R. O. 1998 The modelling of sea ice melt-water ponds for the high Arctic using an airborne line scan camera, and applied to the satellite special sensor microwave/imager (ssm/i). *Journal of Remote Sensing* **19**, 2373–2394.

Feltham, D. L., Untersteiner, N., Wettlaufer, J. S. & Worster, M. G. 2006 Sea ice is a mushy layer. *Geophysical Research Letters* **33**, L14501, doi:10.1029/2006GL026290.

Fetterer, F. & Untersteiner, N. 1998 Observations of melt ponds on Arctic sea ice. *Journal of Geophysical Research* **103**, C11,24821–24835.

Flocco, D. & Feltham, D. L. 2007 A continuum model of melt pond evolution on Arctic sea ice. *Journal of Geophysical Research* **112**, C08016, doi: 10.1029/2006JC003836.

Freitag, J. & Eicken, H. 2003 Meltwater circulation and permeability of Arctic summer sea ice derived from hydrological field experiments. *Journal of Glaciology* **49**, 349–358.

Golden, K. M., Eicken, H., Heaton, A. L., Miner, J., Pringle, D. J. & Zhu, J. 2007 Thermal evolution of permeability and microstructure in sea ice. *Geophysical Research Letters* **34**, L16501, doi: 10.1029/007GL030447.

Hanesiak, J. M., Barber, D. G., De Abreu, R. A. & J., Y. J. 2001 Local and regional albedo observations of Arctic first-year sea ice during melt ponding. *Journal of Geophysical Research* **106**, C1,1005–1016.

Holt, B. & Digby, S. A. 1985 Processes and imagery of first-year fast sea ice during the melt season. *Journal of Geophysical Research* **90**, 5045–5062.

Houghton, J. T., Ding, Y., Griggs, D. J., Noguer, M., van der Linden, P. J., Dai, X., Maskell, K. & Johnson, C. A. 2001 *Climate Change 2001: The Scientific Basis: Contribution of Working Group I to the Third Assessment Report of the Intergovernmental Panel on Climate Change*. Cambridge University Press.

Isaaks, E. H. & Srivastava, R. M. 1989 *Applied Geostatistics*. Oxford University Press.

Laxon, S., Peacock, N. & Smith, D. 2003 High interannual variability of sea ice thickness in the Arctic region. *Nature* **425**, 947–950.

Lemke, P., Ren, J., Alley, R. B., Carrasco, J., Flato, G., Fujoo, Y., Kaser, G., Mote, P., Thomas, R. H. & Zhang, T. 2007 *Climate Change 2007: The Physical Science Basis. Contribtion of Working Group I to the Fourth Assessment Report of the Intergovernmental Panel on Climate Change*, chap. Observations: Changes in Snow, Ice and Frozen Ground. Cambridge University Press.

Lindsay, R. W. 1998 Temporal variability of the energy balance of thick Arctic pack ice. *Journal of Climate* **11**, 313–331.

Lüthje, M., Feltham, D. L., Taylor, P. D. & Worster, M. G. 2006 Modeling the summertime evolution of sea-ice melt ponds. *Journal of Geophysical Research* **111**, C02001, doi:10.1029/2004JC002818.

Maslanik, J. A., Fowler, C., Stroeve, J., Drobot, S., Zwally, J., Yi.D. & Emery.W. 2007 A younger, thinner Arctic ice cover: Increased potential for rapid extensive sea-ice loss. *Geophysical Research Letters* **34**, L24501, doi: 10.1029/2007GL032043.

Maykut, G. A. & Untersteiner, N. 1971 Some results from a time-dependent thermodynamic model of sea ice. *Journal of Geophysical Research* **76**, 1550–1575.

McGuffie, K. & Henderson-Seller, A. 2005 *A Climate Modelling Primer*. John Wiley and Sons.

Mellor, L. & Kantha, L. 1989 An ice-ocean coupled model. *Journal of Geophysical Research* **94**, 10937–10954.

Nazintsev, Y. L. 1964 Thermal balance of the surface of the perennial ice cover in the central Arctic *in Russian. Tr. Ark. Antark. Nauchno Issled. Inst.* **267**, 110–126.

Notz, D. 2005 *Thermodynamic and Fluid-Dynamical Processes in Sea Ice*. Ph.D Thesis, University of Cambridge.

Perovich, D. K. 1990 Theoretical estimates of light reflection and transmission by spatially complex and temporally varying sea ice covers. *Journal of Geophysical Research* **95**, C6,9557–9567.

Perovich, D. k. 1996 *The Optical Properties of Sea Ice*. Monograph.

Perovich, D. K., Grenfell, T. C., Light, B., Richter-Menge, J. A., Sturm, M. and Tucker III, W. B., Eicken, H. & Maykut, G. A. and Elder, B. 1999 SHEBA: Snow and ice studies CD-ROM, version 1.0. CD-ROM.

Perovich, D. K., Grenfell, T. C., Richter-Menge, J. A., Light, B., B., T. I. W. & Eicken.H. 2003 Thin and thinner: Sea ice mass balance measurements during SHEBA. *Journal of Geophysical Research* **108**, C3(8050).

Perovich, D. K., Tucker III, W. B. & Ligett, K. A. 2002 Aerial observations of the evolution of ice surface conditions during summer. *Journal of Geophysical Research* **107**, C10,8048.

Rodo, X. & Comin, F. A. 2003 *Global Climate*. Springer.

Semtner, A. J., J. 1976 A model for the thermodynamic growth of sea ice in numerical investigations of climate. *Journal of Physical Oceanography* **6**, 379–389.

Shine, U. & Henderson-Sellers, P. 1985 The sensitivity of a thermodynamic sea ice model to changes in surface albedo parameterization. *Journal of Geophysical Research* **90(D1)**, 2243–2250.

Slaymaker & Kelly 2007 *The Cryosphere and Global Environmental Change*. Wiley-Blackwell.

Stroeve, J., Holland, M. M., Meier, W., Scambos, T. & Serreze, M. 2007 Arctic sea ice decline: Faster than forecast. *Geophysical Research Letters* **34**, L09501.

Stroeve, J., Markus, T., Meier, W. N. & Miller, J. 2006 Recent changes in the Arctic season. *Annals of Glaciology* **44**, 367–374.

Sturm, M., Holmgren, J. & Perovich, D. K. 2002 Winter snow cover on the sea ice of the Arctic Ocean at the Surface Heat Budget of the Arctic Ocean (SHEBA): Temporal evolution and spatital variability. *Journal of Geophysical Research* **107**, C10,8047.

Taylor, P. D. 2003 *Mathematical Modelling the Formation and Evolution of Melt Ponds on Sea Ice*. Ph.D Thesis, University of London.

Taylor, P. D. & Feltham, D. L. 2004 A model of melt pond evolution on sea ice. *Journal of Geophysical Research* **109**, C12007, doi:10.1029/2004JC002361.

Thomas, D. N. & Dieckmann, G. S. 2003 *Sea Ice*. Blackwell Publishing.

Thorndike, A. S., Rothrock, D. A., Maykut, G. A. & Colony, R. 1975 The thickness distribution of sea ice. *Journal of Geophysical Research* **80**, 4501–4513.

Tschudi, M. A., Curry, J. A. & Malanik, J. A. 2001 Airborne observations of summertime surface features and their effect on surface albedo during FIRE/SHEBA. *Journal of Geophysical Research* **106**, D14,15335–15344.

Tucker III, W. B., Gow, A. J., Meese, D. A., Bosworth, H. W. & Reimnitz, E. 1999 Physical characteristics of summer sea ice across the Arctic Ocean. *Journal of Geophysical Research* **104**, 1489–1504.

Untersteiner, N. 1968 Natural desalination and equilibrium salinity profile of perennial sea ice. *Journal of Geophysical Research* **73(4)**, 1251–1257.

Wadhams, P. 2000 *Ice in the Ocean*. CRC Press.

Weeks, W. F. & Ackley, S. F. 1986 *The Geophysics of Sea Ice*, chap. The Growth, Structure and Properties of Sea Ice, pp. 1–165. Plenumn.

Wettlaufer, J. S., Worster, M. G. & Huppert, H. E. 1997 The phase evolution of young sea ice. *Geophysical Research Letters* **24**, 1251–1254.

Whelan, J. and Maslowski, W., Clement Kinney, J. L. & Jakacki, J. 2007 Understanding recent variability in the Arctic sea ice thickness and volume -synthesis of model results and observations. EOS Transactions of the American Geophysical Union (52): Fall Meeting Supplement, Abstract C22A-06.

Yackel, J. J., Barber, D. G. & Hanesiak, J. M. 2000 Melt ponds on sea ice in the Canadian Archipelago 1. Variability in morphological and radiative properties. *Journal of Geophysical Research* **105**, C9, 22049–22060.